DYNAMIC MODELING AND CONTROL OF A HYBRID FIN ACTUATION SYSTEM FOR AN AIR-TO-AIR MISSILE

A THESIS SUBMITTED TO
THE GRADUATE SCHOOL OF NATURAL AND APPLIED SCIENCES
OF
MIDDLE EAST TECHNICAL UNIVERSITY

BY

TAYFUN ÇELİK

IN PARTIAL FULFILLMENT OF THE REQUIREMENTS
FOR
THE DEGREE OF MASTER OF SCIENCE
IN
MECHANICAL ENGINEERING

DECEMBER 2014

Approval of the thesis:

DYNAMIC MODELING AND CONTROL OF A HYBRID FIN ACTUATION SYSTEM FOR AN AIR-TO-AIR MISSILE

submitted by **TAYFUN ÇELİK** in partial fulfillment of the requirements for the degree of **Master of Science in Mechanical Engineering Department, Middle East Technical University** by,

Prof. Dr. Gülbin Dural Ünver _____
Dean, Graduate School of **Natural and Applied Sciences**

Prof. Dr. R. Tuna Balkan _____
Head of Department, **Mechanical Engineering**

Assoc. Prof. Dr. Ender Ciğeroğlu _____
Supervisor, **Mechanical Engineering Dept., METU**

Assist. Prof. Dr. Yiğit Yazıcıoğlu _____
Co-Supervisor, **Mechanical Engineering Dept., METU**

Examining Committee Members:

Prof. Dr. Reşit Soylu _____
Mechanical Engineering Dept., METU

Assoc. Prof. Dr. Ender Ciğeroğlu _____
Mechanical Engineering Dept., METU

Assist. Prof. Dr. Kıvanç Azgın _____
Mechanical Engineering Dept., METU

Assist. Prof. Dr. Yiğit Yazıcıoğlu _____
Mechanical Engineering Dept., METU

Dr. Bülent Özkan _____
Mechatronics Division, TÜBİTAK SAGE

Date : _____

I hereby declare that all information in this document has been obtained and presented in accordance with academic rules and ethical conduct. I also declare that, as required by these rules and conduct, I have fully cited and referenced all material and results that are not original to this work.

Name, Last name : Tayfun ÇELİK

Signature :

ABSTRACT

DYNAMIC MODELING AND CONTROL OF A HYBRID FIN ACTUATION SYSTEM FOR AN AIR-TO-AIR MISSILE

Çelik, Tayfun

M.S., Department of Mechanical Engineering

Supervisor : Assoc. Prof. Dr. Ender Ciğeroğlu

Co-Supervisor : Assist. Prof. Dr. Yiğit Yazıcıoğlu

December 2014, 136 pages

Air-to-air missiles require high maneuverability. In order to obtain high maneuverability, hybrid fin actuation systems are used. In this study, a hybrid fin actuation system which is composed of aerodynamic control surfaces and thrust vector control is designed. Both aerodynamic and thrust vector control types are explained and the most suitable pair is determined for air-to-air missile. Then, the designed system is physically constructed and system identification procedure is performed. After that three different controllers PID, H_∞ and 2-DOF H_∞ controllers are designed and tested on both on the real system and simulation environment. Finally, all the results are compared with the cascaded H_∞ controller.

Keywords: Fin actuation systems, jet vane, H_∞ robust control, system identification, cascaded systems

ÖZ

HAVADAN HAVAYA FÜZELER İÇİN MELEZ KANATÇIK TAHRİK TASARIMI VE MODELLENMESİ

Çelik, Tayfun

Yüksek Lisans, Makina Mühendisliği Bölümü

Tez Yöneticisi : Doç. Dr. Ender Ciğeroğlu

Ortak Tez Yöneticisi : Yrd. Doç. Dr. Yiğit Yazıcıoğlu

Aralık 2014, 136 sayfa

Havadan-havaya füzeler yüksek manevra kabiliyeti gerektirmektedir. Bu yüksek manevra kabiliyetini yakalamak için melez kanatçık tahrik sistemleri kullanılmaktadır. Bu çalışmada aerodinamik yüzeylerin kontrolü ve itki vektör kontrolü sistemi içeren melez bir kanatçık tahrik sistemi tasarlanmıştır. Hem aerodinamik hem de itki vektör kontrol yöntemleri hakkında bilgi verilmiştir. Bu sistemlerden hava-hava füzesi için en uygun ikiliye karar verilerek sistemin üretimi gerçekleştirilmiştir. Bu sistem için PID, H_∞ ve ikinci derece H_∞ kontrolcüler tasarlanmıştır. Bu kontrolcüler hem benzetim ortamında hem de sistem üzerinde denemiştir. Son olarak sistem için çift döngülü, her iki döngüsünde de H_∞ kontrolcü olan kontrolcüyle test edilmiş ve elde edilen sonuçlar diğer kontrolcülerle elde edilen sonuçlarla karşılaştırılmıştır.

Anahtar kelimeler: Kanatçık tahrik sistemleri, jet vanası, H_∞ gürbüz kontrol, sistem tanımlama, çift döngülü sistem

To My Parents

and

My Love Pınar Çelik

ACKNOWLEDGEMENTS

I would like to send my thanks to my supervisor Assoc. Prof. Dr. Ender CİĞEROĞLU. During preparation of my thesis, my supervisor gave me very special support by his helpful criticism, guidance and patience. I would also like to thank to my co-supervisor Assist. Prof. Dr. Yiğit YAZICIOĞLU due to his contribution.

I want to express my appreciation to my head of division Dr. Bülent ÖZKAN. His encouragements and technical support during progress of the thesis are very valuable. I also specially want to thank to my colleague Berkay BAYKARA for his endless help and patience. My colleague Göktuğ Gencehan ARTAN's encouragements and motivation for this work are delicately appreciated.

I am very grateful to support of TÜBİTAK BİDEB and facilities of TÜBİTAK SAGE in the application of experimental studies of my thesis.

I want to send my thanks to all members of family. They give me endless support and patience throughout my life.

Finally, I am very thankful to my wife Pınar ÇELİK. During progress and preparation of my thesis, my love gave me all motivation and energy for finishing this work.

TABLE OF CONTENTS

LIST OF TABLES

TABLES

LIST OF FIGURES

FIGURES

CHAPTER 1

INTRODUCTION

1.1 Aim of the Study

Air-to-air missiles are very agile munitions that are designed to hit aerial targets. Most of them are equipped with both thrust vector control (TVC) and aerodynamic control surfaces.

In this study, the practicability of the TVC and aerodynamic control surfaces are examined and the most proper pair is chosen and constructed. The challenges of this system is that, it should be compact and modular. The designed system is both affected by aerodynamic forces and exhaust gas of rocket motor so that during the flight of the missile, fin actuation system must be stable and give satisfactory performance required by the physical system and concept of operation. In this thesis, electromechanical system is designed that contains a motor, an encoder, a gear pair and a four link mechanism. The system has some nonlinearities due to its physical nature such as gear backlash. In the light of these facts, the system is simulated and tested by robust controllers.

In this thesis, cascaded H_∞ norm-based control approach is applied to the fin actuation system and this controller is compared in terms of stability and performance to H_∞, 2-DOF H_∞ and PID controllers.

1.2 Scope of the Thesis

In Chapter 1, the general information about the aerodynamic control and TVC control systems are given such that the idea behind the system is well defined. Then,

the theory of the robust control is presented in summary. At the end of this chapter, similar works that are done for control/fin actuation system are given.

In Chapter 2, the physical system is interpreted in detail. The subcomponents of the system are interpreted and their mathematical models are derived in this part. Then the total system is identified and made ready to implement the controller which is synthesized according to the identified plant model.

In Chapter 3, PID, 1-DOF H_∞, 2-DOF H_∞ and cascaded H_∞ of controllers are designed and exhibited. All of them are simulated and tested with physical system. All the data obtained are presented in this section.

In Chapter 4, computer simulations and test results of the controllers are compared and represented in this section.

And finally in Chapter 5, the results are discussed and summarized. The related future works are also proposed in this chapter.

1.3 Background and Basic Concepts

1.3.1 A General Information about Air-to-Air Missile (AAM)

An air-to-air missile is launched from an aerial platform to destroy an opposing one. In general manner, AAMs are used to protect air space, air vehicles and other aerial platforms from hostile air forces. AAMs are broadly divided in two groups which are short range "within visual range" and medium or long range "beyond visual range" missiles. Short range missiles are launched to destroy the enemy aircraft when the hostile platform is close enough and there is no chance to fire medium or long range missile. Short range AAMs are much more agile than long range missiles because of the limited range to maneuver; therefore, some of them have thrust vector control unit to develop agility. On the contrary, medium range missiles are optimized to enhance performance and weight while long range missiles are designed to increase speed and range. They are also equipped with a radar seeker unit. Both of them have some advantages over another but the current developments show that shooting down an enemy from a distance is a new trend. For this reason, MBDA, a multi-national missile corporation was formed by Matra Missile, BAE Dynamics and Alenia Marconi Systems that currently develops Meteor ramjet engine for a long range

missile and several nations try to develop their long range missiles [1].

1.3.2 Control Actuation System (CAS)

Control actuation system (CAS) is an important part of a missile which steers the missile according to the commands coming from guidance system which means that CAS converts an electrical input command to an appropriate output shaft angle as seen in Figure 1 [2]. CAS is composed of electronic cards 'driver etc.', power sources 'thermal battery' and fin actuation system (FAS). Typically, there are three major types of control systems which are aerodynamic control, thrust vector control and reaction control. In a missile, they can be used individually or together. Especially for AAM, maneuverability is severe when it is compared to other missiles such as cruise, ballistic etc. Therefore, in order to follow desired path both of these techniques can be applied. In the sense of AAM, the main idea of using together is to enhance the desired maneuverability.

Missile configuration design decides the FAS space, weight limitations, types of control elements and power requirements while the missile stabilization and guidance loop determines the FAS requirements. According to FAS mechanical design, FASs are classified as electro-hydraulic, electromechanical or electro-pneumatic. Hydraulic type actuators are used where large forces are required. For example, Tomahawk cruise missile uses hydraulic actuators while AIM 9L/M/N have pneumatic actuators because forces acting on aerodynamic surfaces are imperatively small enough to control using pneumatic actuators [3]. The difference comes from , power requirement, package of system, cost, reliability, repeatability, manufacturability, and controllability. But today's AAMs are usually equipped with electromechanical FAS [4].

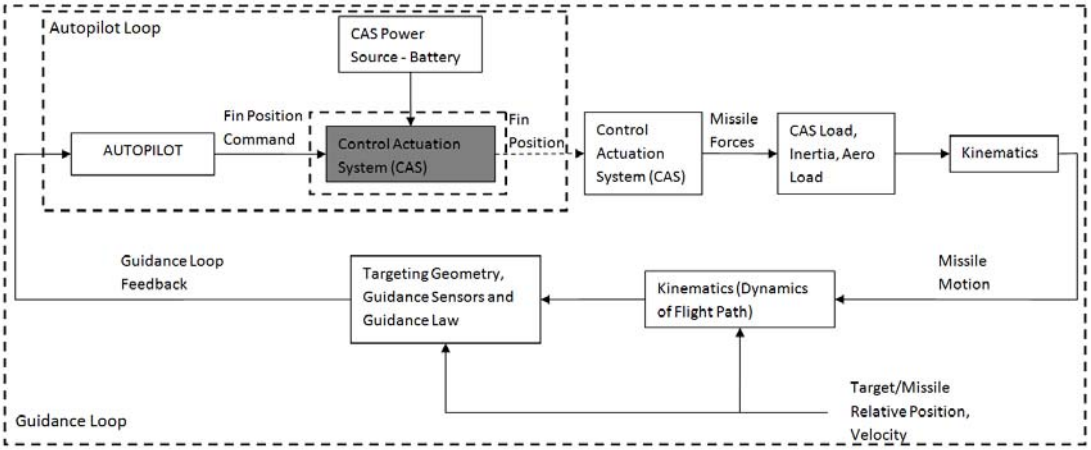

Figure 1. *Auto pilot of the missile [5]*

1.4 Types of Control Systems

1.4.1 Aerodynamic Control

In order to understand the flight of missile, first of all, the motion that missile makes should be understood correctly. The rotation of missile fins about a pivot point changes the direction and magnitude of the aerodynamics forces on the fins, which cause missile to move in intended direction. In Figure 2, it can be seen that, during a flight, missile makes three different types of motion. During pitch motion, missile raise or lower its nose, while in yaw motion, it turns the sideways, and finally in roll motion, missile spins about the main axis of itself [3].

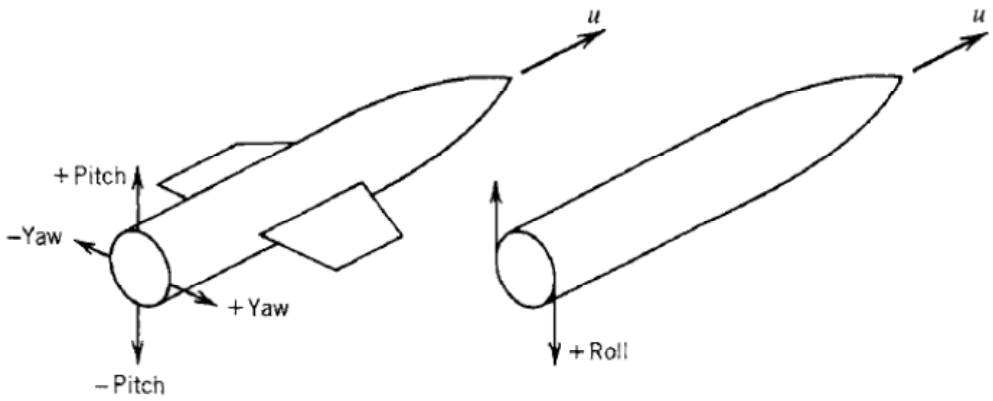

Figure 2. *Missile motions [3]*

The aerodynamic surfaces are inevitable parts of the missiles thus missile designers arrange the location and the geometry of fins so that the minimum hinge moment and maximum maneuverability can be obtained [1]. As it can be seen in Figure 3, many types of aerodynamic configuration are used for missiles. Both of these techniques have some advantages and disadvantages over each other. The most popular air vane control techniques that are used in AAMs are canard, wing and tail type controls.

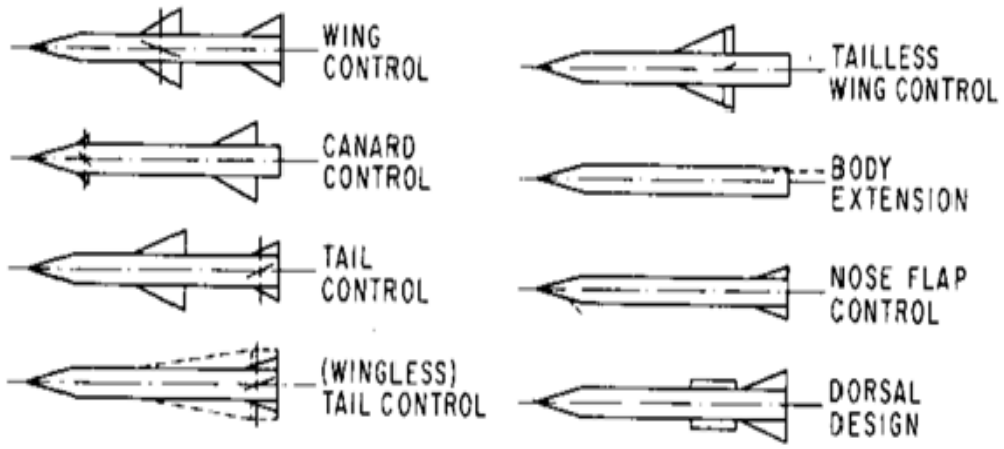

Figure 3. *Air Vane Control Techniques [6]*

1.4.1.1 Wing Control

The first examples of AAMs are generally designed with movable wings because this technique leads to extremely fast response characteristics to body lateral accelerations. In this configuration, control surfaces are arranged close to the center of gravity of the missile and this arrangement causes high hinge moment, severe power requirement, large rolling moment, and nonlinear aerodynamic behavior [6]. In addition to these, wings are relatively large to obtain desired lift and control forces. Although this technique results in lots of disadvantages, fast control and good packaging capabilities are some of featured properties of wing control.

1.4.1.2 Canard Control

In this configuration, control surfaces are attached to the well forward on the missile body. In order to obtain desired lift, the relatively large surfaces compared to canards are attached to wing or tail of the body. The most attractive features of this

configuration are simplicity of packaging, lower missile weight and drag, reduced power requirement, and lower torque requirements [5]. In addition to these, it easily compensate the change of center of gravity due to design changes by making simple relocation of canards. Some of the major disadvantages of this configuration are difficulty of roll stabilization and high surface rates in order to obtain the desired rate of response [6]. The most important example of canard control AAMs is Rafael's Python series.

1.4.1.3 Tail Control

Tail control has slow response characteristic since the tail deflection is in the opposite direction of the angle of attack so that tail angle of attack and hinge moment are generally low. Aerodynamic characteristics of this configuration are linear because wing-tail interference effects are reduced; therefore induced rolling moments are low [7]. The notable disadvantage is limited space available for the CAS due to rocket motor and nozzle. In recent years, nearly all AAMs are designed with tail control.

1.4.2 Control Surface Arrangement

Control surface arrangement is another important point of aerodynamic design. Speed, range and acceleration during motion affect the configurations. Most popular arrangements are shown in Figure 4 but AAMs are generally configured with cruciform arrangements.

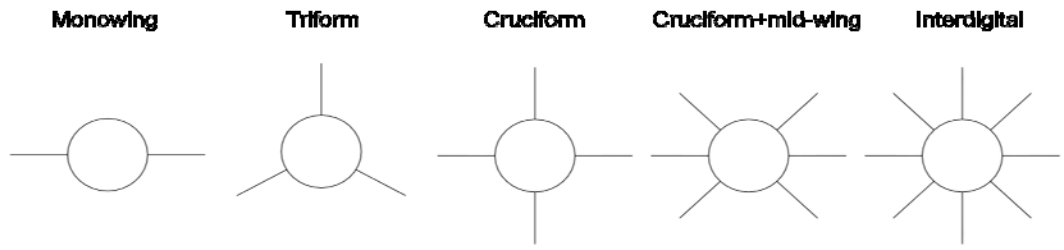

Figure 4. *Arrangements of missile fins*

1.4.2.1 Monowing

Monowing arrangement is the lightest solution because it contains only two fins. In this configuration, the missile body is exposed to lower drag than others but wing areas are wider. This system is widely used in cruise missiles. Turning strategy of monowing missiles is only bank-to-turn.

1.4.2.2 Triform

In triform arrangement, fins area is nearly equal to the cruciform arrangements. This arrangement achieves demanded lift and maneuver using three fins. This system becomes cheaper than cruciform arrangements since the part and actuator numbers are decreased.

1.4.2.3 Cruciform

Most of the missiles are equipped with cruciform arrangements. This arrangement can be in x roll orientation or + roll orientation as shown in Figure 5. X roll orientation has some advantages over + roll orientation. X roll has better launch platform compatibility, higher stability and control effectiveness. Especially for supersonic missiles, these types of configuration are better for use [7]. Patriot, AIM 120, AIM-9X, and IRIS-T are some of the examples.

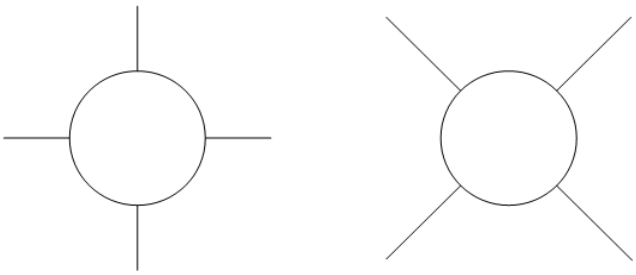

Figure 5*."+" and "x" cruciform arrangement*

1.4.3 Thrust Vector Control (TVC)

Several munitions and ejection systems need steering system in order to follow demanded route and to catch target. Since 1960, designers have searched new missile steering systems because classical aerodynamic control surfaces are not sensitive to follow the route and also maneuverability is insufficient. Especially for

exoatmospheric flight, aerodynamic surfaces become meaningless so these studies accelerated. Thrust Vector Control (TVC) is the most imported method that was developed during these studies. In all of the TVC systems; materials, mechanism design, manufacturing and also aerodynamics design are seen critical technologies. As it can be understood from Figure 6, the working principle of TVC is diverting the direction of the main thrust vector about vehicle axis; therefore, creating a moment about a center of mass of the missile body which cause missile to turn.

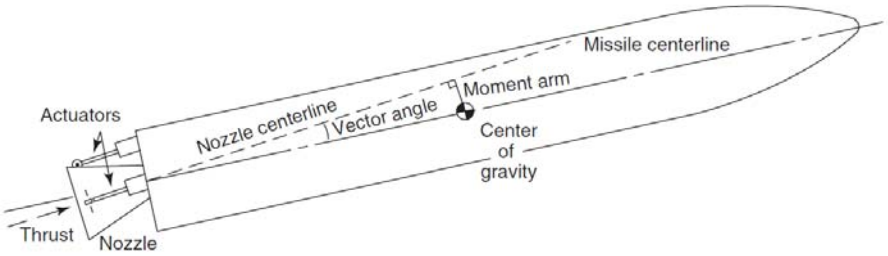

Figure 6. *Working principles of TVC [8]*

TVC systems can be grouped in many ways. According to nozzle type, TVC systems are classified as given in Figure 7.

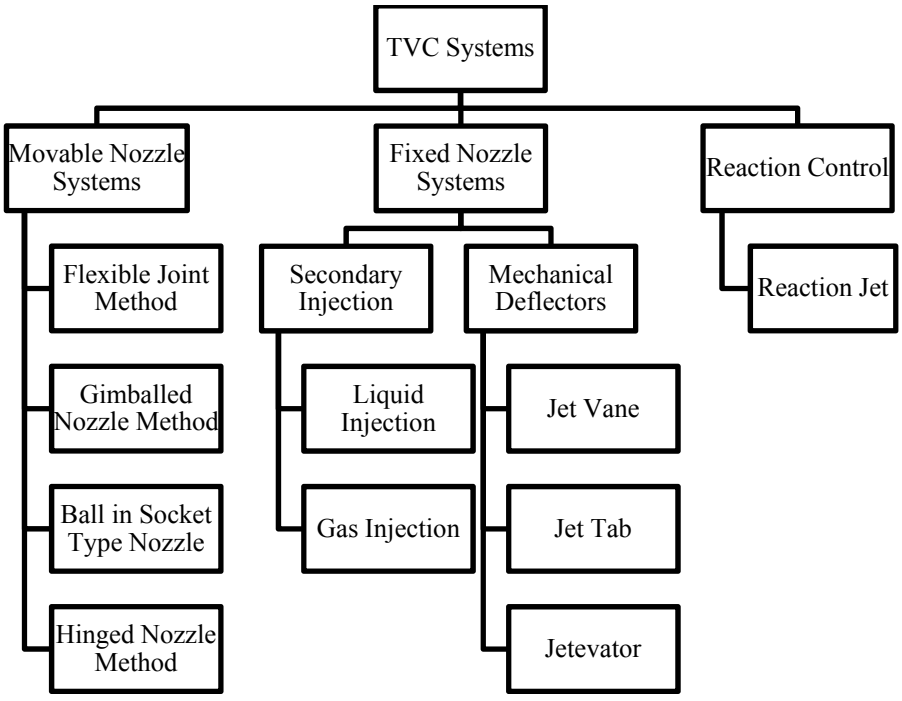

Figure 7*. Thrust vector control systems*

TVC systems are used quite a lot in air defense systems, satellite launch rockets, AAMs, and also intercontinental ballistic missiles. TVC systems have many advantages for different types of applications, especially for

- High speed rockets that require high maneuverability
- Manual controlled anti-tank munitions where the aerodynamic control is hard and speed is low
- Vertical launched systems that makes sudden maneuver
- Rockets fired from submarines
- Air defense system
- Platforms like space vehicles where aerodynamic control is impossible and dynamic pressure is very low.

1.4.3.1 Movable Nozzle Systems (MNS)

Movable nozzle systems are efficient systems that contain a rocket motor, movable nozzle and the joining technique that determines the method itself. Although these systems have some problems due to manufacturing difficulties and functional errors, their performance are quite high. All of the movable nozzle systems are restricted with multi nozzle system because it is not possible to control roll axis effectively when they are used alone. In order to control roll axis, minimum two movable nozzles should be integrated to the system as in Figure 8.

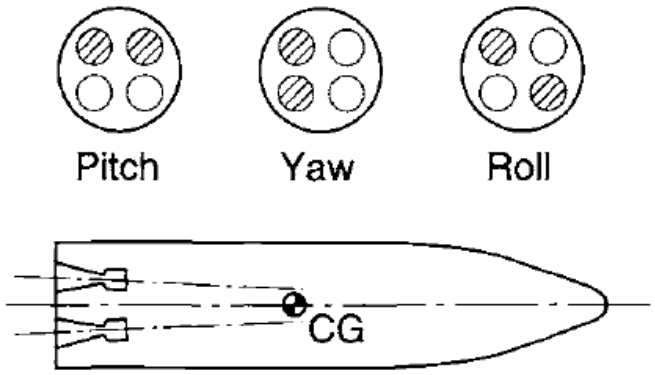

Figure 8. *Flight maneuvers of four-fixed position thrust chambers [3]*

In, NASA-SP-8114 [9], TVC systems up to 1974 is examined, and detailed information about all TVC systems is given. According to [9], nearly more than half of the TVC system designed was only tested in laboratory environment; therefore, in this thesis, only tested and applied methods are mentioned briefly. When movable nozzle systems are investigated, it is understood that these systems are generally used in satellite launch rocket, large diameter ballistic missiles and air defense systems. Difference from the other systems, air defense systems are supported with buster which is ejected after missile reaches desired altitude. Movable nozzle TVC systems are divided into four groups according to the mechanisms.

1.4.3.1.1 Flexible Joint Method

In this method, rocket motor and nozzle are attached to each other by using a flexible joint which is composed of an elastomeric material and a metal or a composite material [10]. The development and manufacturing of flexible joint, insulation material and design of sealing are critical technologies of this system. Power requirements are also high. Despite of these difficulties, flexible joint method is one of the most used methods especially in ballistic missiles and space vehicles. Figure 9 shows the schematic view of flexible joint method TVC system.

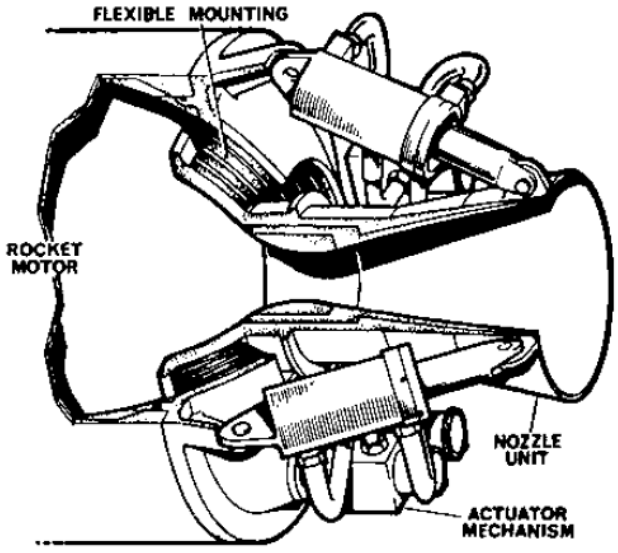

Figure 9. *Schematic of flexible nozzle [11]*

1.4.3.1.2 Gimbaled Nozzle Method

The nozzle is fastened to the rocket motor via gimbal mechanisms. In this method, thrust loss is quite small but the sliding motion of the gimbal which makes it difficult to maintain sealing. Reliability of these systems depends on whether or not the sealing is designed well. Because of these, this method is not preferred in tactical missile systems.

1.4.3.1.3 Ball in Socket Type Nozzle

The nozzle is attached to the motor by means of a spherical joint [10]. In the Figure 10 given below illustrates the ball in socket type nozzle TVC system. This method's development was interrupted by the development flexible joint method because these systems are only tested in laboratory environment.

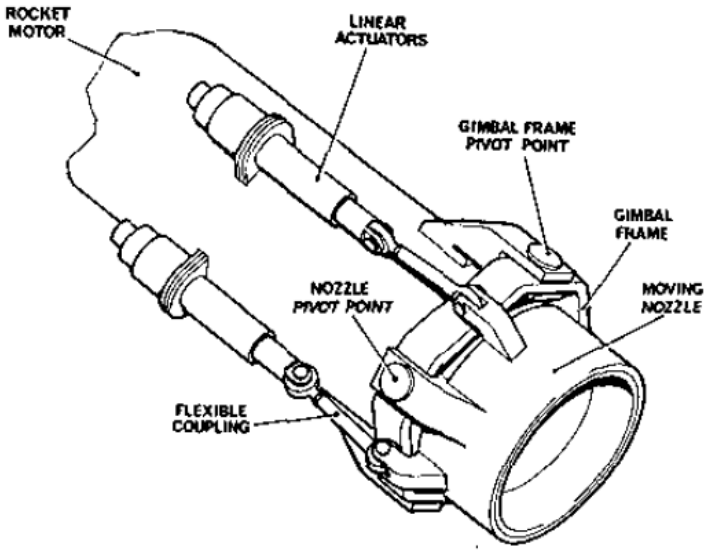

Figure 10. *Schematic of ball & socket nozzle [11]*

1.4.3.1.4 Hinged Nozzle Method

In this method, nozzle is hinged to the rocket motor in one axis only; therefore, in order to control other axis of the system, at least two nozzles are required which is different than other axes.

1.4.3.2 Fixed Nozzle Systems

Fixed nozzle system systems change the direction of thrust vector using secondary fluid injection and mechanical deflectors [8, 12]. Both of these methods have some use in many applications. In most cases, application systems are different than each other while mechanical deflectors are used in small diameter systems like air to air missile, secondary injection methods are preferred in ballistic missiles and large diameter rockets.

1.4.3.2.1 Secondary Injection Thrust Vector Control (SITVC)

In secondary injection method, flow manipulation is accomplished by injecting a secondary fluid inside to the nozzle as shown in Figure 11 which creates shock waves [4-8]. In this way, symmetry of pressure difference on inner wall of nozzle is broken down which expand the flow to the side of the nozzle thus, this action cause a side force on nozzle. This side force forms the thrust vector deflection. SITVC does not need any moving part; therefore, thrust losses are less than mechanically operating TVC systems. SITVC is chosen especially for ballistic missiles and launch systems. SITVC is carried out by different methods [13]. The easiest one is taking secondary injectant from main rocket motor. Another method is using different injectant. In this method, liquid or gas is ejected to the nozzle from a pressurized vessel. The selection of injectant, location of jet, amount of fluid, the selection and number of orifice and the related equipment are important design criteria. SITVC makes some combinations including different types of injectors, injectant fluids, injection location, angle of injection, and types of pressure vessel in order to apply the optimal solution to the specified system.

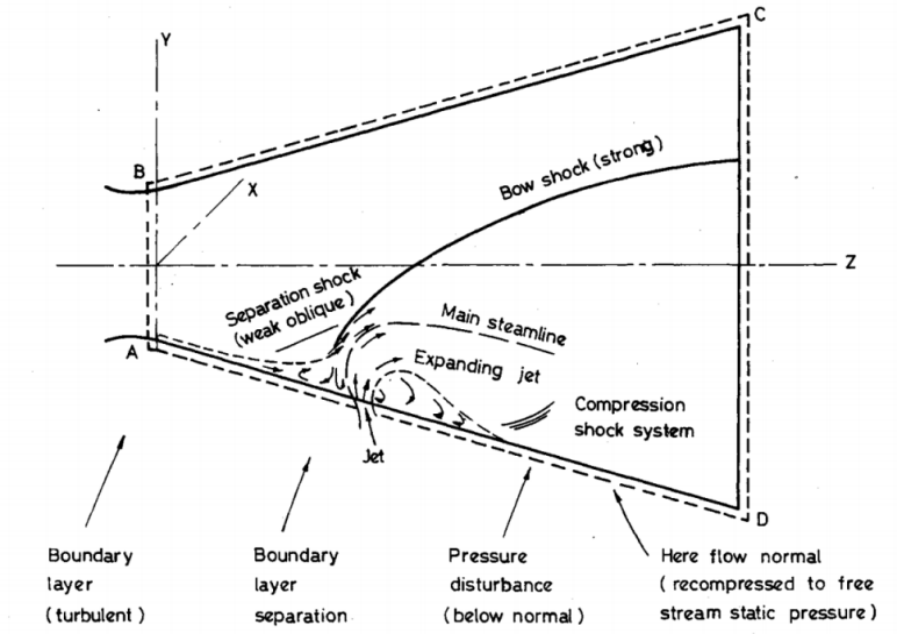

Figure 11. *Schematic of secondary injection method [14]*

1.4.3.2.1.1 Liquid Injection

In this method, inert or reactive liquid is injected into the nozzle. In some systems, liquids are chosen in order to contribute to the thrust of the system. The advantages of the method are rapid response capacity and addition of thrust to the system but the most important disadvantages is total weight of the system.

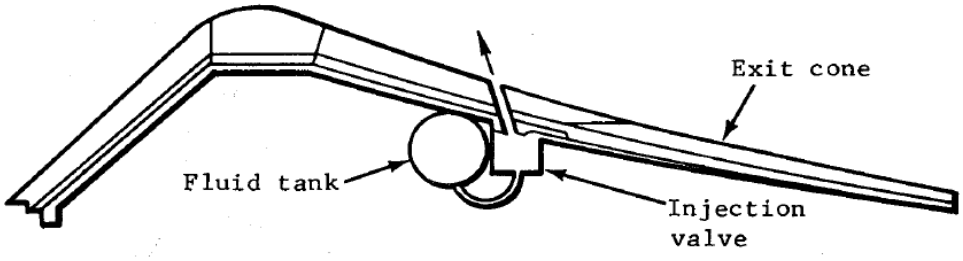

Figure 12. *Liquid injection TVC system [9]*

1.4.3.2.1.2 Gas Injection

In gas injection method, injectant fluid is a gas. Nitrogen is one of the examples. Basics of the method is similar to liquid injection The only difference is instead of feeding a separate fluid, ejecting gas that is taken from the behind of the nozzle as in

Figure 13. The major disadvantages are transportation of excessively hot gas and common leakage problems.

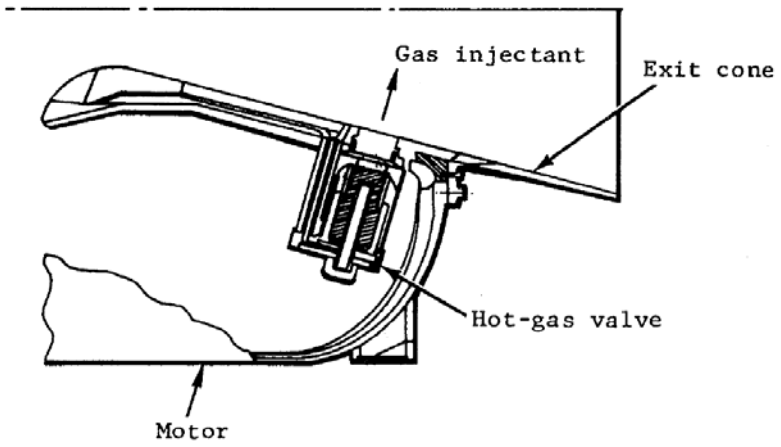

Figure 13. *Gas injection TVC system [9]*

1.4.3.2.2 Mechanical Deflector

Mechanical deflectors alter the main thrust by restraining the flow. The working principle of this method is same as aerodynamics control surfaces. There are three major methods of mechanical deflection of the flow in fixed nozzle categories.

1.4.3.2.2.1 Jet Vane

Jet vane method is one of the oldest methods that were invented for TVC systems. First usage was begun with German V-2 Missile in 1940s [3]. Figure 14 shows the Jet vane that was used in V-2. In this method, vanes are attached to the nozzle exit; thus, the flow is diverted while thrust continues. The notable difference from aerodynamic control surfaces is the vanes that are very small copy aerofins. This method was tried several times and many of applications were developed. (For more information please see Appendix A.1.). Since the surface area of vanes is very small, hinge moments are also small. In addition to these, the jet vane method enables roll control effectively which means that, with a single nozzle, it is possible to control all of the movements of missile.

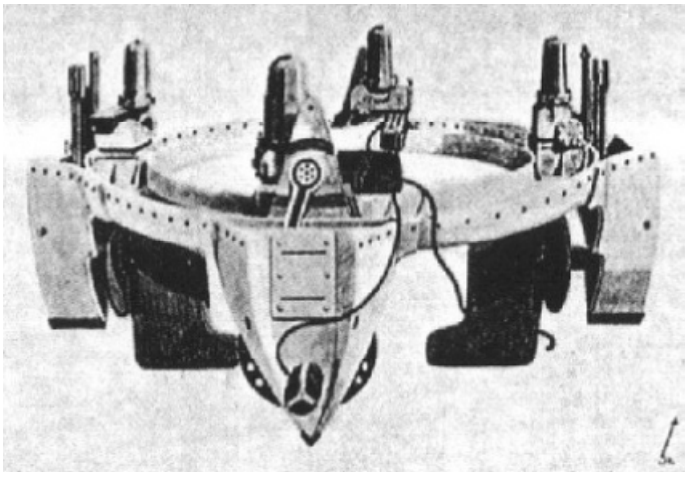

Figure 14. *Jet vanes of German V-2 Rockets [15]*

Thus, total cost of the system is generally low compared to other TVC systems. Critical technologies of jet vane method are development of material and the geometry of the fin because the jet vane imposes very high temperatures so that material has to withstand high temperatures until rocket motor burns out [12], [16]. In several systems, jet vane is disabled after limited time, the ablation of the vanes are studied via simulation and test methods [17].

An experimental study shows that the jet vane method creates the maximum side forces. During experiments, jet vanes are exposed to erosion that makes jet vanes useless but with development of material science, it is possible to develop resistant material [18].

In this method, when fins are deflected at typical angle to exhaust gas, at the surface of the jet vane that meets the flow, oblique shocks waves are developed. While the shock wave increases pressure at this surface, on the opposite side, the expansion shocks cause the decrease in pressure. The pressure difference between these sides provides a force normal to the chord of the vane. The normal force has two components which are lift and drag forces. Lift forces help to control missile whereas drag force results in thrust loses. The high ratio of lift to drag force can lead to the higher performance of the system [19].

Jet vane TVC systems are used in small and large diameter missiles, especially air to air missiles and vertical launched rockets because packaging of the system is easy

compared to other mechanical deflector methods. US's Sea Sparrow [20], Israel's Shavit and Russian Cosmos [21] and Start-1 are some of the examples of vertical launched tactical missile with jet vane TVC system. In addition to this, ejection of this method after launch is another important convenience compared to movable nozzle systems since the weight of the guided munitions is decreased by this ejection. When it is compared to SITVC, capability of maneuverability of jet vane is better than SITVC [20].

Although the movable systems show linear characteristics, the jet vane and SITVC systems are nonlinear. Addition of extra fluid to the nozzle or double the angle of attack of jet vane does not cause doubling of lift forces. Therefore, all the theoretical studies have to be tested experientially [22].

1.4.3.2.2.2 Jet Tab

In jet tab method, tabs are located perpendicular to exhaust stream at the exit of the nozzle as in Figure 15. Generally, jet tabs are coupled with the aerodynamic surfaces. By actuating the tabs, the flow is distracted so desired side force is achieved in order to steer the missile. The significant property of this system is diverting the thrust vector which is proportional to the area of the jet tab.

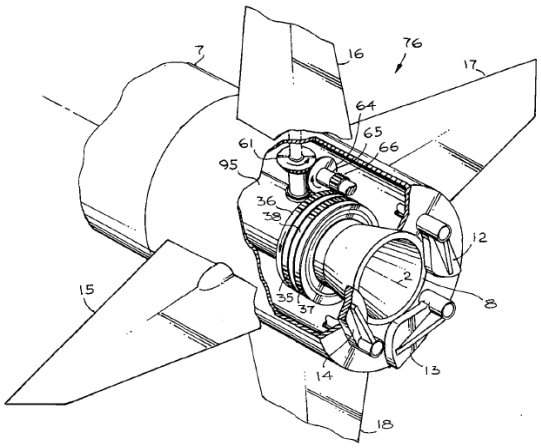

Figure 15. *Jet tab TVC system [23]*

1.4.3.2.2.3 Jetevator

One of the most attractive methods for thrust vector control is a device called jetevator. Jetevator is composed of a spherical ring hinged to the nozzle as shown in

Figure 16. This device swings in and out of the exhaust stream so the demanded response to control servo can be achieved [24]. In addition to this, jetevator can be retracted from the system if there is no need after some time of flight so the degradation of thrust and weight of the system is eliminated. Also by utilizing the curvature of the jetevator, hinge moments and moments of inertia can be held in low values. As in other mechanical deflectors, the development of material that can withstand high temperature during flight is obviously difficult. In recent years, jetevators have been used in fighter aircraft in order to enhance maneuverability.

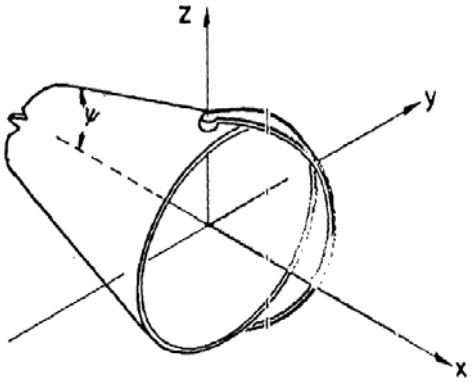

Figure 16. *Jetevator TVC system adapted from* [23]

1.4.3.3 Reaction Control

In reaction control, except from the main motor, small thrusters are used to control the missile. In this method, hot or cold gases can be used. If hot gases are used, special valves, igniters etc. are required whereas in cold gas system, the only need is tank and related equipment to pipe the pressurized gas. The most knowable reaction jet methods are reaction jet, jet interaction, external burning and finally gimbaled motors. Reaction control methods are mostly preferred in space vehicles and satellites.

1.4.3.3.1 Reaction Jet

Reaction jet is one of the most popular reaction control method. Nearly all of the space shuttles and spacecraft are equipped with this method because it enables to control altitude during re-entry, to keep orbit precisely, to make close maneuver

during docking procedures, to control orientation, to point the nose of the craft and finally in order to deorbit the system [25]. Another application area of the reaction jet is projectiles or mortars. In these systems, reaction jets are placed aft section of the body to achieve the desired directional control of the system. General view is that the reaction control decreases the control accuracy for such systems but the main idea here is not to control system precisely only to increase turning capabilities in limited area [26]. In these systems, one shot squibs or pulsed unit are used. [27].

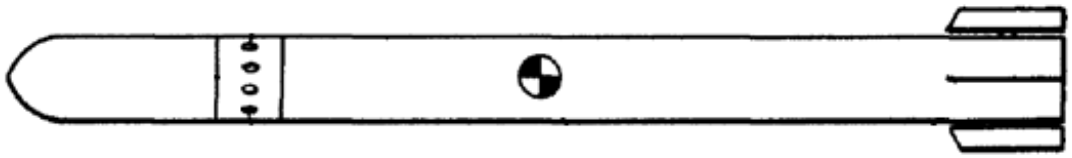

Figure 17. *Projectile reaction jet control system adapted from [27]*

1.5 Basic Concepts of Hybrid Fin Actuation Systems

Fin actuation systems are inevitable parts of missiles. According to applications some systems have different types of control methods as mentioned before. The combination of these methods is called as hybrid fin actuation systems. The elements of methods can be any configuration. The important point of hybrid fin actuation system is being able to control a system without using more than one actuator for a single fin. To illustrate it, if rocket motors burns in 10s, after that since there is no exhaust flow to control, rocket designer needs conventional control method to steer missile during flight. At this point, the movable aerodynamic control surfaces are indispensable. In order to compose conventional aerodynamic control and TVC, different attempts are made [23], [28], [29], [30],[31]. Nowadays, air to air missiles are equipped with these systems and most of them use jet vanes or jet tabs with aero-fins. The implantation of these mechanisms to the system is easy and cost effective; therefore, most advanced air to air missiles such as AIM 9X and IRST-T are designed with hybrid fin actuation systems. In this thesis, aerodynamic control surfaces are coupled with jet vanes.

1.6 Review of the Literature on H_∞ Control

H_∞ control theory is a branch of Robust Control Theory. In order to use H_∞ method, control engineers express the problem statement as mathematical optimization problem and the try to find a controller. In this section, brief history and theory of robust control will be explained.

1.6.1 Historical Background

Control theory is inevitable part of our life. Without control system, it is not possible to develop technologies [32]. All the technologies that surround us are the results of control theory. Control theory can be divided into two main areas which are classical and modern control theories. Although the classical control theory has been used for centuries, the modern control theory is developed around 1950s. With the introduction of Pontryagin's maximum principle in 1956, dynamic programming by Bellman in 1957, and state space representation by Kalman in 1959, modern control theory was founded [33]. The developments of modern control theory opened a new era of control system which is called Robust Control Theory in 1981. The first investigation of the robust control theory was started with Zames [34], where H_∞ optimal control problem was formulated. Then, Doyle at all introduces a state space solution to such problems in 1989 [35] . After that robust control theory has being developed.

1.7 Theoretical Background of Robust Control

Robust control means synthesis of a controller such that this controller makes system stable and guarantees some performance characteristics for an unknown plant with unknown dynamics which is subjected to unknown disturbances [36]. These uncertainties can be any form, but the most important ones are sensor noise, nonlinearity of the system, and unknown dynamics of the plant. In this section, concepts used in robust control are given.

1.7.1 Reasons for Robust Control

For many engineering problems, classical control methods are sufficient enough, but for some systems these methods cannot be defined well or fail to satisfy some

requirements so that designed controller could not provide desired performance. This is because of unknown dynamics and disturbances. In such cases, more powerful design techniques are preferred. The main idea of the robust control is to be insensitive to variation of parameters and able to maintain its stability and performance. The designed controllers meet the desired system requirements in all cases. For that reason sometimes robust control theory are specified as worst case analysis method [36].

1.7.2 Problem Statement

In order to define problem in robust control theory, the following block diagram which is given in Figure 18 is used.

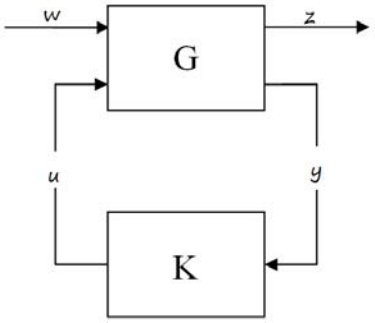

Figure 18. *Standard LTI feedback block diagram*

In Figure 18, G is called generalized plant and K is the controller. The input w is called the disturbance and it contains all the external inputs including reference signals and external noises. The second input u is called actuator and represents the controller signal. The first output z is called cost and represents the error signals which are wanted to be low. And finally, the last output y represents the measurement signals. In this thesis, all the systems are assumed as finite order, linear and time invariant (LTI) according to the formulation given above. The aim is trying to find a controller which makes the system stable and minimize the norms of transfer functions from inputs to errors.

1.7.3 Norms of Systems

In Robust Control Theory, norms are one of the ways that are used to describe the performance and stability of the system. In order to define norm, a real-valued function $\|\cdot\|$ is used if it satisfies the following properties [32].

i. $\|x\| \geq 0$ (positivity) (1.1)

ii. $\|x\| = 0$ iff $x = 0$ (positive definiteness) (1.2)

iii. $\|\alpha x\| = |\alpha|\|x\|$ for any scalar α (homogeneity) (1.3)

iv. $\|x+y\| \leq \|x\| + \|y\|$ (triangle inequality) (1.4)

for any $x \in \mathbb{C}^n$ and $y = X$.

Some signals need special attention for analysis and synthesis. In order to define norm of a system, root-mean-square (RMS) value is needed. Root mean square value is a common method to measure the size of the energy of the signal. [37].

$$\|u\| \triangleq \sqrt{\lim_{T\to\infty} \frac{1}{T}\int_0^T u(t)^2 dt} \tag{1.5}$$

The RMS value of the system in Figure 19, formulated in frequency domain, then RMS value of the system can also be given as [37].

$$\|G\|_{rms} \triangleq \sqrt{\frac{1}{2\pi}\int_{-\infty}^{\infty} |G(j\omega)|^2 \, S_\omega(\omega) d\omega} \tag{1.6}$$

Figure 19. *System G(s) operating on signal w(s)*

where $S_\omega(\omega)$ is the power spectral density of the input. Using above formulation various norms can be defined such as H_2, H_∞ etc. In this thesis, H_∞ norm is used for optimization procedure. H_∞ norm is the maximum magnitude of the G on imaginary

axis which is given as Eq. (1.7)

$$\| G \|_{\infty} \triangleq \sup_{\omega} | \mathrm{G}(\mathrm{j}\omega) | \tag{1.7}$$

1.7.4 Linear Fractional Transformation (LFT)

The LFT has a useful representation that was introduced by Doyle [35]. Consider a plant matrix given in equation (1.8)

$$\begin{bmatrix} A & B \\ C & D \end{bmatrix} := C(\mathrm{sI} - \mathrm{A})^{-1} B + D \tag{1.8}$$

Applying LTI representation to general framework given in Figure 18. According to the given input and out signals, the following relation can be obtained.

$$P = \begin{bmatrix} P_{11} & P_{12} \\ P_{21} & P_{22} \end{bmatrix} \tag{1.9}$$

$$\begin{bmatrix} z \\ y \end{bmatrix} = \begin{bmatrix} P_{11} & P_{12} \\ P_{21} & P_{22} \end{bmatrix} \begin{bmatrix} w \\ u \end{bmatrix} \tag{1.10}$$

The transformation from input u to output z is called the lower linear fractional transformation.

$$z = T_{zw} w = F_l(\mathrm{P}, \mathrm{K})\, \mathrm{w} \tag{1.11}$$

where

$$T_{zw} = F_l(P, K) = P_{11} + P_{21} K (I - P_{22} K)^{-1} P_{21} \tag{1.12}$$

Similarly, upper fractional transformation is found for the system given in Figure 20.

$$F_u(P, \Delta) = P_{22} + P_{21} K (I - P_{11} K)^{-1} P_{12} \tag{1.13}$$

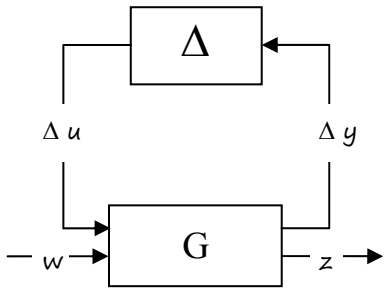

***Figure 20**. Upper fractional transformation*

The H_∞ control problem tries to find a controller that minimizes the infinity norm of an input output map T_{zw} or $\| T_{zw} \|_\infty$ [38].

1.7.5 Sensitivity, Robustness and Feedback Structure

After making all the transformation according to LTF representation, control system can be shown as in Figure 21.

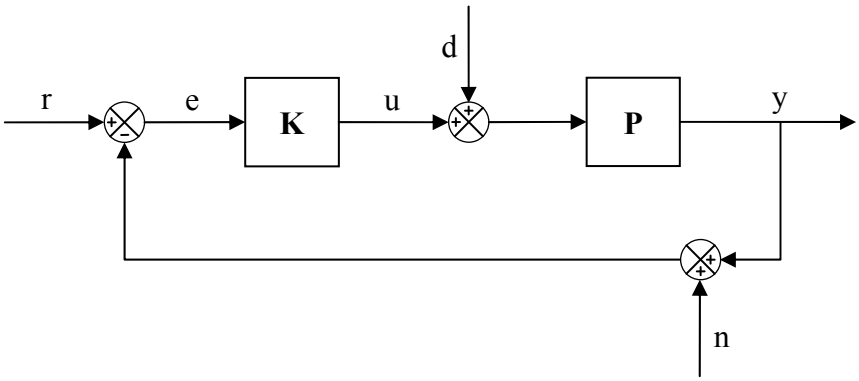

***Figure 21.** Typical feedback loop with disturbances*

In Figure 21, K represents the controller, P is the plant, e is the error signal, d is the disturbance and finally n is the sensor noise. After some algebraic manipulation, transfer function of the system is found as,

$$y = (I + PK)^{-1} PKr - (I + PK)^{-1} PKn + (I + PK)^{-1} Pd \qquad (1.14)$$

where I is the identity matrix. Likewise error signal and input signal can be expressed as

$$u = (I + PK)^{-1} K \{r - d - n\} \qquad (1.15)$$

$$e = (I + PK)^{-1}\{r - d - n\} \tag{1.16}$$

In control terminology, PK is called loop transfer matrix, $(I + PK)^{-1}$ is called output sensitivity matrix 'S' and $(I + PK)^{-1}PK$ is called complementary output transfer matrix 'T'.

$$S = \frac{1}{I + PK} \tag{1.17}$$

$$T = \frac{PK}{I + PK} \tag{1.18}$$

The complementary terms comes from the equality;

$$S + T = I \tag{1.19}$$

S indicates output disturbance input d to the output y. It also describes the tracking error to the reference input. T relates the output of the system to the reference signal. It also indicates how the output is affected by the noise. In a good controller synthesis problem, feedback control system include stability, command following, disturbance rejection, sensor noise attenuation and minimization of control sensitivity. For good command following and disturbance rejection, outputs should track the input reference signals and disturbances inputs have negligible effects upon the outputs. In order to achieve this which means that $y(\mathrm{s}) \simeq \mathrm{r}(\mathrm{s})$ and $e(\mathrm{s}) \simeq 0$, S should be minimized $S \simeq 0$ and $T \simeq I$. For control sensitivity and robustness, T must be small '$T \simeq 0$'. As can be understood from the relation of S and T, both good tracking and noise/disturbance attenuation can be accomplished at the same time. In order to optimize this trade off, one should make the required changes at different frequencies. For low frequencies, T should be made high enough so the disturbance effects are diminished. For high frequencies, T should be small in order to attenuate noise. For detailed information please refer to [38] and [39].

1.7.6 Plant Uncertainty, Stability and Performance

Uncertainty is defined as difference or error between the model and real system. The source of uncertainty may vary from system to system. In some linear system, parameters are known approximately or there can be an error in parameters. Due to

changes and nonlinearities, these parameters may vary again. Another source can be imperfection of measurement devices such as accuracy, linearity, mounting errors etc. These can cause rise an uncertainty on the manipulated inputs. In addition to this, at high frequencies, plant dynamics may be different than identified one. The uncertainty may exceed 100% at some frequency. In some application, although detailed model is available, model reduction techniques can be applied so that some of the dynamics are neglected. These neglected dynamics are also referred as uncertainty. Finally, implementation of controller to the system may differ from the synthesized one. This situation leads to uncertainty in the real system. All these uncertainties may be classified into two main areas [39]:

1. Parametric uncertainty

   In parametric uncertainty, some parameters of the system are unknown. These unknown parameters may be defined in some bounded region $[\alpha_{\min}, \alpha_{\max}]$ than parameter set is defined as

   $$x_p = \bar{x}[1 + r_\alpha \Delta] \tag{1.20}$$

   where $\bar{x}$ is mean value, $|\Delta| \leq 1$ is any scalar and

   $$\mathrm{r}_\alpha = \frac{\alpha_{\max} - \alpha_{\min}}{\alpha_{\max} + \alpha_{\max}} \tag{1.21}$$

2. Neglected and unmodelled uncertainty

   In system, some phenomena are not fully understood so that some of the parameters of the model are missing, usually at high frequencies. Any model will include such type of an uncertainty. These uncertainties may not be defined as in parametric uncertainty.

There are two ways in order to describe uncertainty in a system which are multiplicative and additive uncertainty. The multiplicative uncertainty is expressed as

$$P_p = P_o(I + w_I \Delta_I) \tag{1.22}$$

where P_o nominal plant, P_p is actual plant model and $|\Delta_I(j\omega)| \le 1$. w_I is a weighting function, expressing uncertainty in system. The block diagram representation of multiplicative uncertainty is given in Figure 22.

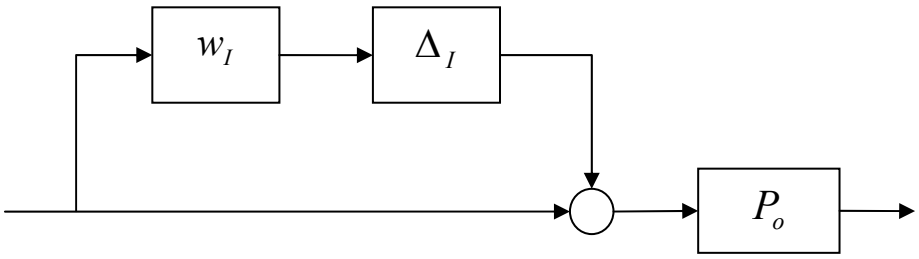

Figure 22. *Multiplicative uncertainty*

The additive uncertainty is defined as

$$P_p = P_o + w_A \Delta_A \tag{1.23}$$

The block diagram representation of additive uncertainty is given in Figure 23.

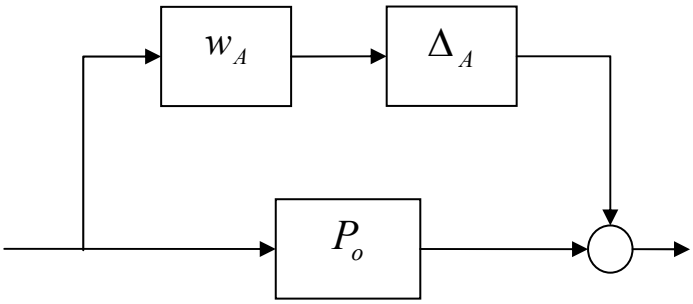

Figure 23. *Additive uncertainty*

These two representations are commonly used to define the uncertainty. The selection of uncertainty types depends on system and information about uncertainty. If absolute error between actual and nominal plant is known, additive uncertainty is chosen but if relative error is known, multiplicative uncertainty is more suitable. For more detailed information about unstructured uncertainty in control system, please refer to [39] and [40].

Consider such a feedback system in Figure 24 with a multiplicative uncertainty of magnitude $|w_I(j\omega)|$

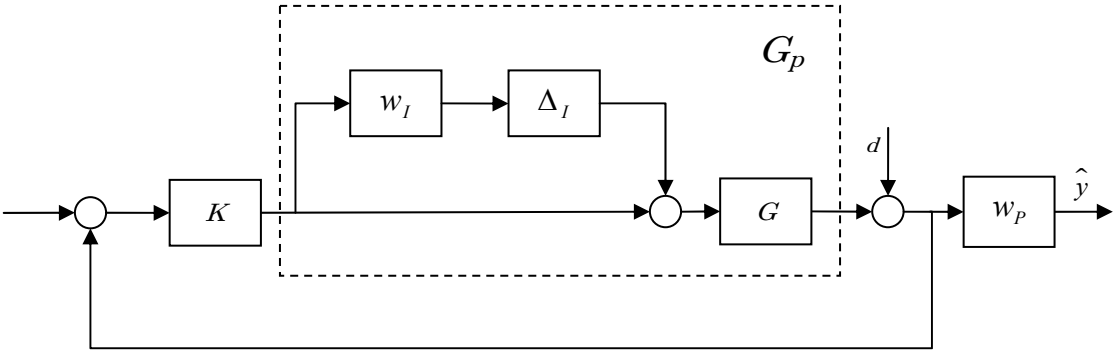

Figure 24. *Feedback system with a multiplicative uncertainty*

Loop transfer function of the system can be written as

$$\begin{aligned} L_p &= G_p K \\ L_p &= (G(I + w_I \Delta_I))K \end{aligned} \tag{1.24}$$

and $|\Delta_I(j\omega)| \le 1, \forall \omega$

The robust stability theory assumed that the normal closed loop system is stable. For simplicity, the loop transfer function L_p is also stable. According to the Nyquist stability condition, L_p should not encircle the point -1, $\forall L_p$ as in Figure 25.

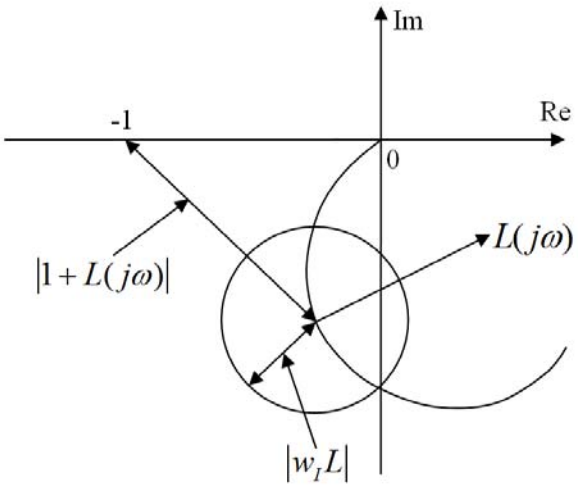

Figure 25. *Nyquist plot of L_p for robust stability* [39]

As can be understood from the Nyquist plot, the disk with radius $|w_I L|$ is smaller than the length $|1+L|$, and then the robust stability condition is satisfied for the system.

$$\begin{aligned} RS \;&\Leftrightarrow\; |w_I L| < |1+L|,\ \forall\omega \\ &\Leftrightarrow\; \frac{|w_I L|}{|1+L|} < 1,\ \forall\omega \;\Leftrightarrow\; |w_I T| < 1,\ \forall\omega \end{aligned} \tag{1.25}$$

where $T = GK(1+GK)^{-1}$

$$\|w_I T\|_\infty < 1 \tag{1.26}$$

In order to define robust performance, the SISO system that is given in can be used.

Before defining robust performance problem, firstly nominal performance must be satisfied.

$$NP \;\Leftrightarrow\; |w_P S| < 1,\ \forall\omega \;\Leftrightarrow\; |w_P| < |1+L|,\ \forall\omega \tag{1.27}$$

Then for all possible plants, including worst condition plant parameters, robust performance is defined as

$$\begin{aligned} RP \;&\Leftrightarrow\; |w_P S_p| < 1, \qquad \forall\omega, \forall S_p \\ &\Leftrightarrow\; |w_P| < |1+L_P|, \quad \forall\omega, \forall L_p \end{aligned} \tag{1.28}$$

Graphical representation of robust performance is given in Figure 26.

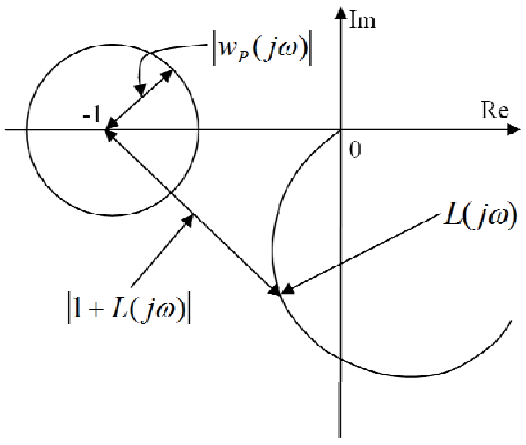

Figure 26. *Nyquist plot of nominal performance condition [39]*

As can be seen from the Figure 26, $L_P(j\omega)$ should not cross the circle with radius $|w_P(j\omega)|$ centered on point -1. The distance between the centers of the disk describe the robust performance, then the robust performance condition becomes

$$\begin{aligned} RP \quad &\Leftrightarrow \quad |w_P| + |w_I L| < |1 + L|, \qquad \forall \omega \\ &\Leftrightarrow \quad |w_P(1+L)^{-1}| + |w_I L(1+L)^{-1}| < 1, \quad \forall \omega \end{aligned} \tag{1.29}$$

1.7.7 Solution to H_∞ Problem

In H_∞ theory, solution to H_∞ problem can be defined in two different ways. The first one is optimal H_∞ controller which is defined as "find all admissible controllers K(s) such that $\|T_{zw}\|_\infty$ is minimized". But it is not possible to a find such controllers especially for MIMO systems. Thus, different type of solution is defined as:

"for a given $\gamma > 0$, find all admissible controllers K(s), it there are any such that $\|T_{zw}\|_\infty < \gamma$ ".

This statement defines suboptimal control. Suboptimal H_∞ solution is very close to optimal one in norm sense and much cheaper to find such controllers. In addition to these, to find an optimal controller is not a practical way and sometimes it is unnecessary [41]. From all these reasons, suboptimal control solution is given in this section. In literature, one of the most known algorithms is presented by Glover and Doyle. This algorithm finds a family of controller such that

$$F_l(P,K) \le \gamma \tag{1.30}$$

The plant G can be represented as

$$G(s) = \left[\begin{array}{c|cc} A & B_1 & B_1 \\ \hline C_1 & D_{11} & D_{12} \\ C_2 & D_{21} & D_{22} \end{array}\right] \tag{1.31}$$

In order to ensure a solution, the following assumption must be made

- **i.** (A, B_2) is stabilizable and (C_2, A) is detectable.
- **ii.** (A, B_1) is controllable and (C_1, A) is observable.

iii. $D_{12} = \begin{bmatrix} 0 \\ I \end{bmatrix}$ and $D_{21} = \begin{bmatrix} 0 & I \end{bmatrix}$

iv. $D_{11} = 0$ and $D_{22} = 0$

After these assumptions the problem is simplified as

$$G(s) = \left[\begin{array}{c|cc} A & B_1 & B_1 \\ \hline C_1 & 0 & D_{12} \\ C_2 & D_{21} & 0 \end{array}\right] \tag{1.32}$$

The solution of H_∞ includes the following two Hamiltonian matrices

$$H_\infty = \begin{bmatrix} A & -\gamma^2 B_1 B_1^* - B_2 B_2^* \\ -C_1 C_1^* & -A^* \end{bmatrix} \tag{1.33}$$

$$J_\infty = \begin{bmatrix} A^* & \gamma^2 C_1^* C_1 - C_2^* C_2 \\ -B_1 B_1^* & -A \end{bmatrix} \tag{1.34}$$

Iff the following conditions are met, it is possible to find a admissible controller such that $\|T_{zw}\| < \gamma$

i. $H_\infty \in dom(Ric)$ *and* $X_\infty := Ric(H_\infty) > 0$

ii. $J_\infty \in dom(Ric)$ *and* $Y_\infty := Ric(H_\infty) > 0$

iii. $\rho(X_\infty Y_\infty) < \gamma^2$

The controller is in the following form

$$K_{sub}(s) := \begin{bmatrix} \hat{A}_\infty & -Z_\infty L_\infty \\ F_\infty & 0 \end{bmatrix} \tag{1.35}$$

where

$$\hat{A}_\infty := A + \gamma^{-2} B_1 B_1^* X_\infty + B_2 F_\infty + Z_\infty L_\infty C_2$$
$$F_\infty := -B_2^* X_\infty$$
$$L_\infty := -Y_\infty C_2^*$$
$$Z_\infty := (I - \gamma^{-2} Y_\infty X_\infty)^{-1}$$

1.8 Literature Review of the Electro-Mechanical Actuator Control

In many aerospace applications such as missile, aircraft etc., electromechanical actuators are widely used; therefore in literature there are numerous papers about electromechanical actuator control. In this section, previous works about electromechanical actuators especially for missile fin control are given.

In 1992, Hartley designed a reduced fourth order H_∞ controller for electromechanical actuator of tail control missile whose frequency response characteristic is similar to seventh-order H_∞. With this work Hartley intends to reduce requirements of microprocessor [42]. In 1993, Hartley tested a H_∞ controller on single axis prototype electromechanical actuator and made some comparison between classical and H_∞ controller design [43]. In 1994, Malassé at all designed an H_∞ control law for a testing bench which is based on coprime factors and compared obtained results with LQG and LQR/LTR designs [44]. Adam and Guestrin made experimental studies on servo motors. They designed a robust controller and stated the results about the performance of their system [45]. Luo and Fan (2003) [46] and Ölçer [47] introduced a mixed H_2 / H_∞ controller that combines both H_2 performance and H_∞ stability for missile electromechanical actuator. They showed simulation and analytical results to the change of parameter and perturbation. Daş [48] made experiments on fin actuation system and presented the multi-loop robust controller. Yoo at all designed an H_∞ controller for an electromechanical fin actuator system using the mixed sensitivity H_∞ control method. The effectiveness of the controller was verified through simulations and experiments [49]. In 2006, Eker studied a sliding mode controller with PID sliding surface and applied his controller to an electromechanical actuator test bench. He compared the solutions with conventional PID and showed controller's tracking performance and robustness [50]. One of the most notable studies about electromechanical actuator is made by Schinstock at all They developed a nonlinear model of thrust vector control of rocket engines and made experiment to verify the model of the actuator [51] [52] [53]. Other important studies were presented by Ristanović. They made experimental studies to improve the performance of the aerofin control system using both conventional and modern control techniques. They tried intelligent control techniques and nonlinear PID

controllers to validate their research experimentally [54] [55] [56] [57]. In addition to these, some applications are achieved by using DSP. Jeong at all (2007) [58] and Khan, Todic, Milos, Stefanovic, Blagojevic (2010) [59] made research about digital controllers and propose a controller for digitally controlled missile actuator. Beside these, variable structure control is used in missile actuators. Robustness of a variable structure makes it important. Gao, Gu and Pan (2008) [60] and Li and Sun (2010) [61], Liu, Wu, Deng and Xiao [62] made research on variable structure control.

CHAPTER 2

SYSTEM MODELING AND IDENTIFICATION

2.1 Modeling of the System

Fin actuation systems steer the missile according to the commands taken from the guidance unit. The output of the guidance unit is the reference input to the control unit which adjusts the position of the fin actuation elements such that a missile tracks the commanded motion as closely as possible. The fin actuation system (FAS) is a closed loop type control unit since the information of the actual position of fins is supplied to the control unit by the position sensors. Then the fin deflection data are taken by the guidance autopilot. The related calculation is made according to the aerodynamics principles in guidance unit. After that, autopilot finds the deviation from the target using its gyroscope and accelerometer data. In order to enhance the precision level of target tracking, other type of sensors are used which is called as seeker unit of missile. Seekers can be IR, IIR, radar antennas or laser. These seekers can be used individually or used together as in dual mode seeker. Finally, the corrected fin position command is generated by the autopilot and this procedure continues until the missile hits the target.

The surface arrangement of the AAM is cruciform X-arrangement as presented in section (1.4.2). The back side view of the missile given in Figure 27. During the flight of the missile, fin actuation system must overcome the forces shown in Figure 27. In this study, fin actuation system is composed of brushless DC motor (BLDC), a position sensor, gear train and a proper 4-link (PPRR linkage) mechanism. Because

of the physical restrictions of the missile geometry, position sensor is attached to the motor side.

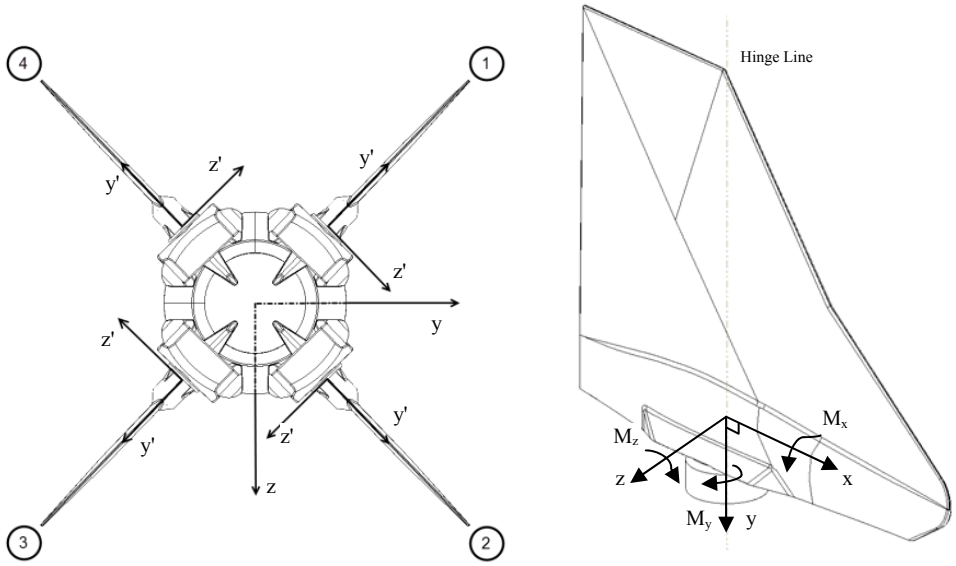

Figure 27. *Backside view of AAM and coordinate frame of a fin*

2.2 Mathematical Models of System

2.2.1 Motion Transmission Mechanism

The physical representation of the mechanism is given in Figure 28. In this system motor drives the gear pair. One of the gear is attached to the ball-screw so that linear motion can be obtained. Then this linear motion is converted to rotational motion using a proper 4-link mechanism that is given below. As can be understood from the Figure 28, rotation of motor $'\theta_m'$ is input, the deflection of the fin $'\delta = \theta_{12}'$ is the output of the system. The output shaft *'fin shaft'* is also attached to jet vane with a parallelogram so that it is possible to drive the jet vanes without any additional actuator to the system.

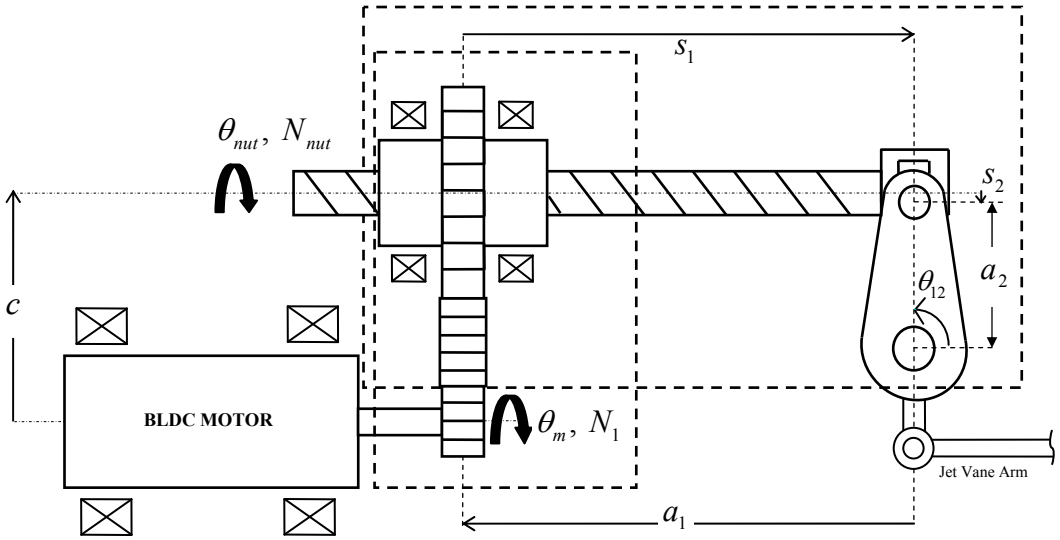

Figure 28. *Schematic diagram of the FAS*

During motion transmission, motor drives gear train. The output gear is integrated with ball screw, thus input to the ball screw results in a linear motion of the screw. Then, this motion is converted to the rotation by using a proper four-link mechanism and finally the output shaft is coupled to the jet vane shaft with a parallelogram.

In order to obtain mathematical model of the mechanism, firstly one should write the loop closure equation (LCE) of the system.

$$-a_1 + ic + s_1 - is_2 = a_2 e^{i\theta_{12}} \tag{2.1}$$

where $i = \sqrt{-1}$. Decomposing equation (2.1) into real and imaginary part gives the following relationship:

$$\begin{aligned} -a_1 + s_1 &= a_2 \cos(\theta_{12}) \\ c + s_2 &= a_2 \sin(\theta_{12}) \end{aligned} \tag{2.2}$$

Note that in Figure 28, the input to the system is given θ_m, therefore, the relationship between the mechanism and gear train should be defined. From Figure 28, the input to the gear train is θ_m, and the output is the gear nut of the ball screw. Then the gear ratio between input and output of the gear train is written as

$$\theta_{nut} N_{nut} = \theta_m N_1 \tag{2.3}$$

Now, the relation between gear train and mechanism can be defined. Before defining this relation, one must understand the ball screw working principle. Ball screw is a mechanical component that converts rotational motion into linear motion. They are used to move things or transfer forces. In this application, force is transferred to the mechanism.

A ball screw is composed of the three components which are

- Balls
- Nut 'including mechanism to recirculate balls'
- Screw shaft

Ball screws are preferred in missile fin actuation system because of high load capacity, high efficiency and low friction. The pitch of the screw shaft defines the transmission ratio between nut and screw. For this application the pitch 'p' is chosen as 2 mm per revolution. In this manner, the transmission ratio between nut rotation and the linear motion 's' is given as

$$s = s_0 + \frac{p}{2\pi}\theta_{nut} \tag{2.4}$$

To calculate the transmission ratio of the mechanism, one should make the velocity analysis of the system using equation (2.2).

$$\begin{aligned} \dot{s}_1 &= -a_2\dot{\theta}_{12}\sin(\theta_{12}) \\ \dot{s}_2 &= -a_2\dot{\theta}_{12}\cos(\theta_{12}) \end{aligned} \tag{2.5}$$

In this study, FAS is capable of moving ± 25° mechanically. This yields

$$65° \le \theta_{12} \le 115° \tag{2.6}$$

After finding the velocities of the components, the transmission ratio of the system can be written as using equations (2.1-2.5).

$$\mathrm{N} = -\frac{N_3}{N_1}\frac{2\pi}{p}a_2\sin\theta_{12} \tag{2.7}$$

Table 1. *Parameters of mechanism*

a_1	53 mm
a_2	22 mm
N_1	19
N_3	61
p	2 mm

Using system parameters given in Table 1 and equation (2.7), transmission ratio for each θ_{12} value is obtained as given in Figure 29.

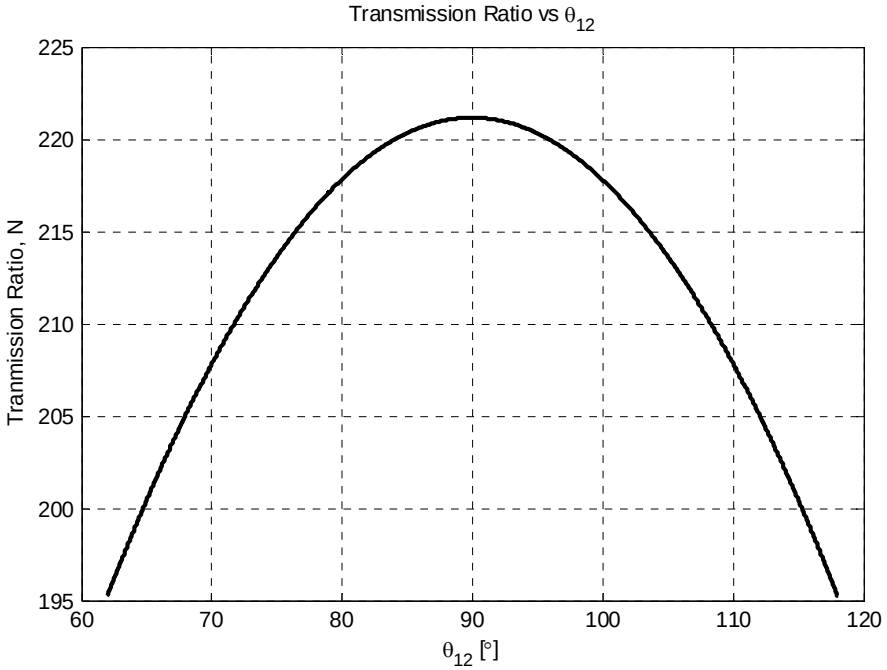

Figure 29. *Transmission ratio of the system*

2.2.2 Sensors

One of the most important parts of the system is sensor; therefore, selection of sensor is a critical aspect. In order to make the right choice, sensor must be capable of minimum system requirements such as accuracy, resolution and geometrical constraint. All these properties have physical meaning. After all the properties are decided, selection of sensor could be made easily. In this study, rotary incremental

encoder is used to measure the motor output shaft position and then estimate the output shaft position of the fin. Because of the physical limitations, the sensor is attached to the motor output shaft. In literature, for system including gears, the sensor is attached to motor side or load side. According to the [63] and [64], the systems including gear pairs with backlash, the position is preferred to be measured from the input shaft which means that the location of the sensor seems well. The incremental encoder is a digital type sensor and works in 500 pulse per revolution (ppr) resolution and the maximum operating frequency is 200 kHz.

2.2.3 DC Motor

In this study, brushless DC motor is used to drive the system because brushless DC motors provide several advantages such as [65]:

- They can operate at higher speeds and at full torque. For this application, speed and torque is relatively high when the geometrical limits are considered. Especially high speed operation cause problems in brushed motor because the motor are switched by brushes which is destructive and shortens the life of the motor.
- For long-life applications, absence of brushes normally increases the life of the motor.
- Brushless DC motors are free of the EMI (Electromagnetic Interference) contributors to the system which is very important for aerospace application. In brushed DC motor, interface between brushes and rotor generates arc which increases the EMI interface.
- For explosive environments, brushless motors can be used without any special housing elements.
- The brushless motors require less preparation than brushed motors.
- They provide high starting torque and variable bi-directional speed.

Another important property of brushless DC motor is the linear characteristics. This is very helpful to define torque output. In brushless motor, input to the system is current and the output is the torque which is directly related with input torque as given in equation (2.8)

$$\tau_m = K_t i \tag{2.8}$$

In order to obtain mathematical model of the motor, equivalent circuit of the DC motor is taken as shown in Figure 30.

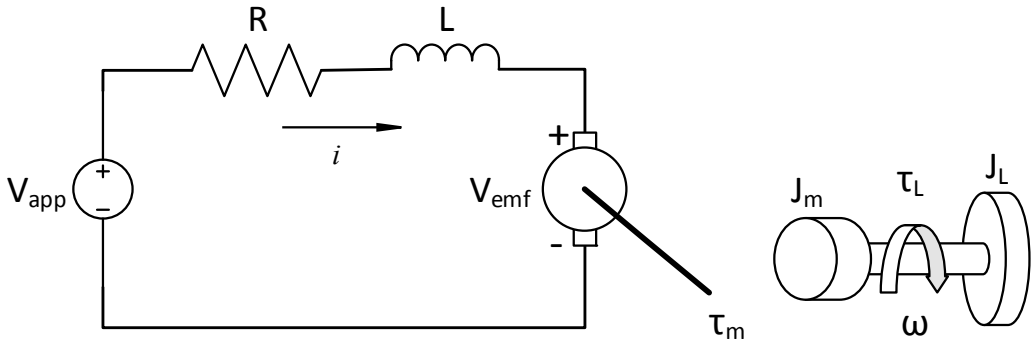

Figure 30. *Equivalent circuit of the DC motor*

Now, using Kirchhoff Voltage Law, equation of the motor can be obtained as

$$V_{app} = Ri + L\frac{di}{dt} + V_{emf} \tag{2.9}$$

where $V_{emf} = K_b\omega$ and K_b is back-emf constant. Mechanical part of the motor equation is obtained as

$$J\frac{d\omega}{dt} + B\omega + \tau_L = \tau_m \tag{2.10}$$

where $J = J_m + J_L$ is the equivalent moment of inertia. Using equations (2.8), (2.9), (2.10) and Laplace transform, transfer function of the motor can be found as

$$\frac{\omega(s)}{V_{app}(s)} = \frac{K_t}{(R+Ls)(Js+B)+K_bK_t} \tag{2.11}$$

but this expression is written from motor voltage 'V_{app}' to motor speed 'ω' . In this application, the position is controlled thus transfer function must be arranged like that

$$\omega = \dot{\theta},\ \omega(s) = s\theta(s) \tag{2.12}$$

$$\frac{\theta(s)}{V_{app}(s)} = \frac{K_t / LJ}{s^3 + (\frac{R}{L} + \frac{B}{J})s^2 + (\frac{RB + K_b K_t}{LJ})s} \tag{2.13}$$

The block diagram of the transfer function given in the equation (2.13) can be presented as follows

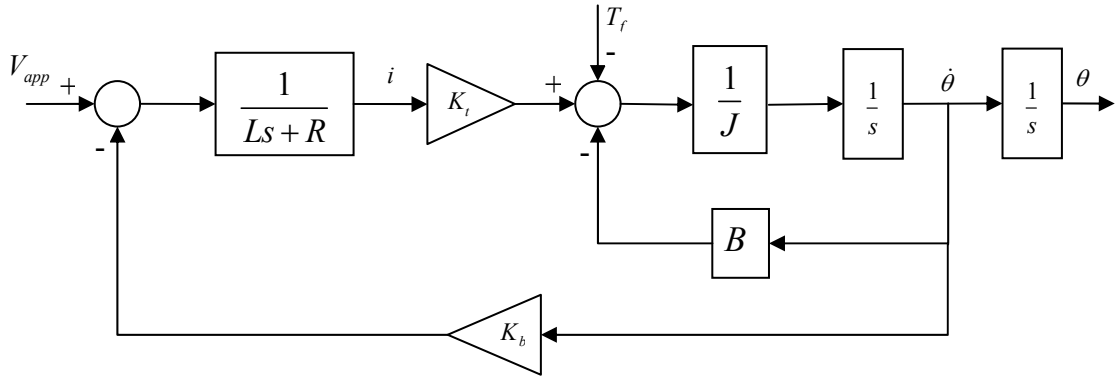

Figure 31. *Block diagram of the DC motor between voltage and motor position*

In this application, precision position control is required to drive the motor so that analog servo drives are used. The working principle of the drive is to transmit the low energy signal from controller to high energy signals [66]. Generally input to the these types of drivers is voltage but in servo drive, the input command voltage controls the output current which means that in reality output of the controller is current. In many applications transfer function of the drive is taken as a constant number 'K_s'. Using this constant in equation (2.13)

$$\frac{\theta(s)}{V_{app}(s)} = \frac{K_t K_s / LJ}{s^3 + (\frac{R}{L} + \frac{B}{J})s^2 + (\frac{RB + K_b K_t}{LJ})s} \tag{2.14}$$

As mentioned before, the servo drive's input is voltage but it makes transformation between voltage and current according to its transfer function $K_s[V / A]$. Another important property of the servo drive is sampling time of the driver. In this application, driver is much more faster than system whose frequency is 33 kHz so that it is possible to simplified the equation (2.14) as

$$G(s) = \frac{\theta_{motor}(s)}{I(s)} = \frac{K_t}{s(J_{eq}s + B_{eq})} \tag{2.15}$$

where J_{eq} is the equivalent moment of inertia of FAS and B_{eq} is equivalent viscous friction of the system. As can be seen from equation (2.15), the parameter K_s is also excluded from equation because K_s is only needed in real system test in order to apply right command signal to physical system using xPC Target® environment. This plant is used for the rest of the thesis for both identification and controller synthesis. Some of the parameters that is given in equation (2.15) are unknown. These are motor torque constant 'K_t' and equivalent inertia 'J_{eq}' of the system. K_t is given in motor catalog as $K_t = 10000\frac{kg \cdot mm^2}{s^2 A}$. J_{eq} is also found by using the following mathematical relation:

$$J_{eq} = J_{rotor} + J_{gear1}^{eq} + J_{gear2}^{eq} + J_{nut}^{eq} + J_{ball-screw}^{eq} + J_{shaft}^{eq} + J_{jet-vane}^{eq} \tag{2.16}$$

$$J_{gear1}^{eq} = \frac{J_{gear1}}{\left(N_2 \diagup N_1\right)^2} \tag{2.17}$$

Similarly, $J_{ball-screw}^{eq}$ is found as

$$\begin{aligned} \frac{1}{2} m_{ball-screw} \dot{s}_1^{\,2} &= \frac{1}{2} J_{ball-screw}^{eq} \theta_m^{\,2} \\ m_{ball-screw} \left(\frac{\theta_m}{N_2} \frac{p}{2\pi} \right)^2 &= J_{ball-screw}^{eq} \theta_m^{\,2} \\ J_{ball-screw}^{eq} &= m_{ball-screw} \left(\frac{N_3}{N_1} \frac{p}{2\pi} \right)^2 \end{aligned} \tag{2.18}$$

At the end of the calculation with the help of the CAD software, equivalent inertia of the system is found as $J_{eq} = 5.65 kg \cdot mm^2$.

In this thesis, in order to simplify the indication of the system, parameters are not shown term by term. Instead of it, the following relationship is used.

$$G(s) = \frac{K_p}{s(T_p s + 1)} \tag{2.19}$$

where $K_p = K_t / B_{eq}$ and $T_p = J_{eq} / B_{eq}$ .Thus it is possible to use the process model of identification toolbox.

2.2.4 External Loads and Disturbances

As mentioned before, the external disturbances are aerodynamic forces on the fin which is called hinge moment and the variable environmental conditions. Viscous friction of the system changes according to environmental conditions. In robust control design, the uncertainty can be defined for this parameter. In addition to these, motor cogging torque can be thought of another source of disturbance which is not taken into account in this thesis actually. Estimated maximum hinge moment for this system is 30 Nm at the fin side but this value can randomly alter during the flight of the missile. Continuous operation point is nearly half of the stall torque.

$$\left| T_{hinge} \right| \leq 30 \ Nm \tag{2.20}$$

For the motor side, the maximum hinge moment is divided by the transmission ratio thus continuous and stall torques at the motor side can be calculated.

2.3 System Identification

System identification means obtaining the dynamic model of the system by using experimental data [67]. For any physical system, there are two basic approaches to find the mathematical model of the system. The first one is analytical. Using proper mathematical manipulation and physical laws, it is possible to obtain mathematical model of the system. The second way relies on experiment. In this method, measurements of the system inputs and outputs are used to identify the system. Basic block diagram of the system identification process is given in Figure 32.

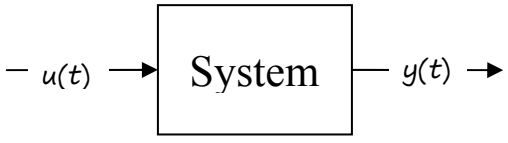

Figure 32. *A dynamic system with input u(t) and output y(t)*

Mathematical modeling and system identification approaches are compared in many cases. In many systems, processes are so complex that it is not possible to find a well-defined mathematical model using physical laws. In such a situation, system identification techniques are preferred. In some cases, identification techniques can be used to find an unknown parameters of the system that is modeled analytically thus unknown parameters of the system are easily estimated. The obtained model by system identification has following properties which are different than model based on mathematics [68].

- The models have limited validity because it is not possible to identify a system exactly; therefore, engineers try to define a working range for a certain process and then they try to identify system in this defined range.
- In most cases, models have physically meaningless parameters. These parameters are used to describe the system's overall behavior not the system itself physically.
- Construction and usage of models are quite easy.

Before starting identification procedure, one must know that identification process is not an exact methodology thus the following important points should be taken into account carefully [68].

- For good estimations, appropriate mathematical models must be defined firstly.
- During data collection procedure, signal noises and other effects from physical world must be taken into consideration.
- All the processes may change with time depending on the working conditions, environment etc. In order to obtain time-invariant models, these are thought carefully.
- In several applications, some signals and variables cannot be measured properly.

Identification of a system is rather complex procedure. The identification experiment is carried out by exciting the system using proper signals such as impulse, step, random input etc. It is not possible to use all the signals for identification; therefore, the input signal must be chosen carefully according to following properties.

- The signal must be rich enough in order to guarantee that system can be identified for intended use.
- The amplitude of the input signal must be higher than noise of the output sensor.

Another important point of system identification is determination of sampling frequency. All the identification procedure is carried out using computer controlled system. This causes some information loses in sampling signals. In many applications sampling frequency must be at least 10 times higher than the bandwidth of the system but if there is an uncertainty in the system, sampling frequency should be selected as high as possible where the physical system permits, thus accuracy can be maximized. Then this data can be downsampled to desired value using digital filter and decimation [69].

Input types that can be used for system identification are given below.

- *Impulse:* Ideally, impulse has infinitely high amplitude over zero duration. It includes all the frequency range but it cannot be achieved practically. Thus engineers try to obtain a very large peak during in small time interval. Impulse signal is generally used for structure identification.
- *Step:* One of the most commonly used signals. Signal to noise ratio in high frequency band is low in step signal thus step signal is used to stimulus a slow process or a slow physical system [70].
- *White Noise:* White noise or random signal is type of a signal that whose amplitude varies randomly. Theoretically, this signal has flat frequency response for whole spectrum but for real, limited bandwidth systems, it is not possible to achieve this. Important property of white noise, in a certain range, is that it excites all the modes of the system. Generally, white noise is used to identify electronics.
- *Chirp:* A chirp signal is a varying frequency sinusoid. It is suitable when frequency response within a certain range is needed.
- *Pseudo Random Binary Sequence (PRBS):* A PRBS signal is random sequence of rectangular pulses. Its amplitude changes between two values. The signal sequence repeats every $2^n - 1$ values.

In this thesis, the FAS's reference input is output angle of the fin. This fin is mechanically limited at ± 25°. Therefore, the amplitude of the signal is chosen such that the system should not hit the limits. In addition to this, input signals are arranged such that outputs without any saturation are obtained satisfactorily by a trial and error method. Two examples of the input signal and the measured output signal are given in Figure 33 and Figure 34.

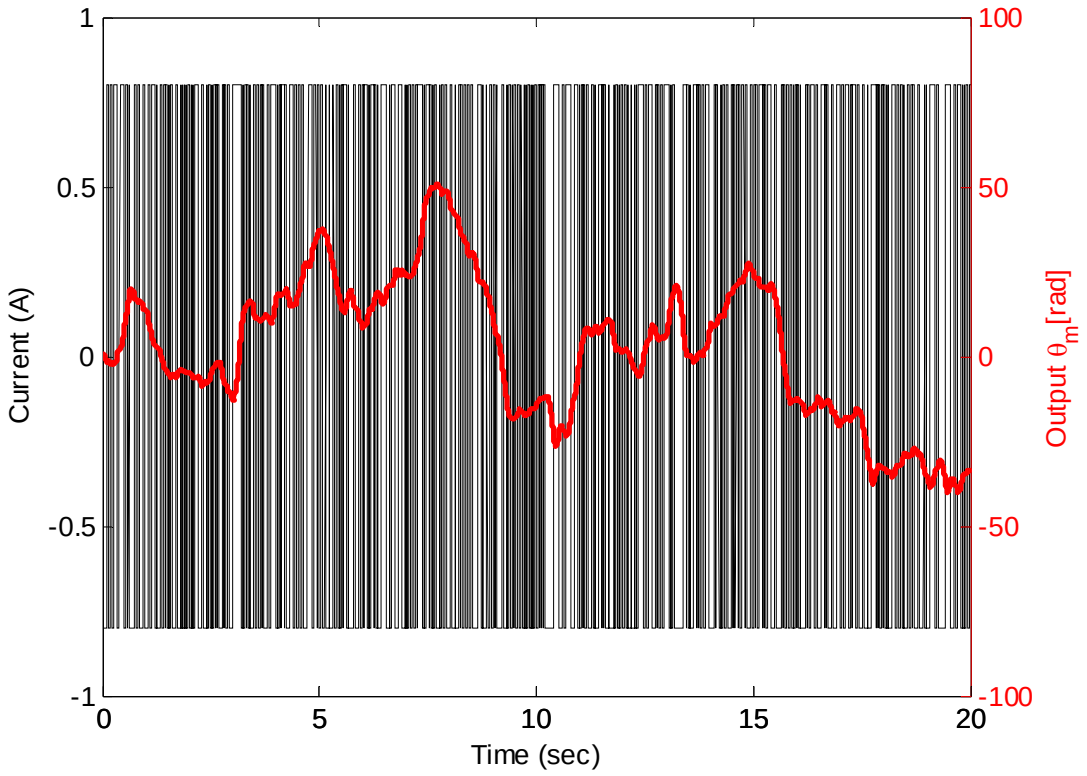

Figure 33. *A PRBS input signal used in system identification*

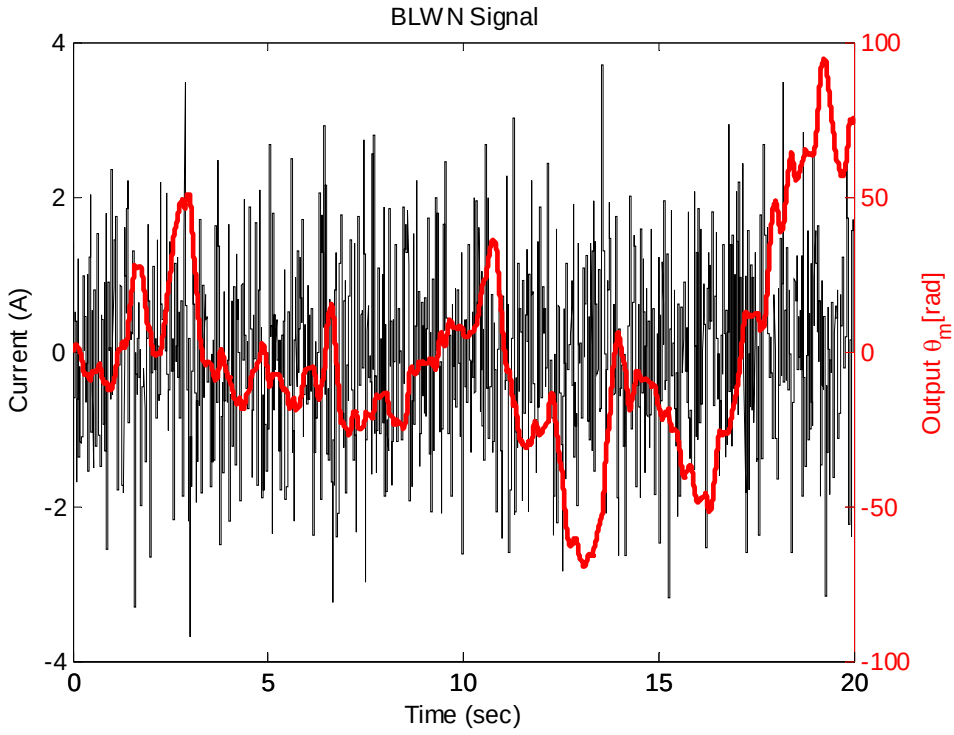

Figure 34. *A BLWN input signal used in system identification*

Another important point is the frequency content of the input signal. In order to make the identification process satisfactorily, the input signal is formed such that at least two modes of the system should be excited since the identification model used in this thesis is a second order model. In some cases, the input signal is created such that the controller bandwidth remains within this frequency. This approach remains on the safe side. The frequency content of the above signals are given respectively in Figure 35.

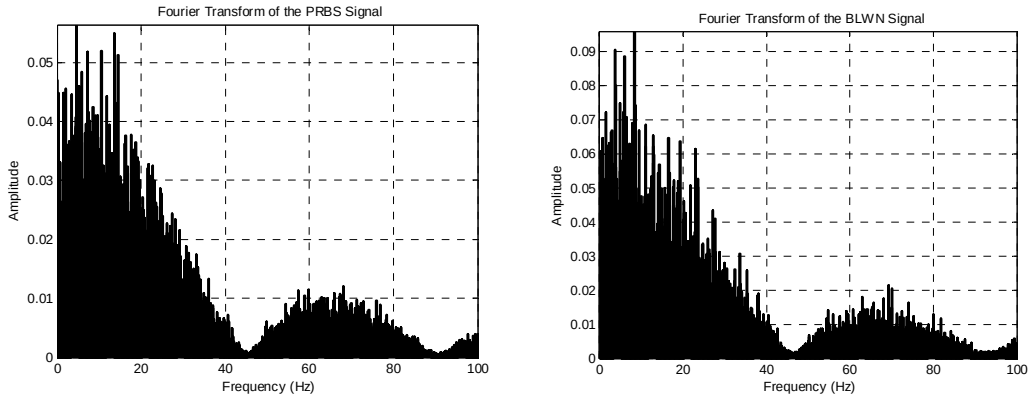

Figure 35. *Frequency spectrum of the input signals*

During the system identification experiment, a MATLAB® and the real time xPC Target® module are used in order to collect input/output signal of the system. In this application, input signal is a current that is applied to the motor in units of Amperes and output signal of the system is angular position of the motor measured by rotary incremental encoder. All the input/output signal sets used to identify the mechanical system are given in Appendix A.2. Besides, the frequency spectrum of these input/output signal sets are also presented in Appendix A.3. In order to obtain satisfactory results, identification procedure could be performed in two-stage. In first stage, the system, or motor itself is tried to be identified using feasible PRBS or BLWN signal. Then, using obtained data, model of the system could be obtained. Using this model, new input signals could be generated in simulation environment in order to guarantee that the outputs of the system moves within the physical limits. In second stage, newly generated signals are applied to the system in order to identify the system more properly. At the end of this procedure, better results could be achieved in a short time. In this thesis, firstly the motor and the gear pair are identified, and then the total system is identified using System Identification Toolbox™ of MATLAB®.

System Identification Toolbox™ could be used to identify continuous or discrete time system both in time domain and frequency domain. In this thesis, frequency domain input-output data are preferred for identification process. Before running the toolbox, some of preliminary preparation must be done. Firstly, all collected time domain data must be transformed into frequency domain data. To do this, *'tfestimate'* command can be used. Then, the required frequency part of the data is filtered. For this application, 30-40 Hz frequency band gives satisfactory results so that high frequency modes can be neglected. Usage of toolbox is also easy. In order to use the toolbox whose image is given in Figure 36, procedure that is given below can be followed.

- Toolbox is run using *'ident'* command.
- Frequency or time-domain data are imported to toolbox using import data tab.
- One of the data is chosen as validation data and the others are picked as working data one by one.

- Using estimate tab, any model type can be chosen. In this thesis, process model is selected to describe the system.

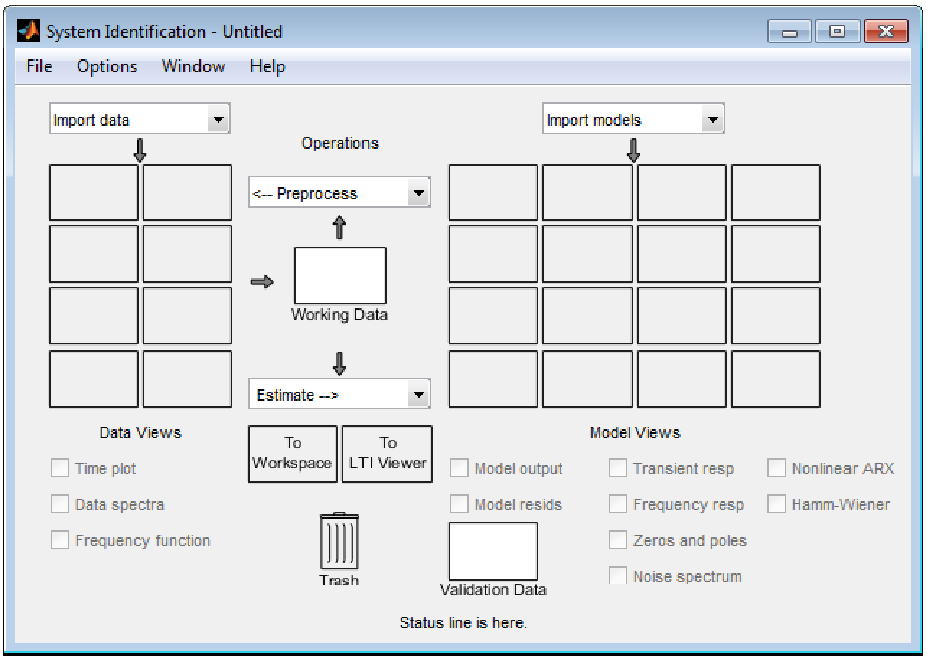

***Figure 36**. System identification toolbox GUI*

The similarity of the estimated model and measured data is calculated in percentage using the following formula [71]:

$$fit = \left(1 - \frac{\|y - \hat{y}\|}{\|y - mean(y)\|}\right)100\% \tag{2.21}$$

where y is the measured data output and $\hat{y}$ is the estimated data output of the system. Another method to check the goodness of fit is VAF which is called as variance accounted for [72]. This method compares the variation of the variance between input and output signal. In this work, VAF is only used to compare the time domain data of the system. VAF is computed as:

$$VAF = \left(1 - \frac{\text{var}(y - y_m)}{\text{var}(y)}\right)100\% \tag{2.22}$$

The parameters to be estimated are given in equation (2.19). The software uses the least square error method to find the parameters of the model. In Figure 37, the

measured output of the system and the fitted curves to these signals in frequency domain can be seen for some fitting results and in Figure 38, all fitted data are drawn simultaneously whose fitted parameters are given in Table 2. According to the simulation results in Figure 37, the system can be well-defined as a second order linear system with one free integrator. This means that the mathematical model of the system is enough to define the system itself.

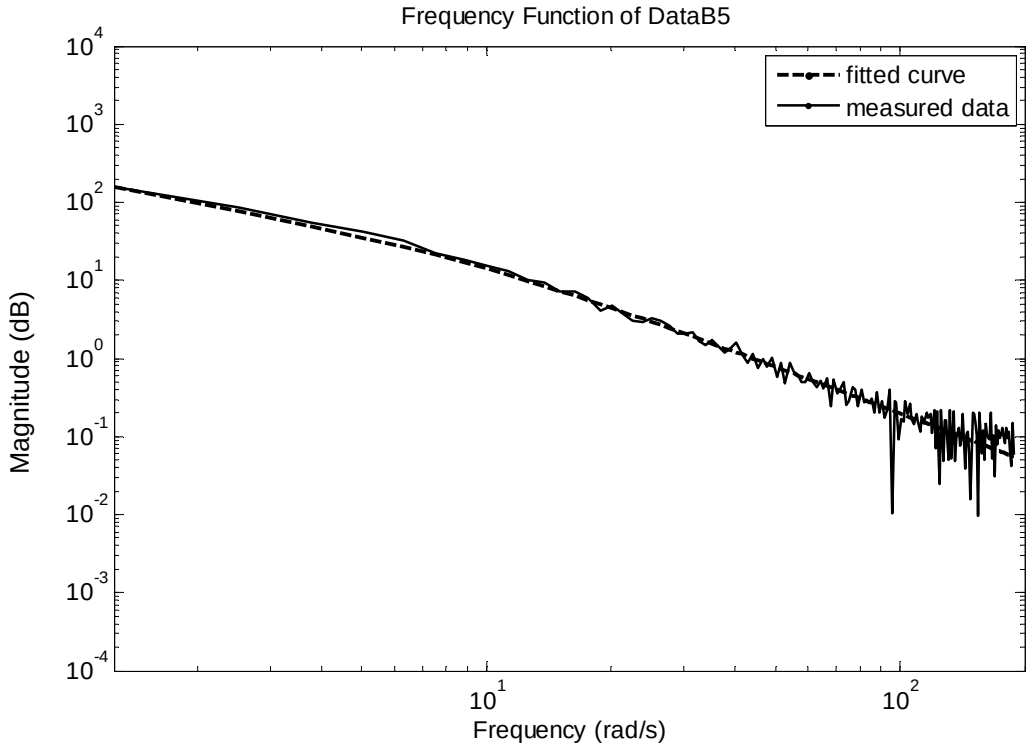

Figure 37. *Comparison of estimation results with outputs*

Table 2. *Process model parameter estimation and percentage of the fittings*

Data Set Name	Parameters	Similarity (%)
DataB1_1	Kp=210.4 Tp1=0.10775	89.86
DataB3_1	Kp=210 Tp1=0.10	90.08
DataB5	Kp=218.5 Tp1=0.1034	88.45
DataB6_1	Kp=219.58 Tp1=0.1017	88.14
DataB7_1	Kp=219 Tp1=0.103	88.17
DataB9	Kp=222.5 Tp1=0.10085	87.22
DataB10	Kp=220.22 Tp1=0.09978	87.92
DataB3_2	Kp=204.15 Tp1=0.15	83.81
DataB4	Kp=218.71 Tp1=0.10	88.36
DataB2	Kp=218.22 Tp1=0.090148	87.98
DataB3	Kp=220 Tp1=0.1	87.99
DataP1	Kp=210 Tp1=0.10	90.08
DataP2	Kp=242.51 Tp1=0.10	79.24
DataP3	Kp=230 Tp1=0.15	81.46
DataP4_1	Kp=180 Tp1=0.099	84.27
DataP5	Kp=210 Tp1=0.10711	89.93
DataP6	Kp=229.19 Tp1=0.099	84.46
DataP7	Kp=237.6 Tp1=0.12579	81.27
DataP8	Kp=205.12 Tp1=0.10986	89.87
DataP13	Kp=201.47 Tp1=0.10476	90.01
DataP10_1	Kp=205.12 Tp1=0.10483	90.24
DataP9	Kp=205.12 Tp1=0.10536	90.21

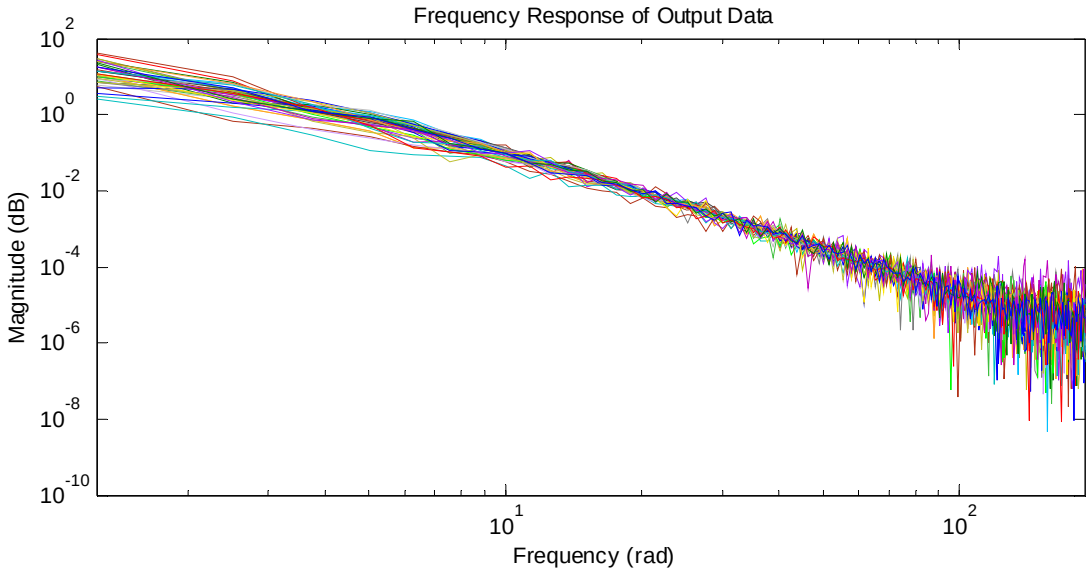

Figure 38. *Frequency response of experimental outputs*

Note that in Figure 38, all the outputs behave in nearly same manner, which means that collected data are consistent to each other. The Bode plot of obtained plant models is given in Figure 39.

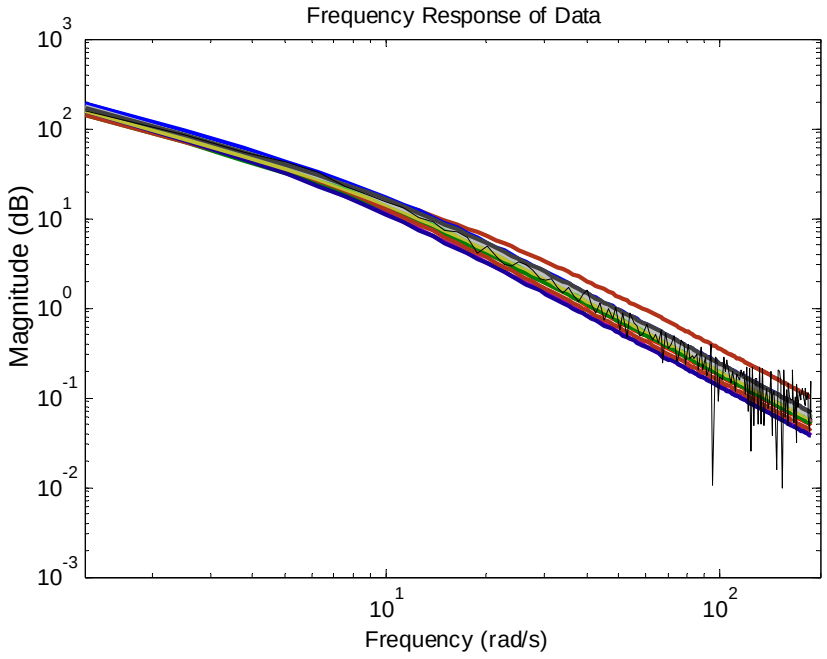

Figure 39. *Fitted transfer functions*

As mentioned before, these analyses can also be done in time domain but time domain analysis has some disadvantages. One of them is that, time domain identification procedure depends on initial conditions which means that outputs of the system may differ although same input signal is applied to the system several times. Therefore, the fitted data could not be reliable enough to use. In order to obtain satisfactory results in time domain, analysis should be done a bit longer in time and the some initial parts of the data can be thrown away for the analysis. If the simulated data has trend or is parallel to the measured data, VAF is used to show the similarity of the simulated data. In this thesis, some of data are also analyzed in time domain. By this way, the frequency response fitted data are double-checked. From Figure 40 to 42, results of the time domain analysis can be seen for some input signals mentioned in Table 2.

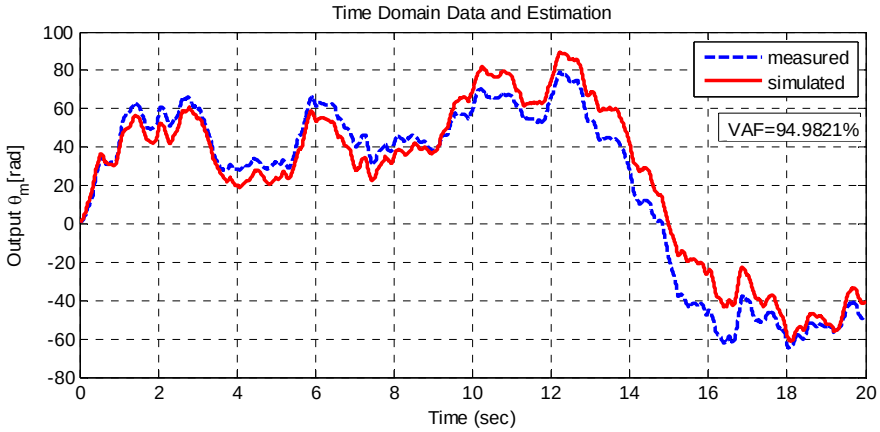

***Figure 40**. Output of the DataB2*

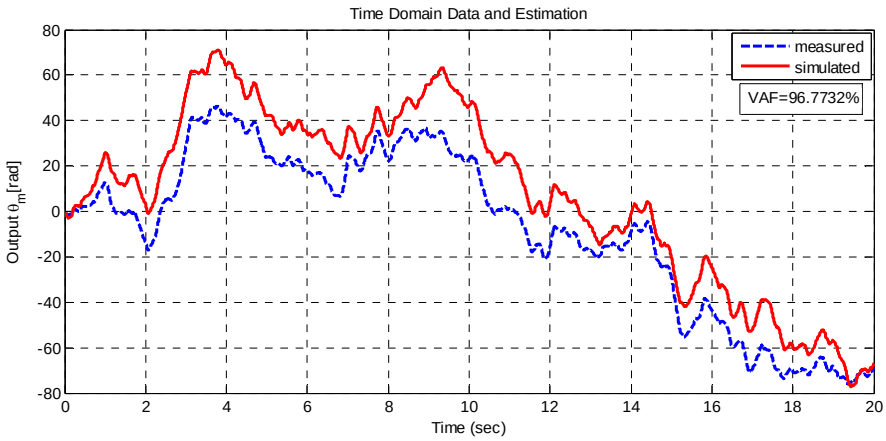

***Figure 41.** Output of the DataP3*

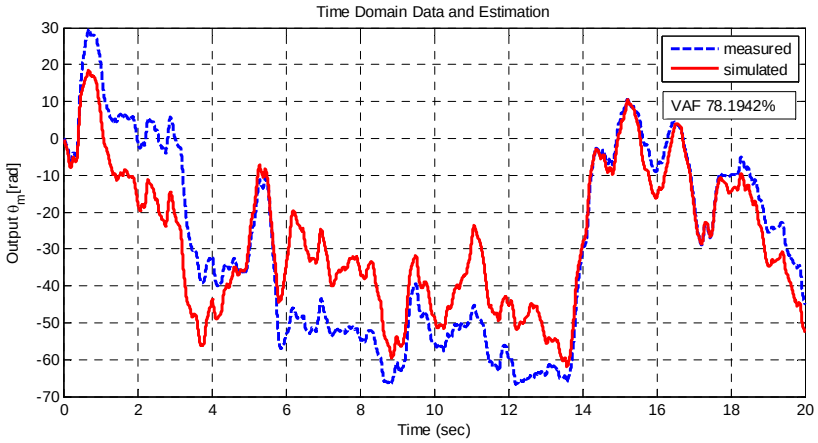

***Figure 42**. Output of the DataB4*

As can be understood from the time domain analysis, the plant is well estimated. Although one of the VAF rates are low, the fitted and measured data trend resemble each other. Then, for the controller design, the following plant is used thereafter.

$$G_p = \frac{210}{s(0.1s+1)} \tag{2.23}$$

If the equation (2.15) is used for the system identification procedure with the known K_t and J_{eq} values, the following B_{eq} values are found.

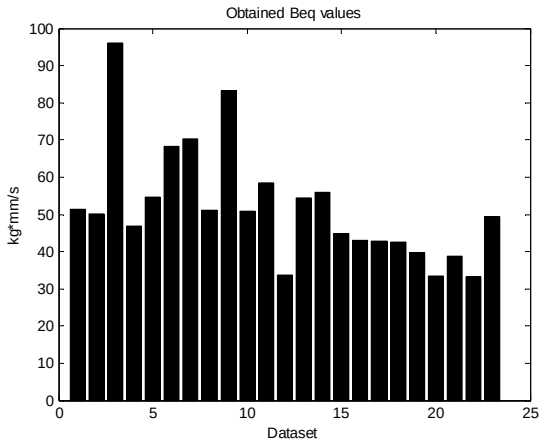

***Figure 43.** Obtained B_{eq} values*

The nominal model of the plant can also be written as

$$G_p = \frac{10000}{s(5.65s+49.737)} \tag{2.24}$$

CHAPTER 3

CONTROLLER DESIGN

3.1 Requirements for the Closed Loop System

In any closed loop system, the basic requirements to be met are:

- The minimum requirement should be defined to make the closed loop stable.
- The controlled variable should track the command input well enough. (both precise and fast).
- Disturbance rejection should be good enough.
- Finally, the closed loop system should be robust enough to deal with the changes of system parameters in predefined degree.

As explained in previous chapters, robust control helps engineer to make such a design especially for unknown plant variation. In this system, plant parameters have uncertainties. Sensor noise and aerodynamic loads are the external source of disturbances while modeling errors and environmental conditions on the plant are the source of plant uncertainties. Apart from these, the system itself shows nonlinear behavior. These can be grouped as saturation limit on the physical system, limited current capacity and cogging torque of actuator. As mentioned earlier, the fin deflection angle is limited to $\delta = \pm 25^{\circ}$. As might be expected, the current source is not unlimited. The power budget of the system limits the current and for the system in this thesis, current limit value cannot be higher than $\pm 30\ A$. The current limit can cause saturation on the control signal. In addition to this, the cogging torque is another source of disturbance. This torque always opposes to the motion of the system. On the other hand, the angular speed of the fin is also limited.

The maximum angular speed of the system can be $\left|\dot{\theta}_{fin}\right| \leq 200\,\text{deg/s}$. All these limitations and disturbances sources are taken into account while designing a controller. In Table 3 below, the minimum performance requirements of the closed loop system are given.

Table 3. *Minimum performance requirements of the system*

Settling Time	$\leq 0.100s$
Maximum Percent over shoot	$\leq 6\%$
Bandwidth for $\pm 1^{\circ}$ amplitude signal	$\geq 10\ Hz$
Steady state error	$\leq 0.1^{\circ}$

3.2 PID Controller Synthesis

PID (proportional, integral and derivative) control action is one of the most widely used feedback control schemes. In many industrial, engineering and science applications, PID controllers are preferred because of its simple design and ease of implementation. In addition to these, PID controllers are cost effective. Although they are not the optimum controller, they provide adequate performance in most cases.

PID controller is composed of three parts which are proportional, integral and derivative parts. The proportional part drives the out in proportion to the instantaneous error while integral part drives the out in proportion to the accumulated error. And finally, derivative action drives the output in proportion to the rate of change of error [73].

Transfer function of PID controller is given as

$$K(s) = K_p + \frac{K_i}{s} + K_d s \tag{3.1}$$

In Figure 44, the closed loop block diagram of fin actuation system for the reference input δ_r, hinge moment input T_f and the output fin angle θ_f can be seen. Then, the closed loop transfer function of the FAS block diagram is written as

$$\frac{\theta_f}{\delta_r} = \frac{(K_d s^2 + K_p s + K_i +) \Big/ K_i}{\frac{T}{K_i K} s^3 + \frac{(1+K_d)}{K_i} s^2 + \frac{K_p}{K_i} s^2 + 1} \tag{3.2}$$

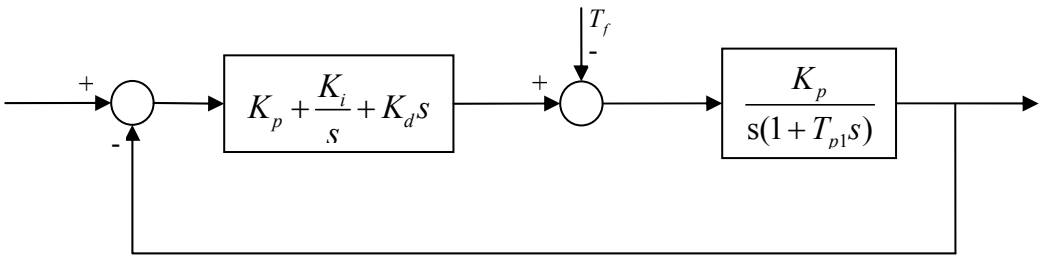

Figure 44. *Fin actuation system block diagram for PID controller*

After obtaining the closed loop transfer function, the weights of the PID controller can be found to obtain the optimal performance meeting the system requirements. This is called tuning. In literature, there are many methods developed in order to obtain the weights of the PID [74]. One of the methods is Butterworth and Chebyshev polynomials. The characteristic equation of the system is a third-order polynomial therefore in this work a third-order Butterworth polynomial could be chosen for controller design [75].

$$B_3(\mathrm{s}) = \frac{s^3}{\omega_c^3} + \frac{2s^2}{\omega_c^2} + \frac{2s}{\omega_c} + 1 \tag{3.3}$$

where ω_c is the desired bandwidth of the system. After matching the denominators of equations (3.2) and (3.3) term by term, weights of the controller can be found as

$$\begin{aligned} K_p &= \frac{2T_{p1}\omega_c^2}{K} \\ K_i &= \frac{T_{p1}\omega_c^3}{K} \\ K_d &= \frac{2T_{p1}\omega_c - 1}{K} \end{aligned} \tag{3.4}$$

To be able to apply the controller to the system in real application, the obtained PID controller must be discretized. The general PID control action can also be shown as

$$u(t) = K\left[e(t) + \frac{1}{T_i}\int_0^t e(t)dt + T_d \frac{de(t)}{dt} \right] \tag{3.5}$$

where $e(t)$ is the input to the controller and $u(t)$ is the output of the controller. Discretizing the equation (3.5) by approximating the integral term by the trapezoidal summation and the derivative term by two point differences, the following equality is obtained.

$$u(kT_s) = K\left\{ e(kT_s) + \frac{T_s}{T_i}\sum_{h=1}^{k} \frac{e((h-1)T_s) + e(hT_s)}{2} + \frac{T_d}{T_s}\left[e(kT_s) - e((k-1)T_s) \right] \right\} \tag{3.6}$$

and define

$$\sum_{h=1}^{k} \frac{e((h-1)T_s) + e(hT_s)}{2} = \sum_{h=1}^{k} f(hT_s), \quad f(0) = 0 \tag{3.7}$$

Taking the z transform of the equation (3.7)

$$\begin{aligned} Z\left[\sum_{h=1}^{k} \frac{e((h-1)T_s) + e(hT_s)}{2} \right] = Z\left[\sum_{h=1}^{k} f(hT_s) \right] &= \frac{1}{1-z^{-1}}\left[F(z) - f(0) \right] \\ &= \frac{1}{1-z^{-1}} F(z) \end{aligned} \tag{3.8}$$

where $F(z)$ is

$$F(z) = Z\left[f(hT_s) \right] = \frac{1+z^{-1}}{2} E(z) \tag{3.9}$$

Then, the equation(3.6) is written as

$$U(z) = K\left[1 + \frac{T_s}{2T_i}\frac{1+z^{-1}}{1-z^{-1}} + \frac{T_d}{T_s}\left(1 - z^{-1}\right) \right] E(z) \tag{3.10}$$

The block diagram of the discrete PID controller is given in Figure 45.

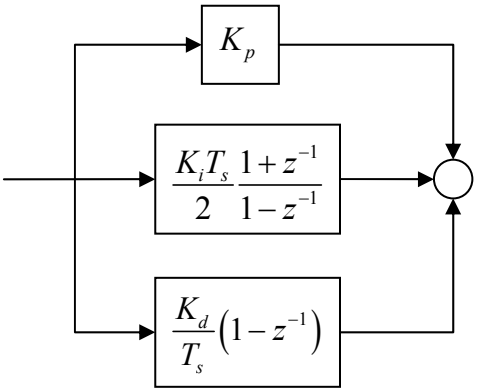

***Figure 45**. Discrete time PID controller*

In practice, PID controllers are not used with pure derivative actions because when it is used, it produces a derivative kick in the control signal for step inputs [33]. This situation causes undesirable noise amplification; so that PID controller's are cascaded by a first order low pass filter. The representation of the PID controller is given in equation (3.11). This alternative controller is designed using *'pidtool'* command.

$$PID_f = K_p + \frac{K_i}{s} + \frac{K_d s}{T_f s + 1} \tag{3.11}$$

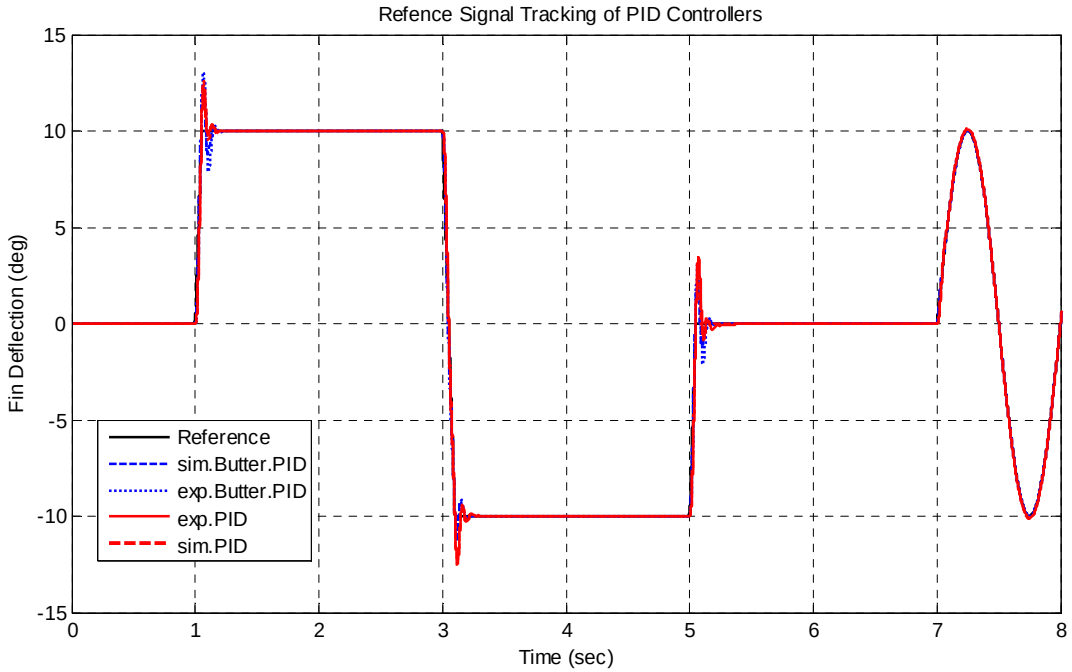

***Figure 46.** Reference signal tracking of the PID controllers*

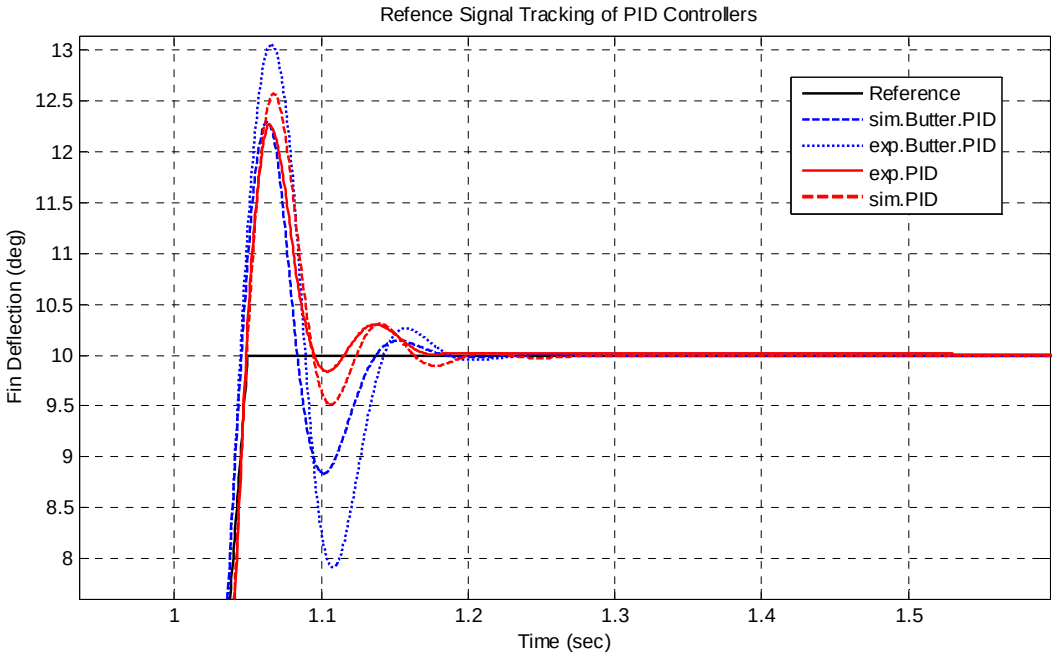

Figure 47. *Magnification of step response at t=1s in Figure 46*

The block diagram used in simulation is given at Figure 49.

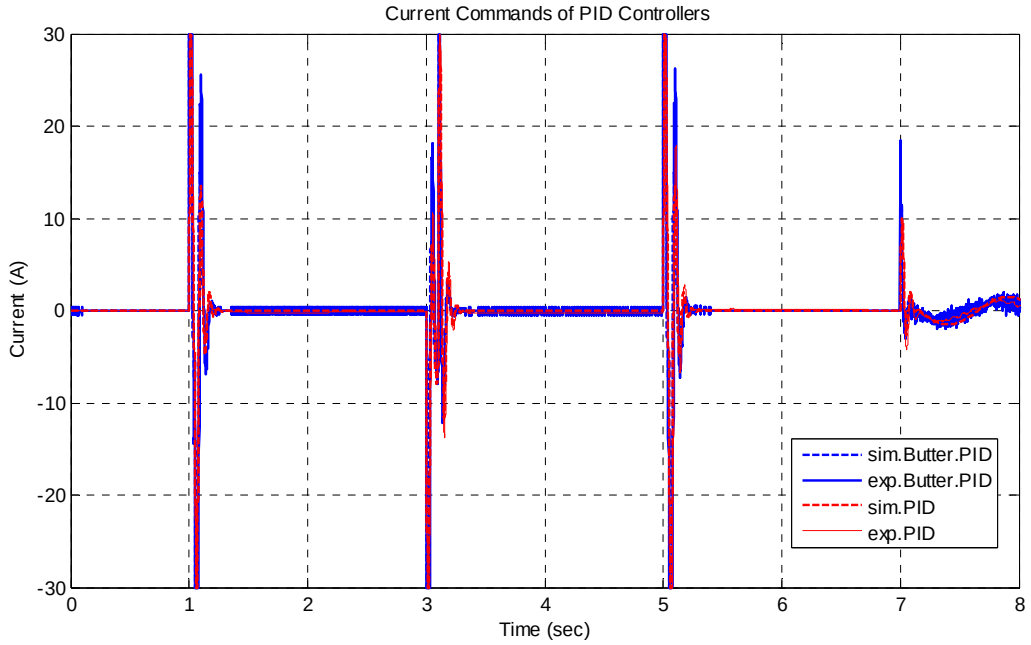

Figure 48. *Current commands of PID controllers*

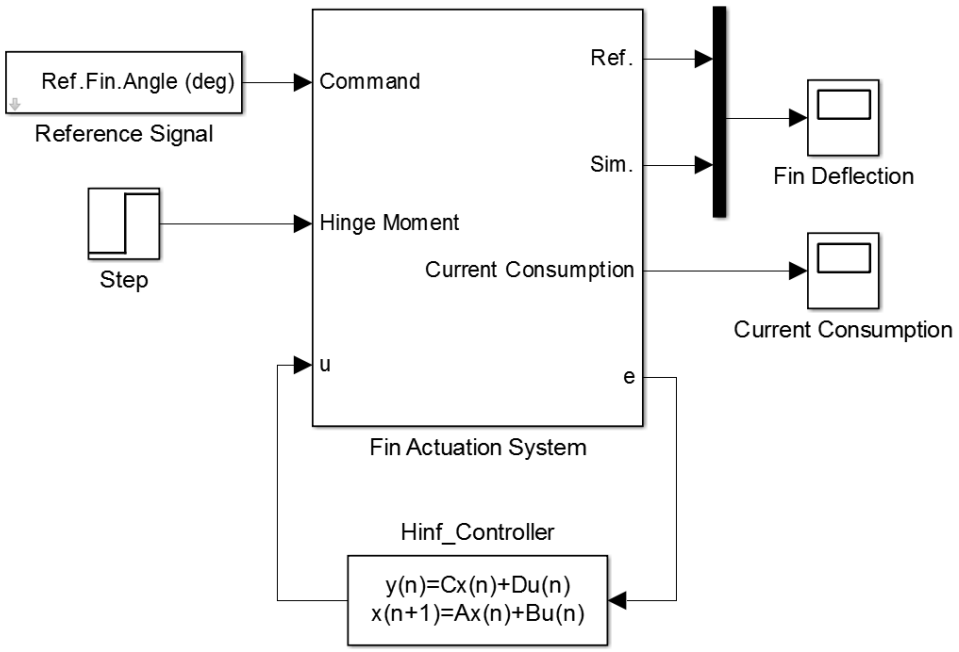

Figure 49. *The main block diagram used in simulations*

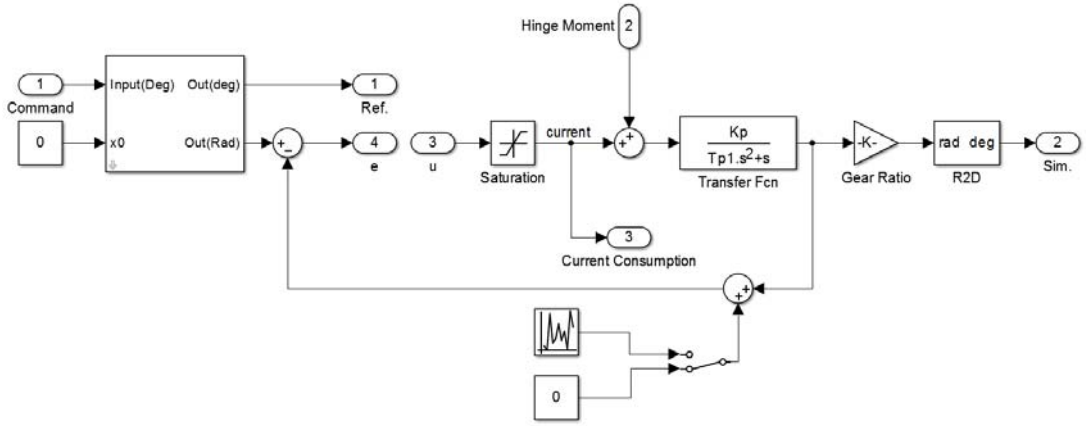

Figure 50. *Subsystem of the main block diagram*

Another alternative tuning method for PID controller is well known empirical Ziegler-Nichols method. Although this method originally is used for process control application, it can also be applied to servo control systems. In Ziegler-Nichols tuning method, plant is resembled to the first order system with a transport lag which is called as first order plus dead time (FOPDT) model. The model is expressed as

$$G(s) = \frac{k}{1+sT} e^{-sL} \tag{3.12}$$

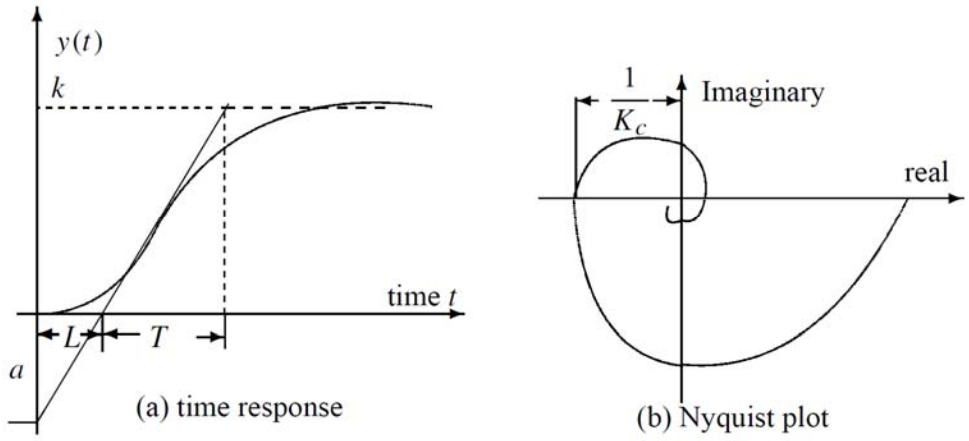

***Figure 51**. Response of the FOPDT model [33]*

There are two methods to find the parameters of the PID controller. The first one is based on the response of the plant to the step input. Ziegler Nichols tuning rule that based on the step response is given in Table 4.

***Table 4.** Ziegler Nichols tuning formula based on step response*

Controller Type	K_p	T_i	T_d
P	1/a	-	-
PI	0.9/a	3L	-
PID	1.2/a	2L	0.5L

where $a = \frac{kL}{T}$

If frequency response experiment is performed, the following tuning formula which is given in Table 5 is used. ω_c is called the crossover frequency and K_c is called ultimate gain. These parameters can be obtained using Nyquist plot as shown in Figure 51.

Table 5. *Ziegler Nichols tuning formula based on frequency response*

Controller Type	K_p	T_i	T_d
P	$0.5K_c$	-	-
PI	$0.4K_c$	$0.8T_c$	-
PID	$0.6K_c$	$0.5T_c$	$0.125T_c$

where $T_c = \dfrac{2\pi}{\omega_c}$

For this system, Z-N tuning procedure can be applied as given below.

- Set K_i and K_d value to zero. Excite the system with step input.
- Increase the proportional gain until system begins to oscillate. When oscillation begins, record the K_p and oscillation frequency value f_0 .

In this application, Z-N PID could not give the desired results. However, for this type of work, it is very useful for obtaining data or making closed loop identification whereas it is not possible to adjust the system bandwidth in Z-N PID. In Figure 52, the step response of the system is given. As stated above, the system is excited until it starts to oscillations. At that time, the K_p is found as 0.12 and frequency of the oscillation can be determined as $f_0 = 2.3872$.

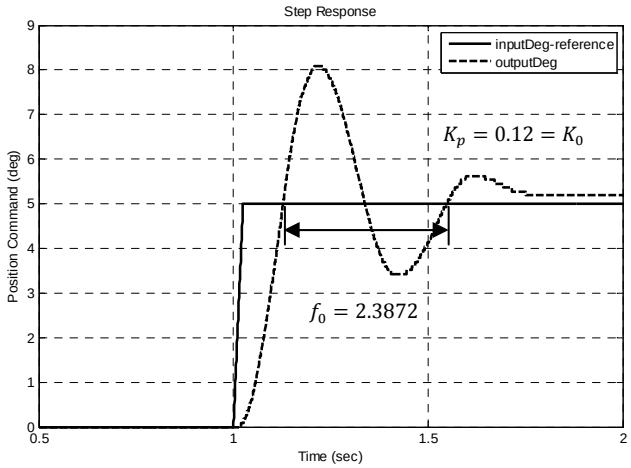

Figure 52. *Step response of the system to determine K_p*

Then using these values, Z-N PID controller parameters can be determined using Table 5 as

$$K_p = 0.6K_o = 0.072\,,\ K_i = 2f_oK_p = 0.3438 \text{ and } K_d = \frac{K_p}{8f_o} = 0.0038$$

The step response of the Z-N PID tuned system is given in Figure 53. As expected, the system is very slow and the desired performance could not be obtained.

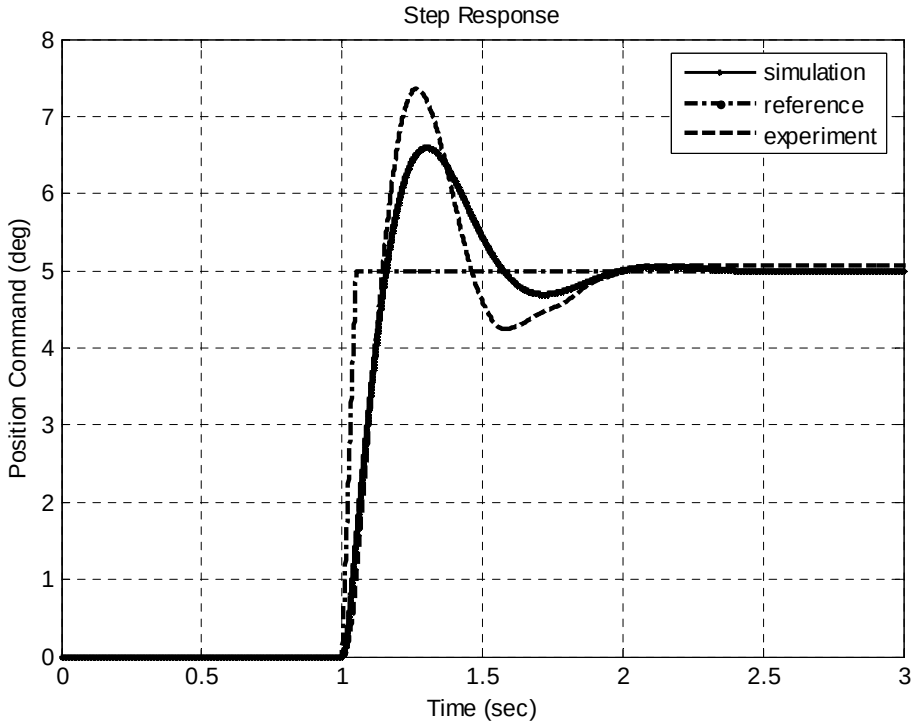

Figure 53. *Step response comparison of Z-N Tuned PID*

As can be seen from Figure 53, Z-N tuned PID controller has some difficulty to follow the command. The dry friction on the system also affects the system performance which results in undesired behavior.

3.3 Synthesis of Robust Controllers

In this section, the synthesis of robust controllers will be discussed. As known, disturbances and uncertainties cause the performance of the classical controllers to decrease. In robust control design methodology, it is possible to add the uncertainties to the controller design process which is a very important advantage over classical controllers. In general, the obtained robust controllers have higher orders. Especially,

apart from the plant, the weighting functions selection affects the order of controller; therefore, in order to keep the controller order lower, first order weighing functions are generally chosen. If the obtained controller order is too high for computational cost, it is possible to decrease the order of controller using some order-reducing algorithms; however, the powerful calculation tools, high speed microprocessor currently make it easy to develop such controllers.

The aim of the robust controller design is same as in classical controllers; however the main difference is that the robust controllers maintain the stability and performance under the pre-specified uncertainties and disturbances. In this thesis, the proper system model and the desired controller are obtained using MATLAB® "*hinfsyn*" command.

The block diagrams for the controller synthesis and the input-output signals to the system are given in Figure 54-57. The parameters defining uncertainties, disturbances, weighting and cost functions are defined as follows:

W_{ref} : Weighting function for reference signal

W_{hinge} : Weighting function for external aerodynamic loads

W_{u} : Cost function for controller output

W_{ideal} : Ideal closed loop system

W_{perf} : Cost function for performance index

W_{noise} : Weighting function for sensor noise

W_{m} : Model uncertainty function

N : Transmission ratio for mechanism

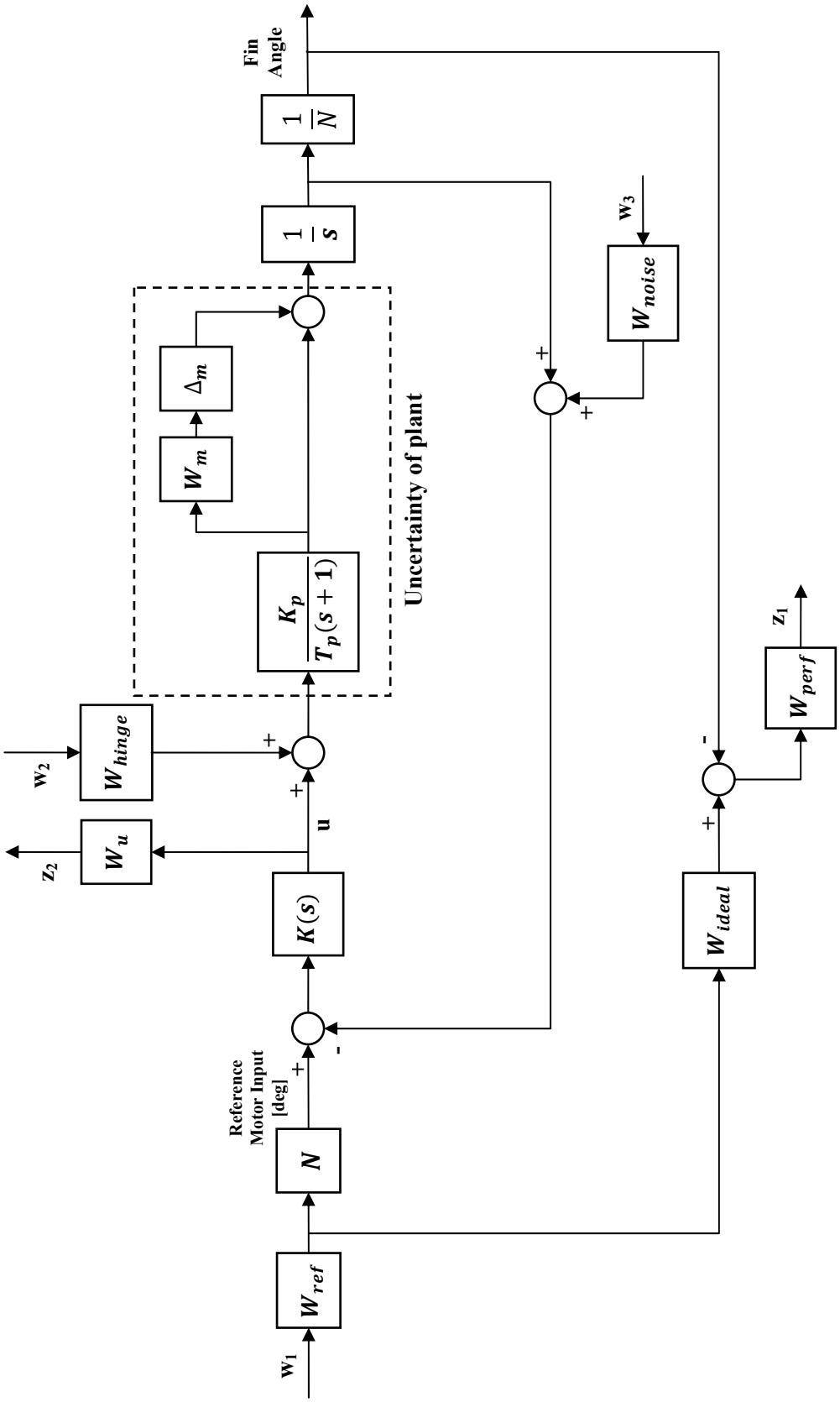

Figure 54. *Block diagram for H_∞ robust controller*

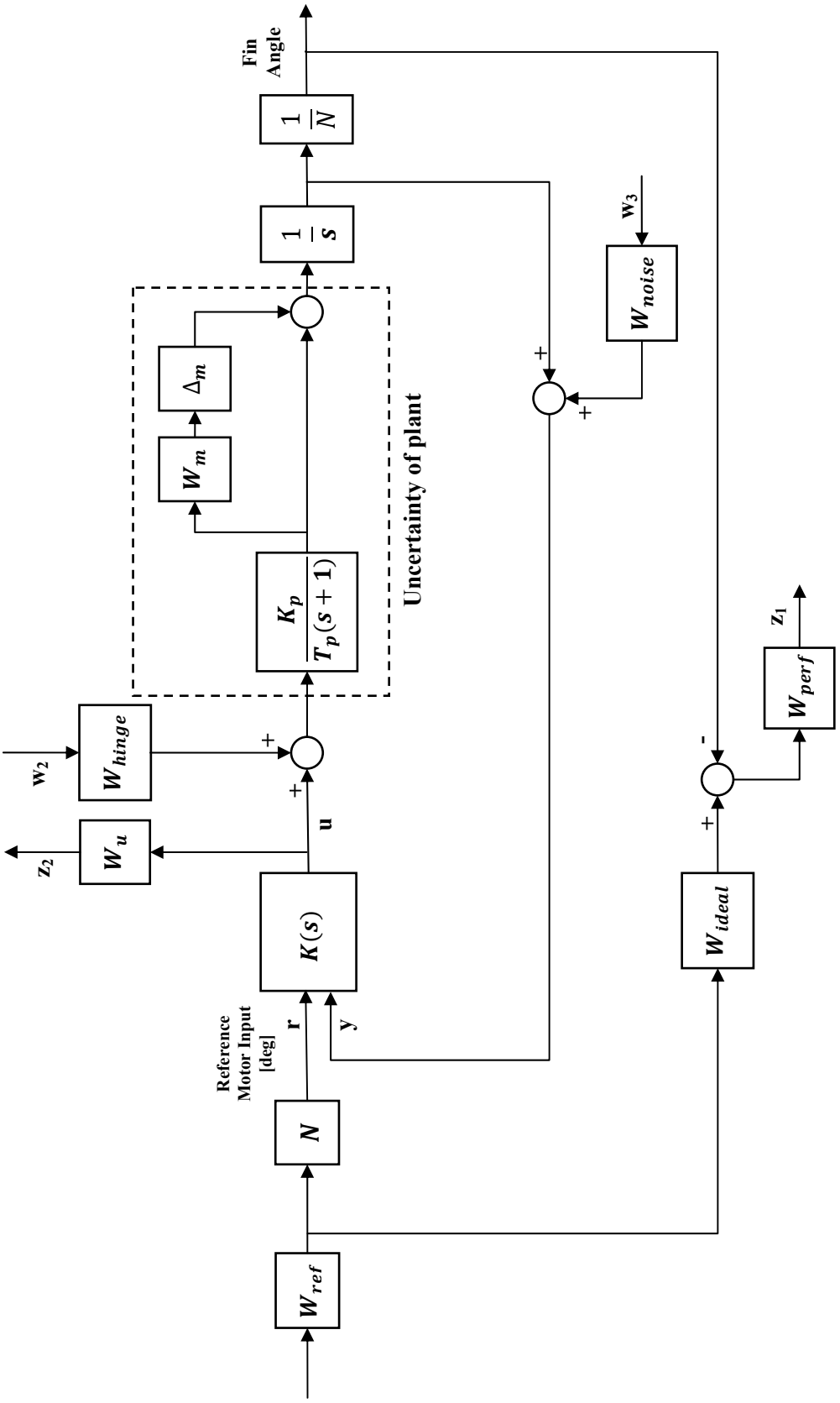

Figure 55. *Block diagram for 2-DOF H_∞ robust controller*

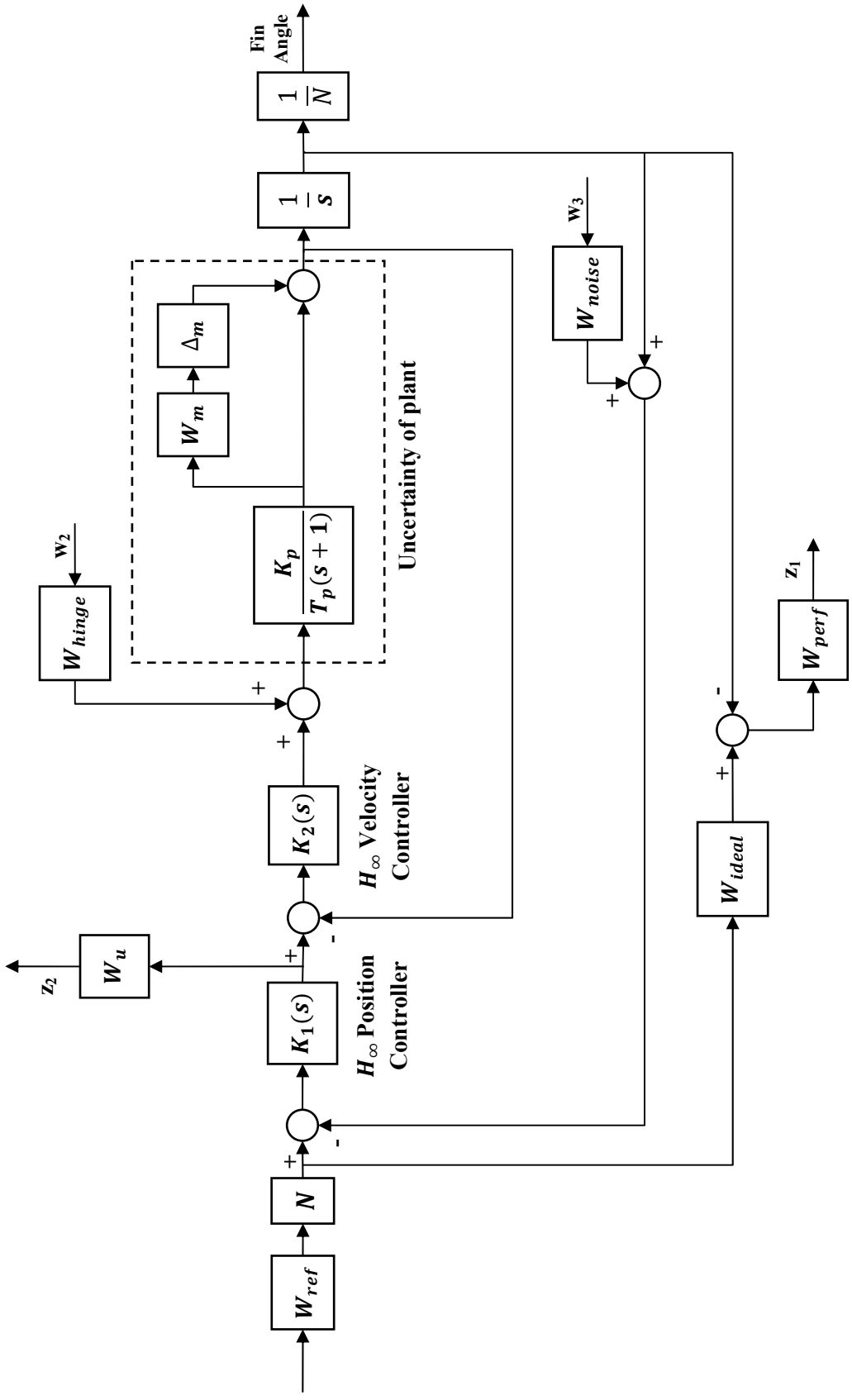

Figure 56. *Block diagram for cascade H_∞ robust controller*

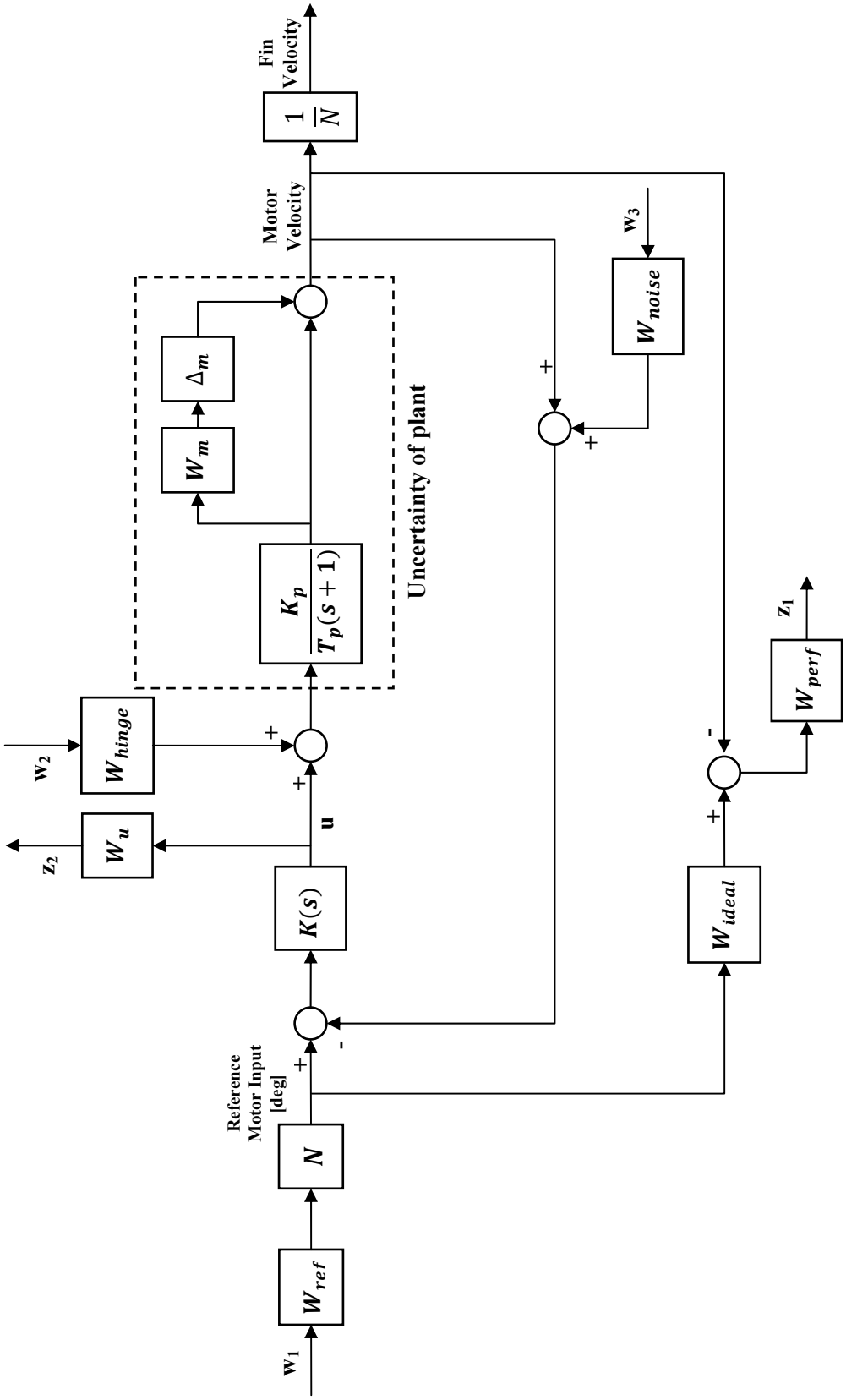

Figure 57. *Block diagram for inner loop H_∞ speed robust controller*

According to these diagrams, the generalized plant model of the system can be illustrated as in Figure 58.

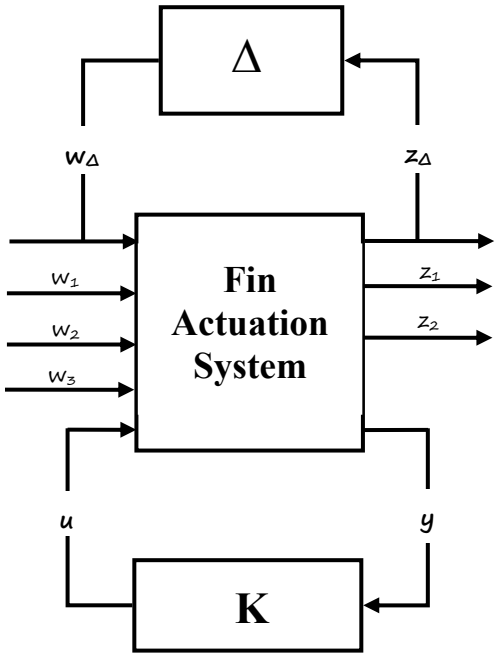

Figure 58. *Generalized plant for controller synthesis*

The main idea of H_∞ controller is to find the stable $\min K(s) = \|T_{zw}\|_\infty$ where $T_{zw} = LFT(P,K)$ is defined in previous chapter. The more detailed representation of T_{zw} is

$$\underbrace{\begin{bmatrix} z_\Delta \\ z_p \end{bmatrix}}_{z} = P * K \underbrace{\begin{bmatrix} w_\Delta \\ w_p \end{bmatrix}}_{w} \quad \text{and} \quad P * K = LFT(P,K) = T_{zw} \tag{3.13}$$

H_∞ controller minimizes the transfer function infinity norm from input w to the out z; thus infinity norm of T_{zw} 'γ' is kept under the unity.

3.3.1 Selection of Weighting Functions

The selection of weighting functions is one of the most important parts of the robust control design since closed loop system properties including desired performance characteristics, limits of the system, uncertainties and disturbances are defined by means of these functions. The obtained controller is directly connected to the

weighting functions. Although there is not a straight forward way of defining weighting functions, there are some methods in the literature [38], [41], [76], [77], [78], and [79] based on experiments and past experience. As mentioned before, the selection of weighting functions shapes the frequency and time response of the system; thus these functions should be selected such that the desired closed loop system are stable and minimum performance characteristics are obtained. In order to achieve the desired performance and robustness, one should consider the previously mentioned sensitivity and complementary functions and their effects on system as given in Figure 59.

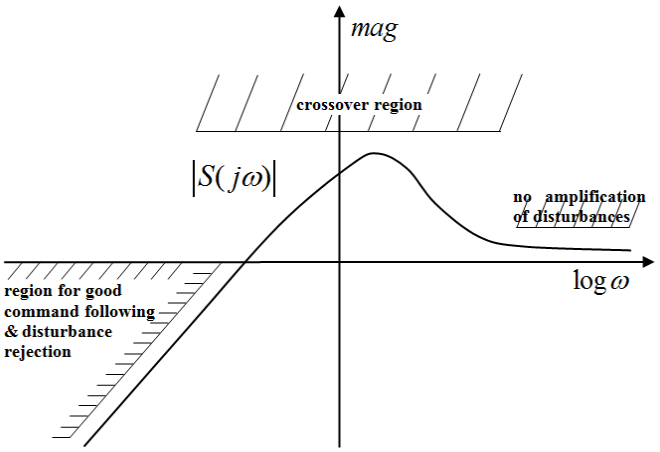

Figure 59. *Typical sensitivity function [38]*

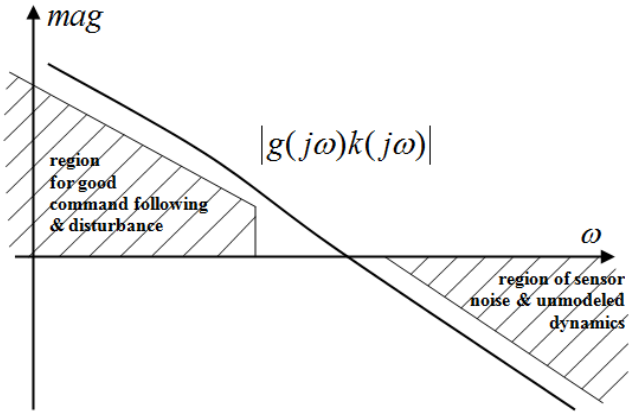

Figure 60. *Typical complementary function [38]*

In order to obtain the desired performance, the weighting function should be selected such that the following statement must be ensured.

$$\left\| w_g X \right\|_\infty < 1,\ X(j\omega) < \frac{1}{\left| w_g(j\omega) \right|},\ \forall \omega \tag{3.14}$$

The selected weighting functions must cover the sensitivity function to satisfy the performance and disturbance requirements. In Figure 61, the possible choice of performance weight function is illustrated.

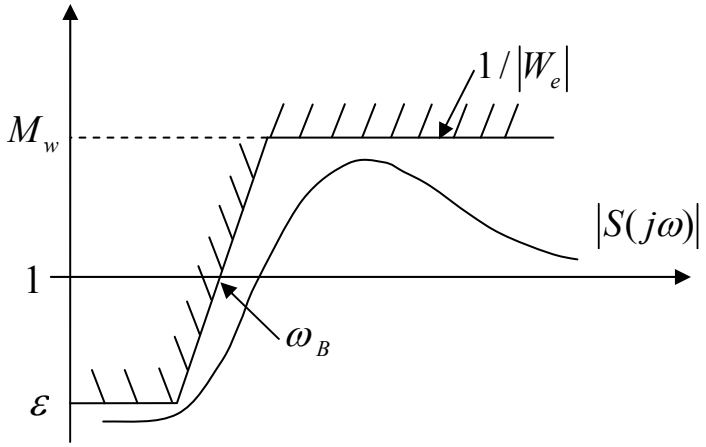

Figure 61. *Performance weight function*

In this figure, M_w describes the peak sensitivity, ω_B is bandwidth of the system and ε is the steady state error. When the mentioned parameters are defined, the following equation (3.15) and (3.16) can be used to determine the weighting function. At this point, recall that, the given function is not an absolute solution but a only the starting point. During experiments, the weighting functions are redefined and rearranged.

$$w_g = \frac{s/M_w + \omega_B}{s} \tag{3.15}$$

$$w_g = \frac{s/M_w + \omega_B}{s + \omega_B \varepsilon} \tag{3.16}$$

If steeper transition is needed between the low and high frequency region, the following formula can then be used to define weighting functions.

$$w_g = \left(\frac{s / \sqrt[k]{M_w} + \omega_B}{s + \omega_B \sqrt[k]{\varepsilon}} \right)^k \tag{3.17}$$

For the controller output, the magnitude of $|KS(j\omega)|$ in the low frequency region should be penalized according to the controller cost effort and saturation limits. In Figure 62, M_u describes the maximum gain and it is generally large. This gain is limited by the controller bandwidth ω_{BC}. Then the candidate weight functions are written as

$$w = \frac{s + \omega_{BC} / M_u}{\omega_{BC}} \tag{3.18}$$

$$w = \frac{s + \omega_{BC} / M_u}{\varepsilon_1 s + \omega_{BC}} \tag{3.19}$$

One would need faster roll-off in order to attenuate the high-frequency noises as fast as possible, and then the following weighting function may also be selected.

$$w = \left(\frac{s + \omega_{BC} / \sqrt[k]{M_u}}{\sqrt[k]{\varepsilon_1} s + \omega_{BC}} \right)^k \tag{3.20}$$

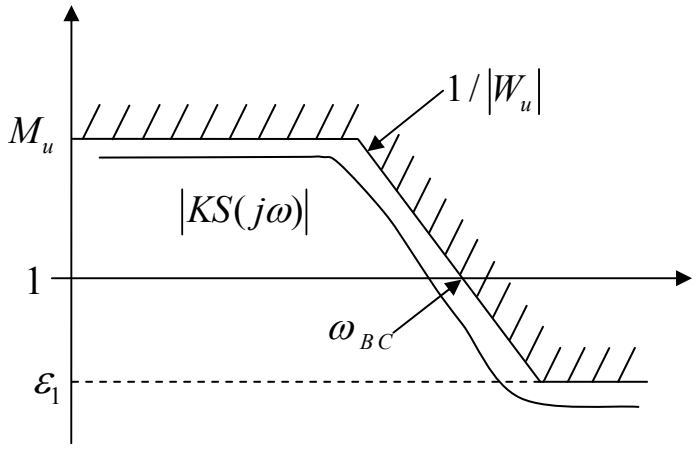

Figure 62. *Control signal weight function*

3.3.1.1 Model Uncertainty

In previous section, control actuation system was modeled as a second order system with a free integrator. When the obtained data are examined, it can be understood that parameters of the system change in some interval. The Bode plot of the system with uncertainties which is modeled as in equation (2.19) is given in Figure 63.

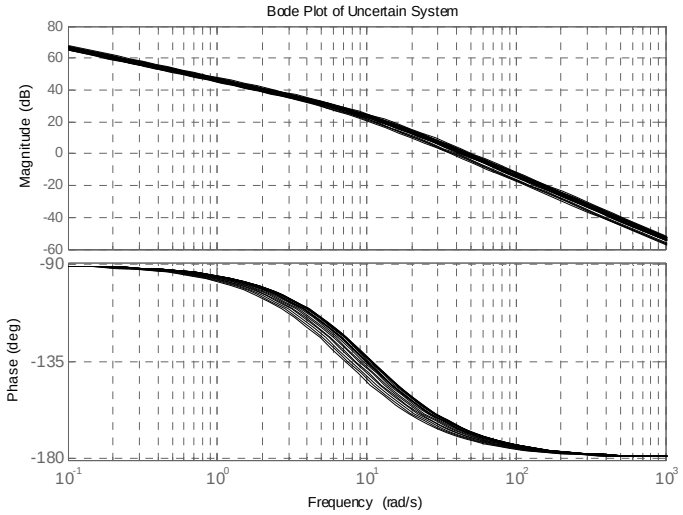

Figure 63. *Bode plot of uncertain system*

As mentioned before, the system was also identified using the known parameters K_t and J_{eq}. Using the equation (2.15), the Bode plot of this system is shown in Figure 64.

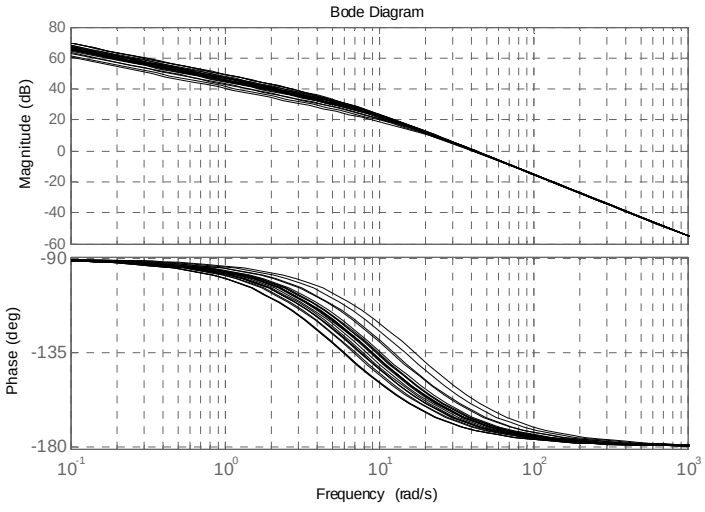

Figure 64. *Bode plot of uncertain system with known* K_t *and* J_{eq}

Variable environmental and working conditions cause these uncertainties on the system. In this system, uncertainty can be defined in two ways. The first one is taking the system parameters term by term and specifying the multiplicative uncertainties as shown in Figure 65.

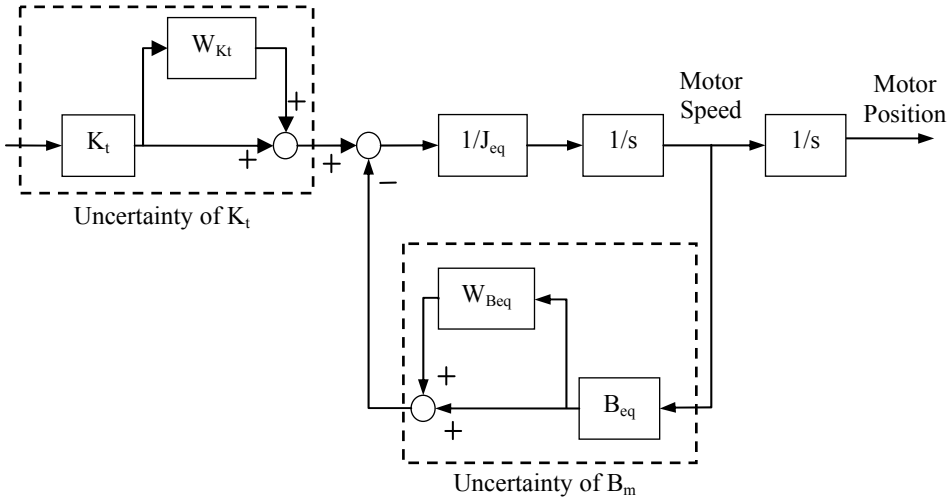

Figure 65. *Representation of plant uncertainties term by term*

The second one is that the uncertainty of the system is defined as a whole system as shown in Figure 66. In this thesis, this method is preferred while designing robust controller.

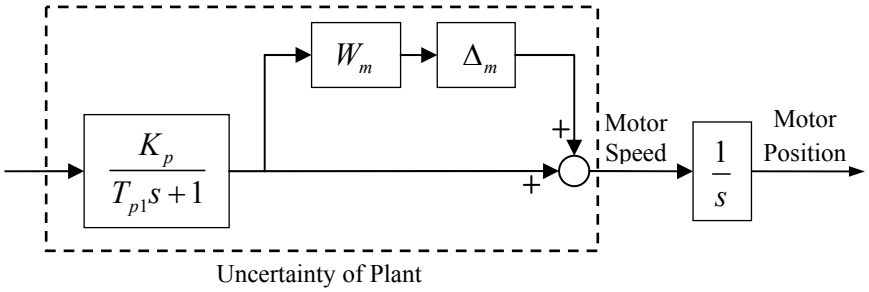

Figure 66. *Representation of whole plant uncertainty*

In this system, there is no difference in defining the uncertainty in the position level or velocity level. Thus, free integrator can be separated from the model to obtain the transfer function in velocity level. Then, the model uncertainty is described as a first

order system as shown in Figure 66. Experimental results given in Table 2 show that the parameters of the system vary as given below.

$$\begin{aligned} 180 < K_p < 230 \\ 0.09 < T_{p1} < 0.15 \end{aligned} \tag{3.21}$$

The multiplicative uncertainty is defined as

$$G_p = G_n(s)[1 + W_m(s)\Delta_m(s)] \tag{3.22}$$

where $|\Delta_m(j\omega)| \leq 1$. The relative error is also defined as using the following relation

$$\frac{|G(\mathrm{j}\omega) - G_n(\mathrm{j}\omega)|}{|G_n(\mathrm{j}\omega)|} \leq |W_m(\mathrm{j}\omega)|, \ \forall \omega \tag{3.23}$$

Using relations from equations (3.21) to (3.23), uncertainty of the model could be approximated as if it would include all uncertain plant models as shown in Figure 67. Then, the weighting function is given in equation (3.24)

$$W_m = \frac{0.4323s + 0.9574}{s + 6.71} \tag{3.24}$$

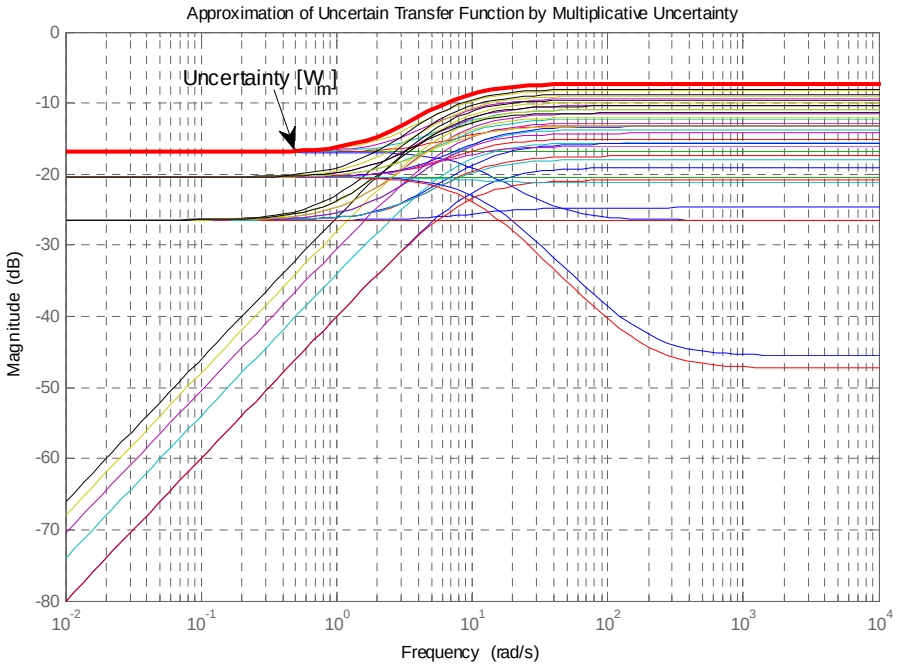

Figure 67. *Approximation of uncertain transfer function by multiplicative uncertainty*

3.3.1.2 Weighting Function for Reference Signal W_{ref}

Reference weighting function defines the desired input signal to the closed loop system. As mentioned before, the maximum fin angle is 25° at static condition (0 Hz) and $\delta_{ref} = 1^{\circ}$ at 20 Hz bandwidth is desired. Using this starting point, the weighting function can be approximated as

$$W_{ref} = \frac{0.01745}{0.3138s + 1} \tag{3.25}$$

The Bode amplitude plot of the weighting function of the reference signal to the closed loop system is given in Figure 68.

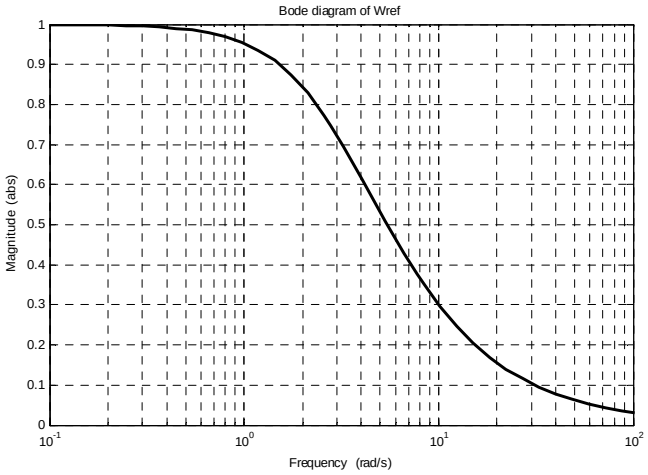

Figure 68. *Magnitude plot of the reference weight function,* W_{ref}

3.3.1.3 Weighting Function for Aerodynamic Loads W_{hinge}

Aerodynamic forces vary during the motion of missile. W_{hinge} is the weighting function that defines the estimated disturbance moment on the system during the motion. At the output of the weighting block, the disturbance signal is obtained. In this study, the maximum hinge moment that disturbs the system is 25 Nm. The desired weighting function is chosen as a low pass filter whose transfer function equation is given in (3.26) and its magnitude plot is drawn in Figure 69.

$$W_{hinge} = \frac{25}{0.3183s + 1} \tag{3.26}$$

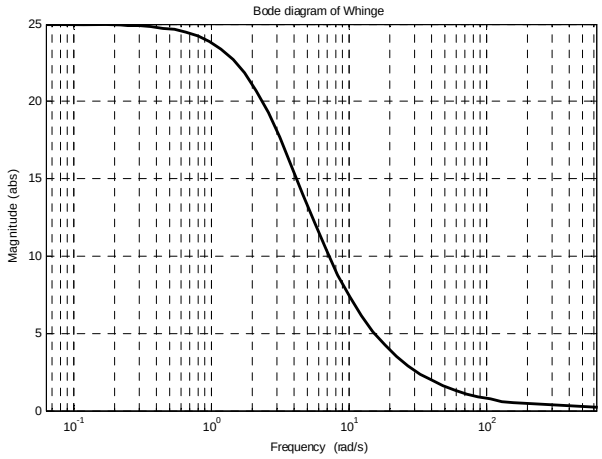

Figure 69. *Magnitude plot of the aerodynamic loads,* W_{hinge}

3.3.1.4 Cost Function for Controller Output W_u

Weighting function of the control output is used to define the limits of the actuator. This function helps to prevent the overconsumption of current; thus it is also called as penalty function. The maximum current to the system is 30 A and the corner frequency is 20 Hz. At high frequencies, the weighting is arranged such that minimum 1.5 A can be supplied to the system. Using this information, the weighting function can be written as in equation (3.27) and its amplitude plot is shown in Figure 70.

$$W_u = \frac{3.4s + 39.44}{s + 4092} \tag{3.27}$$

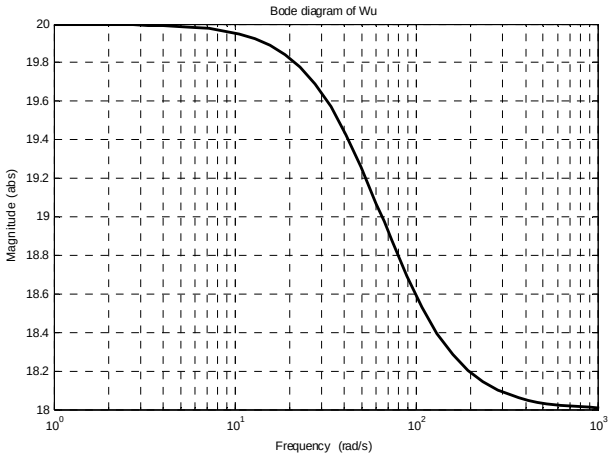

Figure 70. *Magnitude plot of the controller output loads,* $1/W_u$

3.3.1.5 Ideal Close Loop System, W_{ideal}

The desired closed loop behavior of the system can be defined using ideal system transfer function. Any model can be used here to define performance of the system. In this thesis, the model given in equation (3.28) is used to define the damping ratio and low frequency response of the closed loop system. In addition to this, the ideal system should satisfy the requirement of the closed loop system that is given in Table 3.

$$W_{ideal} = \frac{\omega_n^2}{s^2 + 2\xi\omega_n s + \omega_n^2} \tag{3.28}$$

where $\xi = 0.707$ and $\omega_n = 20\ Hz$.

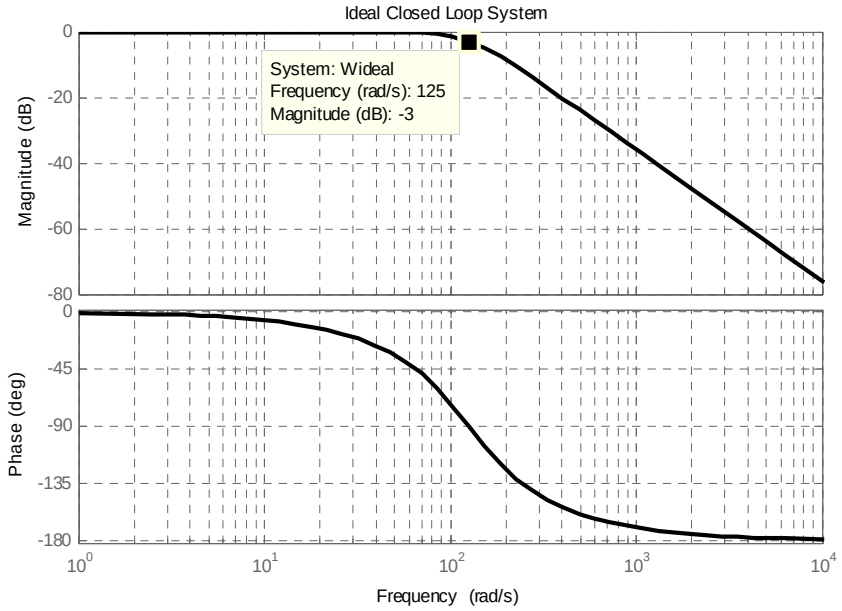

Figure 71. *Bode plot of the ideal closed loop system*

3.3.1.6 Cost Function for Performance Requirements, W_{perf}

As in controller output cost function, penalty function is again defined to guarantee that the error between the ideal system output and the obtained output fin angle in response to the same reference signal is small enough to meet the closed loop system requirements. The maximum error is chosen as 0.1° at minimum 20 Hz; therefore,

the penalty function is defined as high amplitude at low frequency and low amplitude at high frequency. The obtained penalty function can be represented as transfer function in equation (3.29) and its amplitude plot is given in Figure 72.

$$W_{perf} = \frac{0.28648s + 45.006}{s + 0.7584} \tag{3.29}$$

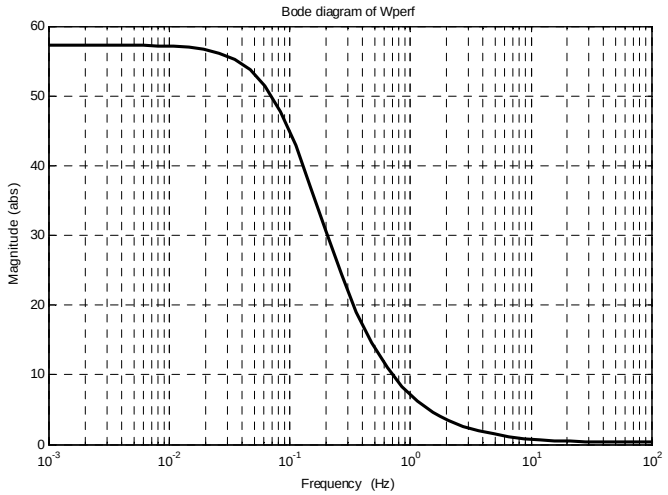

Figure 72. *Magnitude plot of the controller output,* $1/W_{perf}$

3.3.1.7 Weighting Function for Sensor Noise W_n

This function is used to represent the effect of encoder noise on the system. Possible reading errors are assumed to be same for all frequencies and defined in equation (3.30) below as:

$$W_{noise} = 2 \cdot 2 \cdot pi / 500 \tag{3.30}$$

3.3.2 H_∞ Controller Synthesis

After all these weighting functions and uncertainties are defined, it is now possible to create the generalized plant of the system as given in Figure 58. The generalized plant matrix could be formed using *'sysic'* built-in function. The synthesized plant matrix is given in Appendix A.4.

In order to simulate the controller performance, the system is modeled in SIMULINK® environment. The weighting functions and other parameters of the

system can be tuned using trial and error procedure. Now, using *'hinfsyn'* command, H_∞ controller can be designed as below.

```
[Kinf,CL,GAM,INFO] = hinfsyn(Pinf,1,1,'DISPLAY','on','METHOD','ric');
```

According to this equation, synthesized controller is 9th order and written as

$$K_{H_\infty} = \frac{\begin{array}{l}1.536\times10^{8}s^{8}+4.706\times10^{10}s^{7}+6.731\times10^{12}s^{6}+4.661\times10^{14}s^{5}+1.495\times10^{16}s^{4}\\ +2.259\times10^{17}s^{3}+1.965\times10^{18}s^{2}+9.153\times10^{18}s+1.455\times10^{19}\end{array}}{\begin{array}{l}s^{9}+1.087\times10^{5}s^{8}+1.374\times10^{9}s^{7}+3.627\times10^{11}s^{6}+4.471\times10^{13}s^{5}+2.255\times10^{15}s^{4}\\ +3.253\times10^{16}s^{3}+1.492\times10^{17}s^{2}+2.474\times10^{17}s+1.07\times10^{17}\end{array}}$$

The reduced order model of controller can also be obtained using *'reduce'* command. This controller can be reduced to 4th order. The controllers obtained here is discretized using Tustin's method. The step responses of the synthesized closed loop system with different plant uncertainties are illustrated in Figure 73.

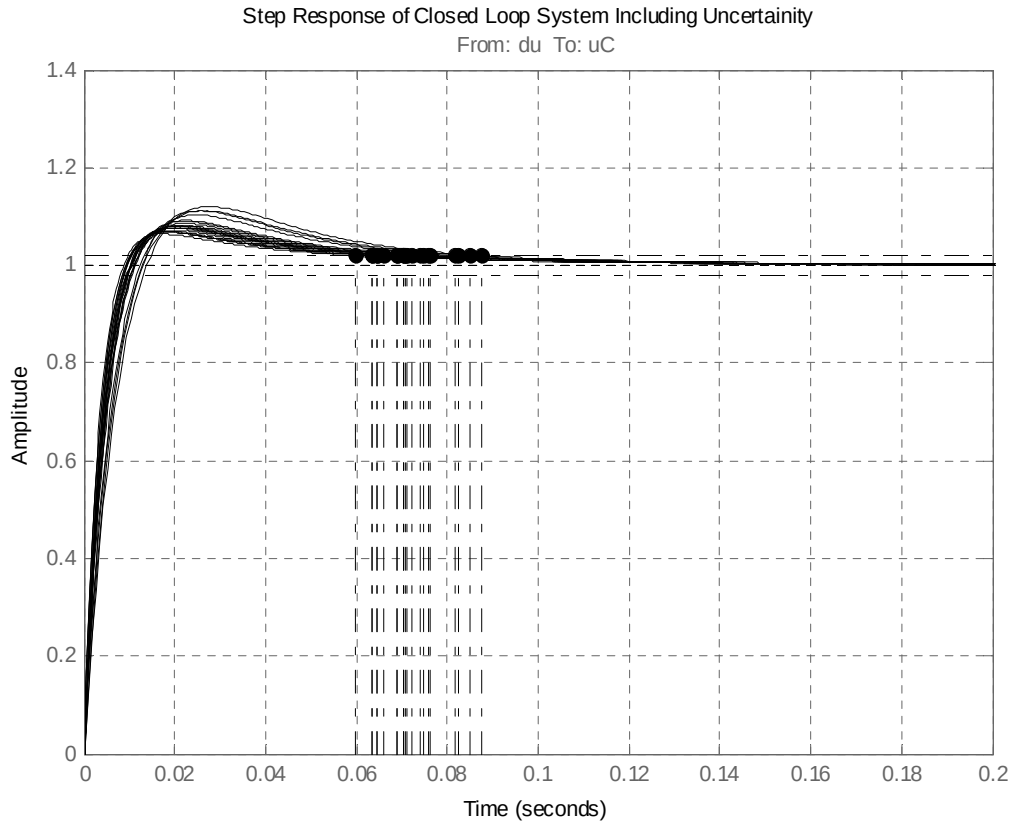

Figure 73. *Step response of the uncertain system*

According to these results, the settling time of the closed loop system with plant uncertainties is at most about 0.1 s which means that settling time is a bit longer than it was estimated. Besides, the singular value plot of the system shows that, in low frequency region, singular values of the system are below -120 dB which means that input disturbances could be attenuated more than 1e6 times at plant input.

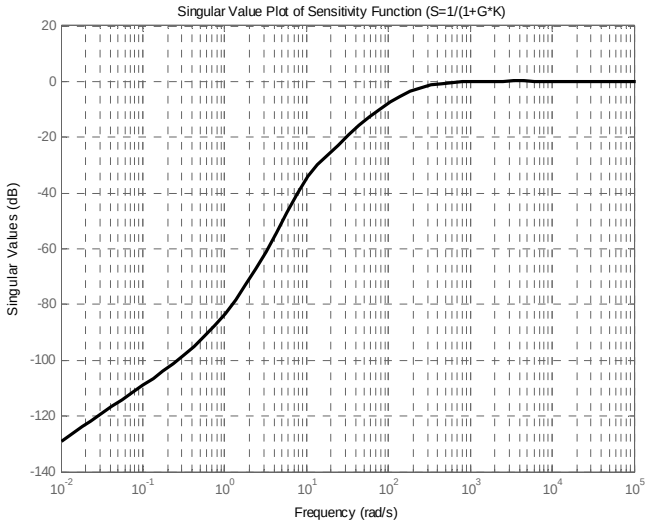

Figure 74. *Singular value plot of sensitivity function*

The bandwidth of the closed loop system is shown in is around 43 Hz which is higher than the minimum closed loop bandwidth.

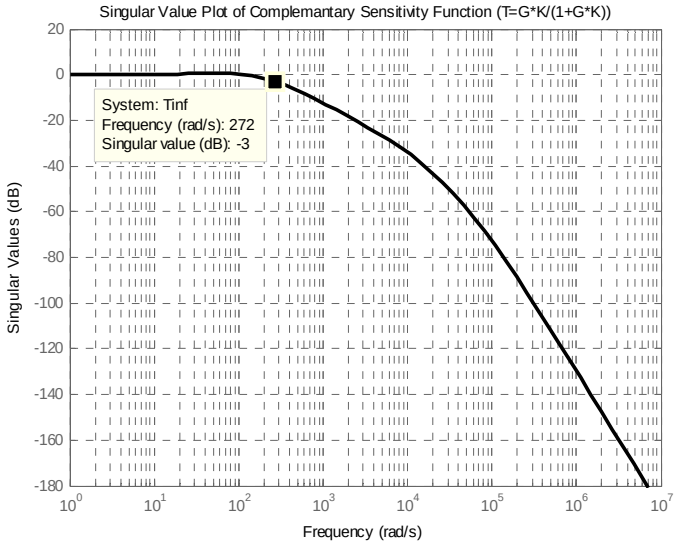

Figure 75. *Singular value plot of complementary sensitivity function*

The change of open loop gain and sensitivity function in accordance with the frequency is illustrated in Figure 76. This figure shows that the variation of the plant parameters do not change the system dramatically.

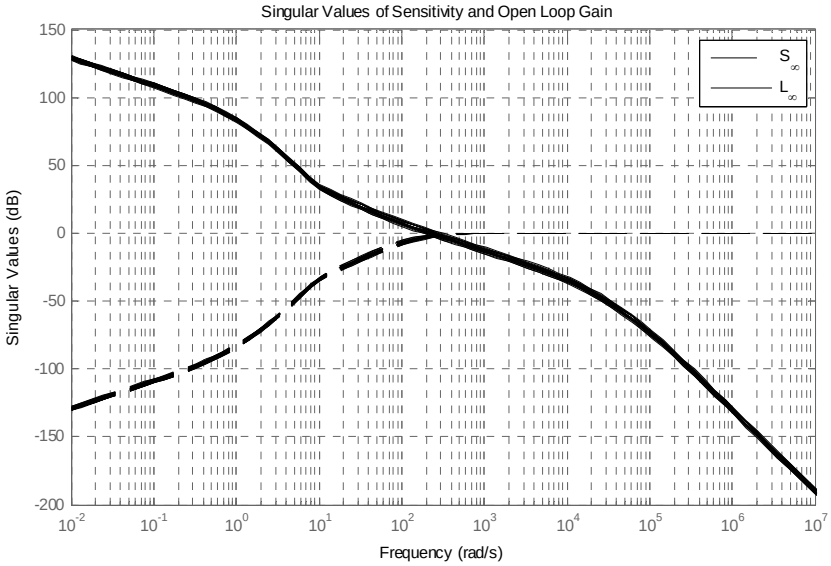

Figure 76. *Singular value plot of open loop gain and sensitivity function of uncertain system*

The simulation and experimental results of H_∞ controller is given in Figure 77. As can be seen from the, the simulation and experiment results are very similar which means that the identified system is also good enough. The controller signal of simulation and experimental data is also given in Figure 79.

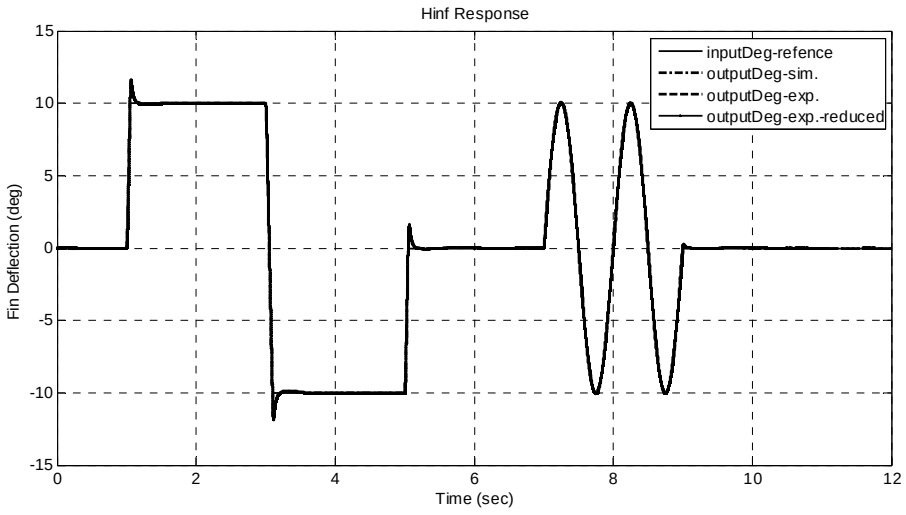

Figure 77. *Simulation and experimental results of H_∞ controller*

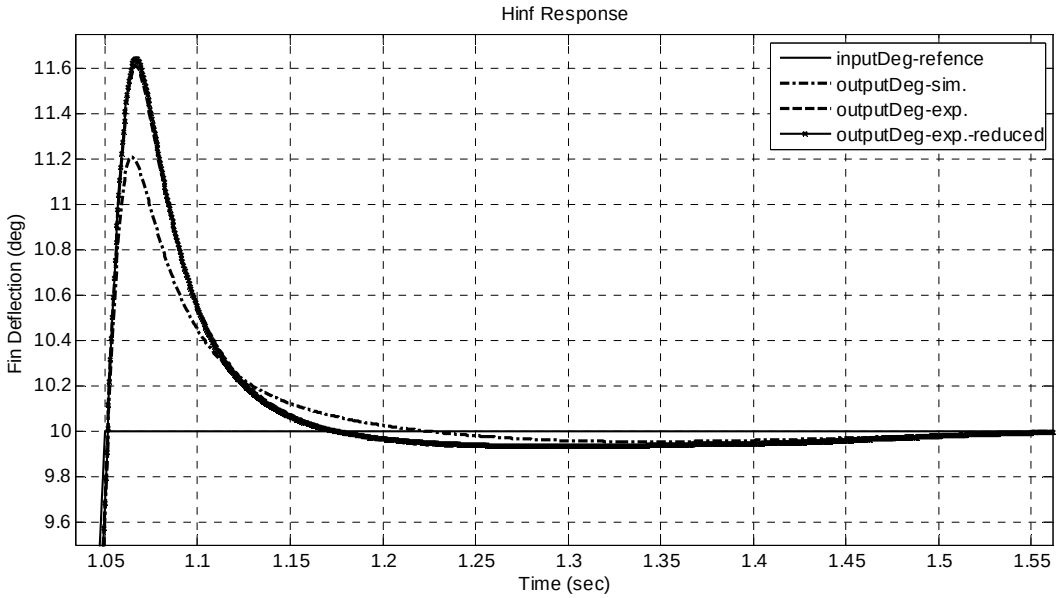

Figure 78. *Magnification of step response at t=1 s in Figure 76*

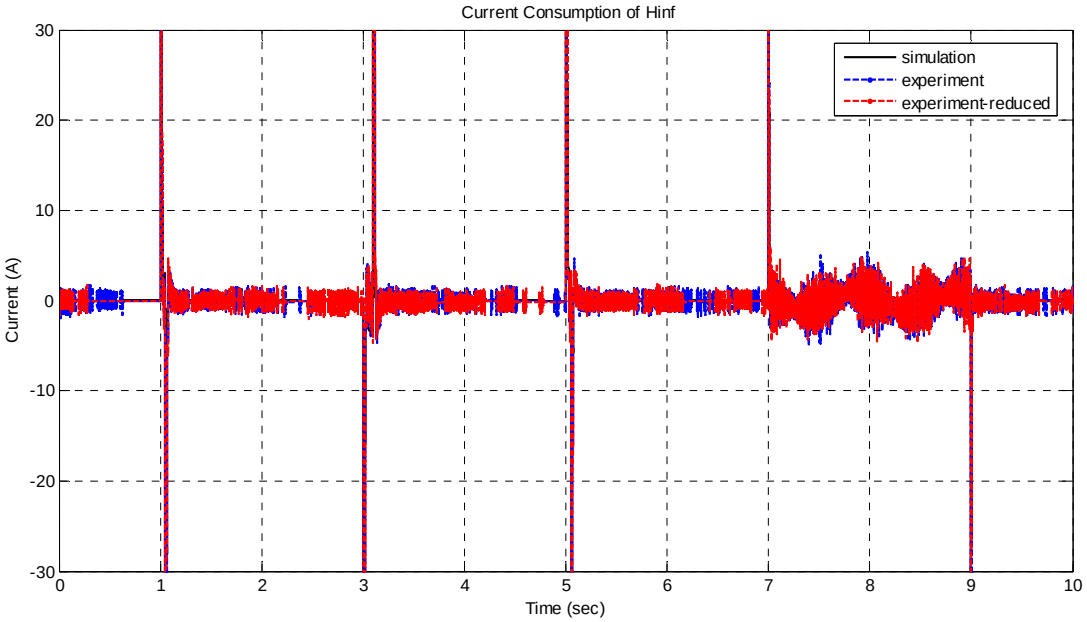

Figure 79. *Current consumption of H_∞ Controller*

3.3.3 2-DOF H_∞ Controller Synthesis

The H_∞ controller given in previous part can also be extended to 2 degree-of-freedom H_∞ controller. The block diagram of the 2-DOF H_∞ is given in Figure 55. The

weighting functions that is used in 2-DOF H_∞ controller is the same as in H_∞ controller. The designed 2-DOF controller is 9th order controller:

$$K_{2-DOF.H_\infty.r} = \frac{\begin{array}{l}4.89\times10^5 s^8 + 5.35\times10^8 s^7 + 2.909\times10^{11} s^6 + 7.526\times10^{13} s^5 + 1.14\times10^{16} s^4 \\ +1.057\times10^{18} s^3 + 5.054\times10^{19} s^2 + 9.522\times10^{20} s + 4.278\times10^{21}\end{array}}{\begin{array}{l}s^9 + 9681 s^8 + 2.144\times10^7 s^7 + 1.937\times10^{10} s^6 + 8.857\times10^{12} s^5 + 1.979\times10^{15} s^4 \\ +1.145\times10^{17} s^3 + 9.655\times10^{17} s^2 + 2.083\times10^{18} s + 5.491\times10^{17}\end{array}}$$

$$K_{2-DOF.H_\infty.\mathrm{y}} = \frac{\begin{array}{l}-3.56\times10^5 s^8 - 7.874\times10^{10} s^7 - 5.59\times10^{11} s^6 - 2.047\times10^{14} s^5 - 2.72\times10^{16} s^4 \\ -1.689\times10^{18} s^3 - 5.612\times10^{19} s^2 - 9.659\times10^{20} s - 4.279\times10^{20}\end{array}}{\begin{array}{l}s^9 + 968 s^8 + 2.144\times10^7 s^7 + 1.937\times10^{10} s^6 + 8.857\times10^{12} s^5 + 1.98\times10^{15} s^4 \\ +1.145\times10^{17} s^3 + 9.655\times10^{17} s^2 + 2.083\times10^{18} s + 5.491\times10^{17}\end{array}}$$

The step response of the feedback system including plant uncertainties is given in Figure 80. The obtained overshoot is below 20% and the settling time is also about 0.13 s. These results indicate that the obtained controller is quite similar to desired one except overshoot.

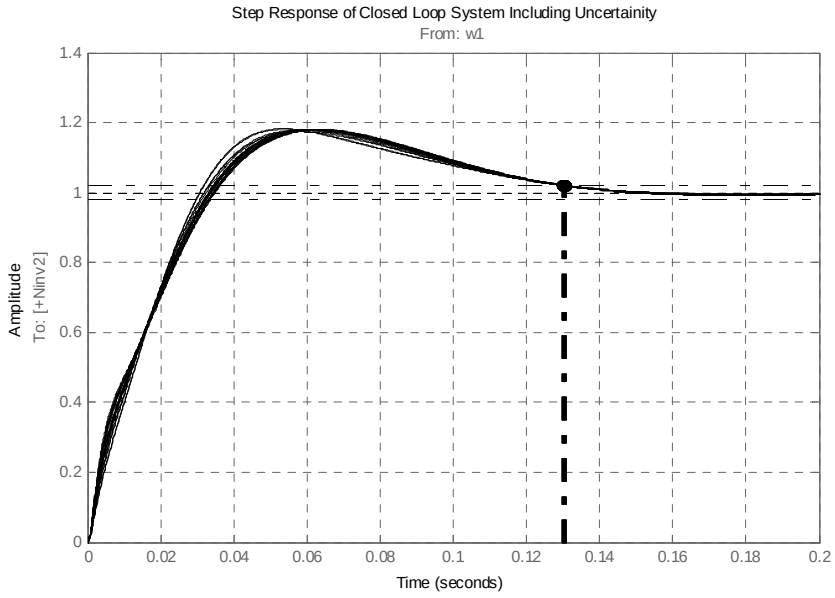

Figure 80. *Step response of the uncertain system (2-DOF H_∞)*

The robustness of the controller also seems well as seen from Figure 81. In low frequency region, singular values of the system is below -160 dB which means that input disturbances could be attenuated more than 1e8 times at plant input.

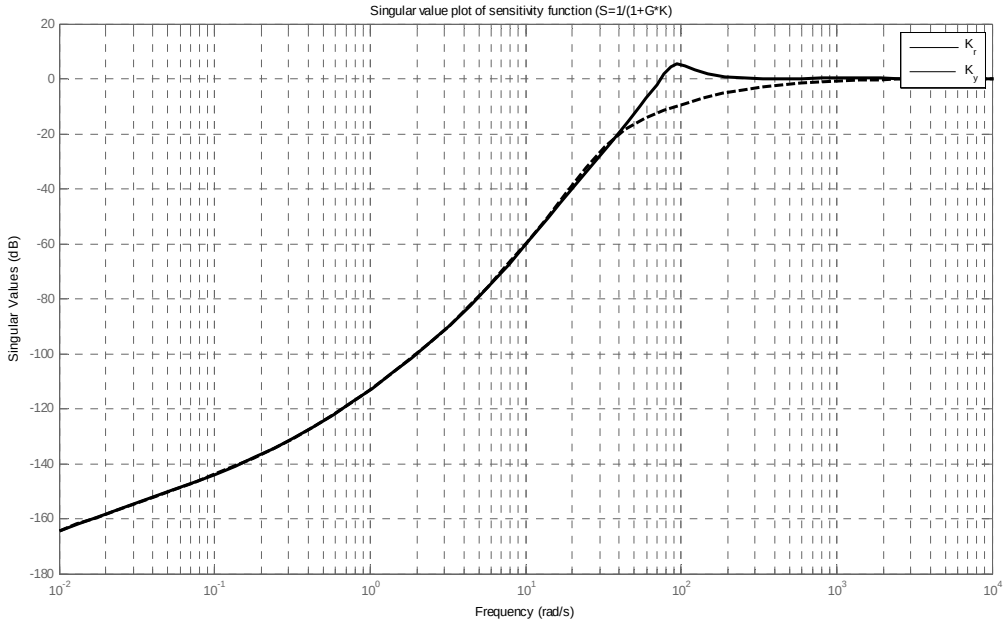

Figure 81. *Singular value plot of sensitivity function (2-DOF H_∞)*

The closed loop system bandwidth is about 10 Hz as seen in Figure 82, which is the lower limit of the desired bandwidth.

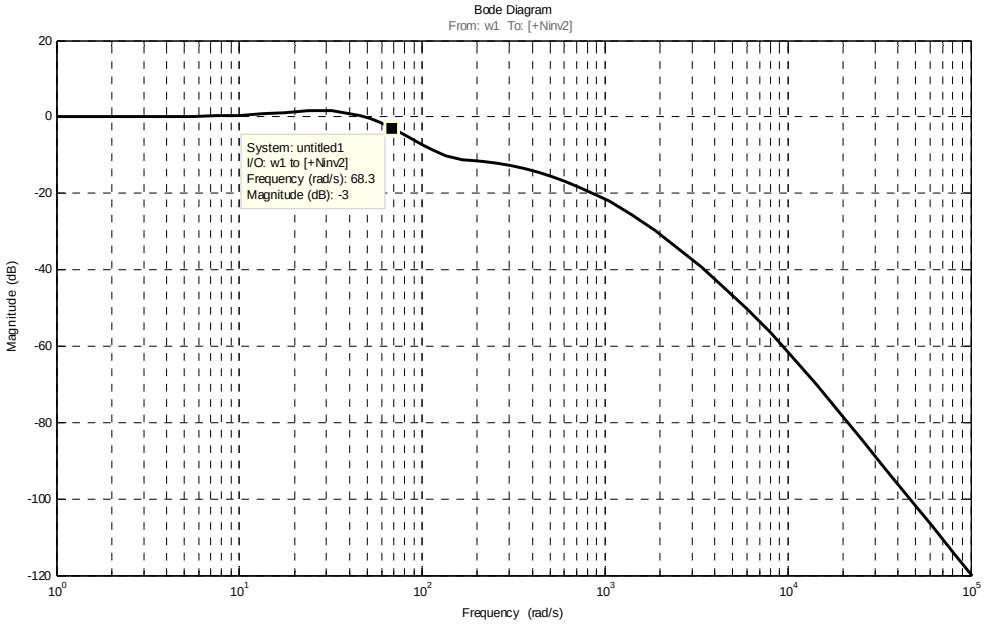

Figure 82. *Closed loop Bode diagram of 2-DOF H_∞ controlled system*

For uncertain plant, the robustness of the closed loop system does not change too much as seen from Figure 83.

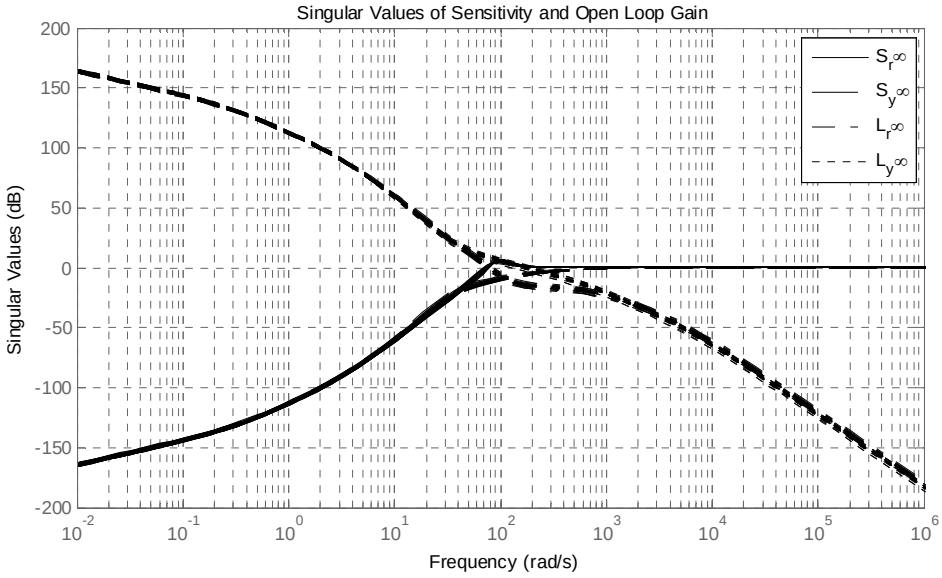

Figure 83. *Open loop gain and sensitivity function of uncertain system (2-DOF H_∞)*

This controller can also be reduced to 5th order. The simulation and the experimental results of the system are given from Figure 84 to Figure 86. For 2-DOF H_∞ controlled system experimental results are almost the same as in simulation results both pure and reduced controller.

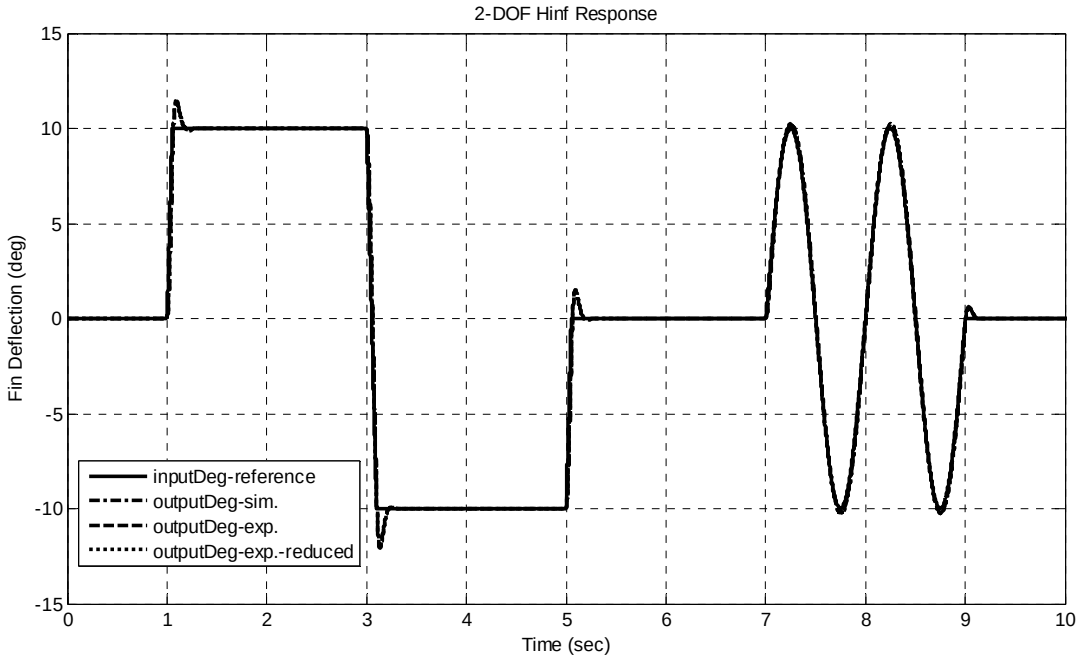

Figure 84. *Simulation and experimental results of 2-DOF H_∞ Controller*

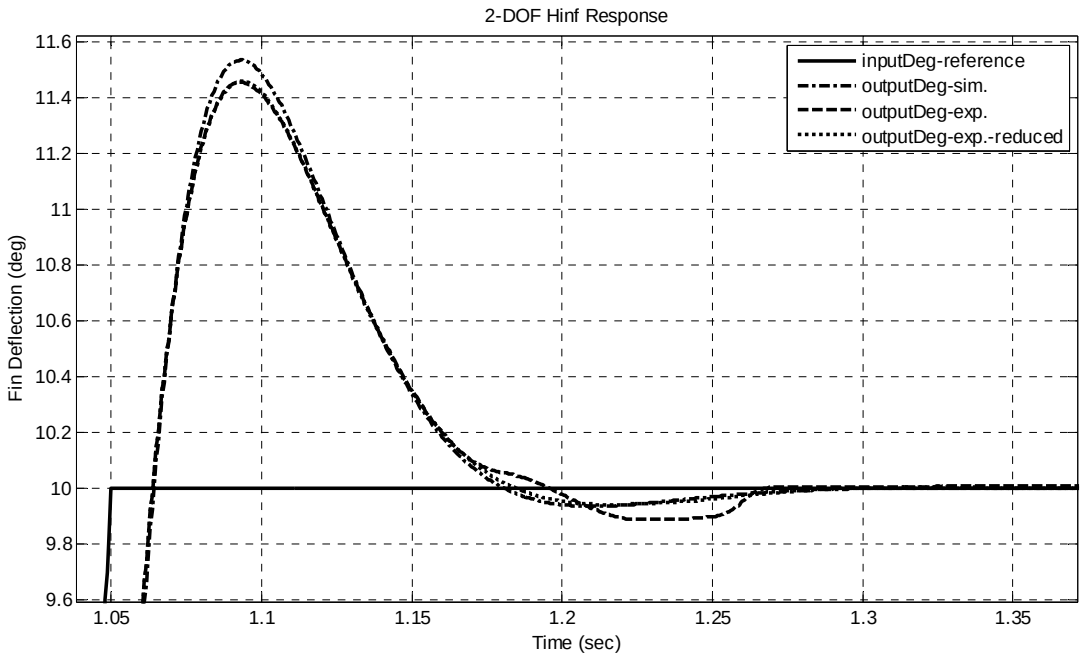

Figure 85. *Magnification of step response at t=1 s in Figure 84*

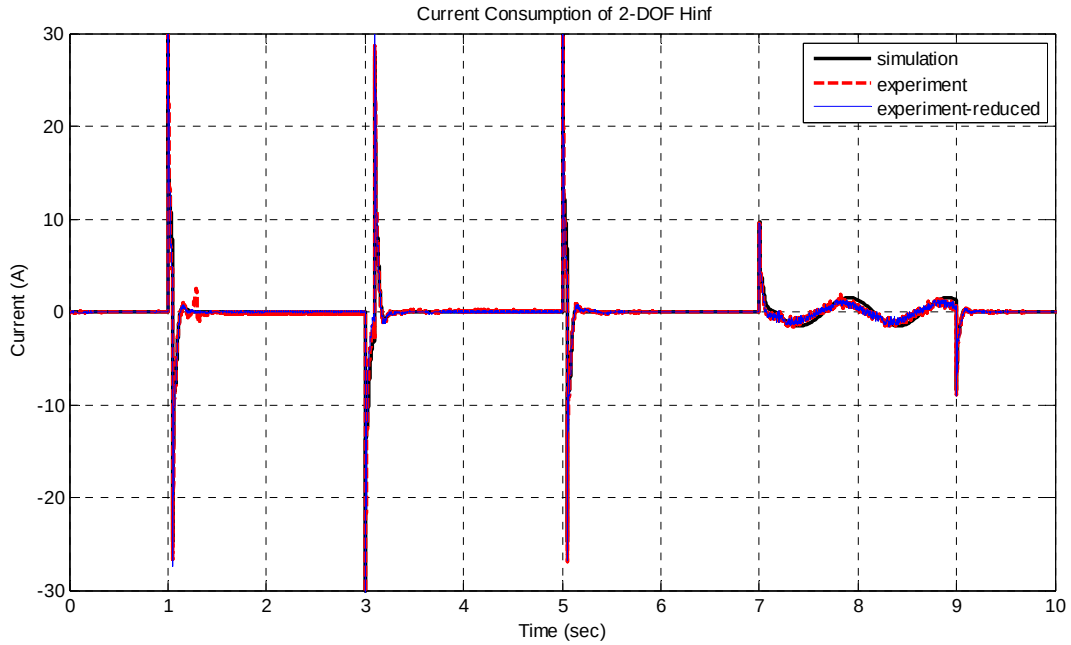

Figure 86. *Current consumption of 2-DOF H_∞ controller*

3.3.4 Cascaded H_∞ Controller Synthesis

Cascaded H_∞ controller is composed of two parts as given in Figure 56 and Figure 57. The first part is the inner loop of the system. The inner loop of the system is velocity controlled part which uses velocity as the measured signal and the outer loop

is the position controlled part; which uses the position as the feedback signal. The main idea, in cascade system is the inner loop should be at least 5 times faster than the outer loop so that it is possible to achieve a good control performance from the controller and the final closed loop system. In this thesis, the outer loop bandwidth which limits the whole system is about 20 Hz. The inner loop has 50 Hz bandwidth.

3.3.4.1 H_∞ Speed Controller

The weighting functions of the system are given in Appendix A.5. The weighting functions are a bit different than the other controllers since the velocity of the system is tried to be controlled; thus all the weightings are chosen according to the system limits in speed level. The synthesized controller is of 8th order. The step response of the closed loop speed control system with uncertain plant is given in Figure 87. As mentioned before, the transient region of the inner loop should be fast enough in order to control the whole system. As can be understood from the step response of the speed controlled system, the settling time changes from 0.035s to 0.08s.

$$K_{H_\infty \cdot speed} = \frac{\begin{array}{l} 570.2s^7 + 6.092\times10^5 s^6 + 3.236\times10^8 s^5 + 4.656\times10^{10} s^4 + 2.863\times10^{12} s^3 \\ +7.327\times10^{13} s^2 + 2.595\times10^{14} s + 2.161\times10^{13} \end{array}}{\begin{array}{l} s^8 + 5957s^7 + 5.374\times10^6 s^6 + 2.431\times10^9 s^5 + 1.936\times10^{11} s^4 + 3.553\times10^{12} s^3 \\ +1.397\times10^{13} s^2 + 4.77\times10^{12} s + 2.64\times10^{11} \end{array}}$$

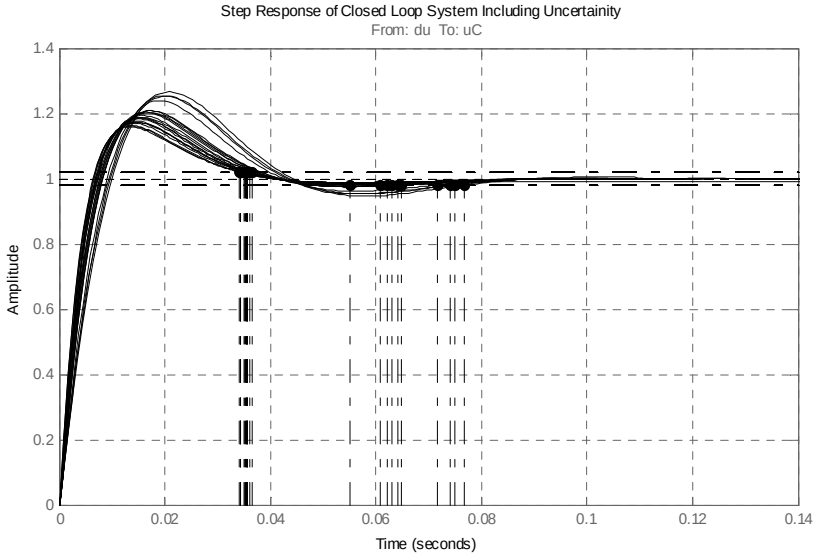

Figure 87. *Step response of the uncertain system (H_∞ speed)*

On the other hand, the sensitivity and open loop gain of the system is illustrated in Figure 88 which is similar to the previous controllers.

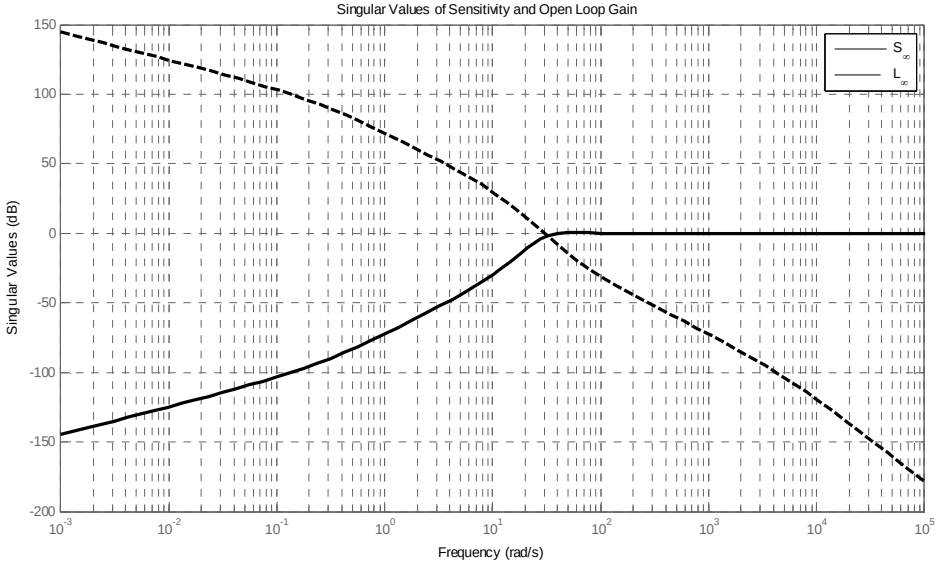

Figure 88. *Open loop gain and sensitivity function of the system (H_∞ speed)*

The closed loop bandwidth of the system is about 50 Hz as shown in Figure 89; which means that the bandwidth of the position controller cannot be higher than the 20 Hz. The simulation and experimental results of the system are shown from Figure 89 to Figure 92.

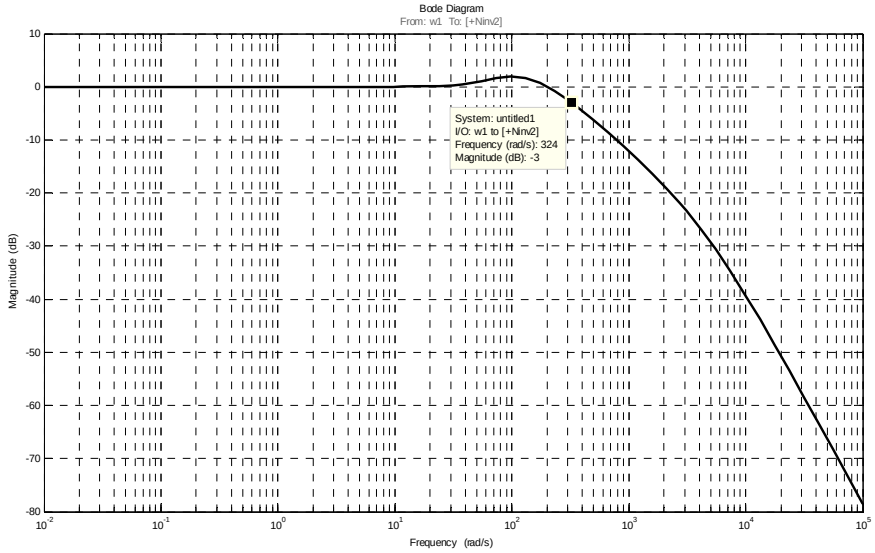

Figure 89. *Closed loop Bode diagram of H_∞ speed controlled system*

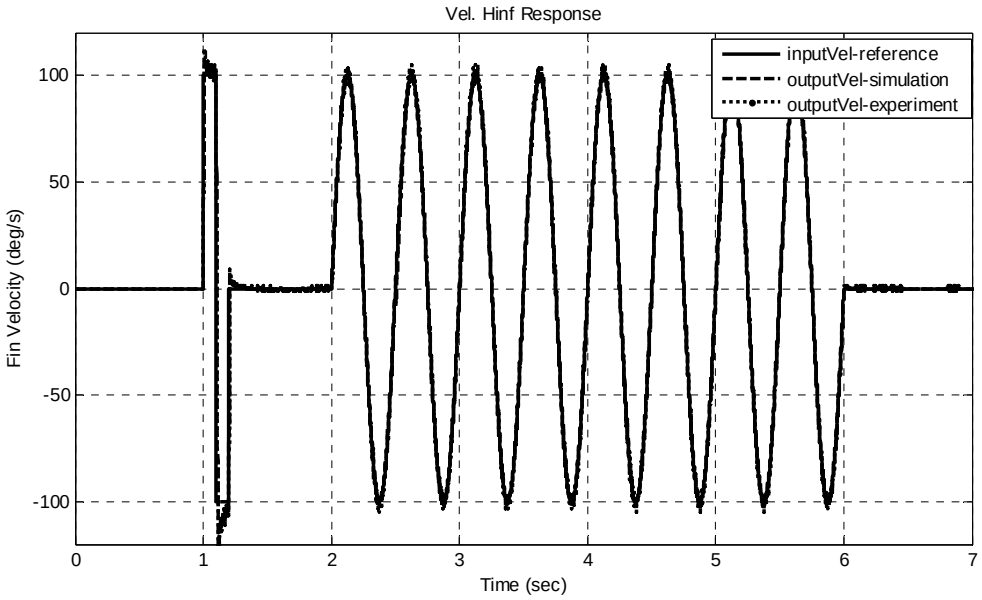

Figure 90. *Simulation and experimental results of H_∞ speed controlled system*

Note that from Figure 90 to Figure 92, the 100 degree/s step velocity input is given at the beginning of the test and the controller output is very similar to desired one. Here, the velocity information required for the velocity controller is obtained by taking the derivative of the position signal measured by means of encoder same encoder mounted to the motor shaft.

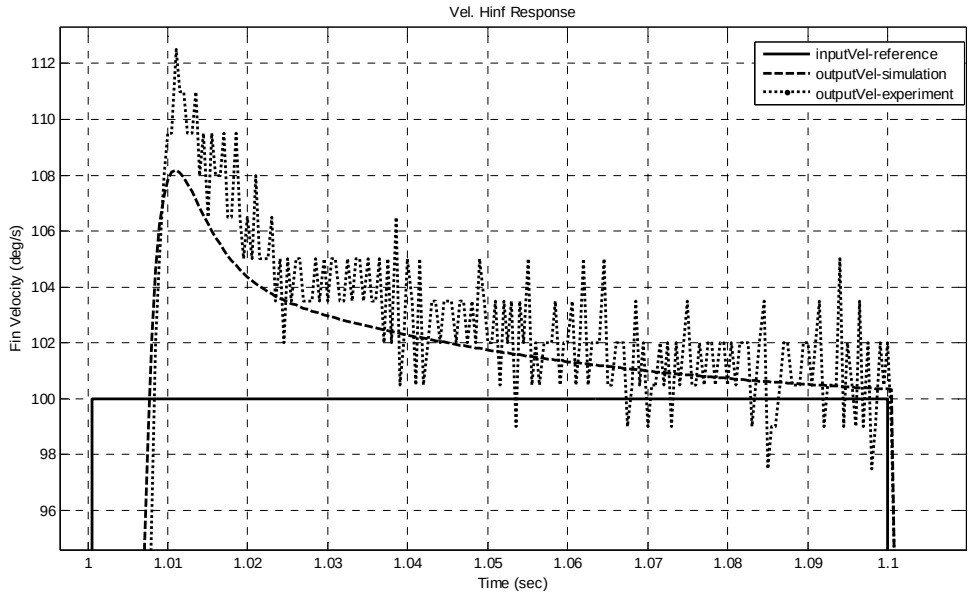

Figure 91. *Magnification of step response at t=1 s in Figure 90*

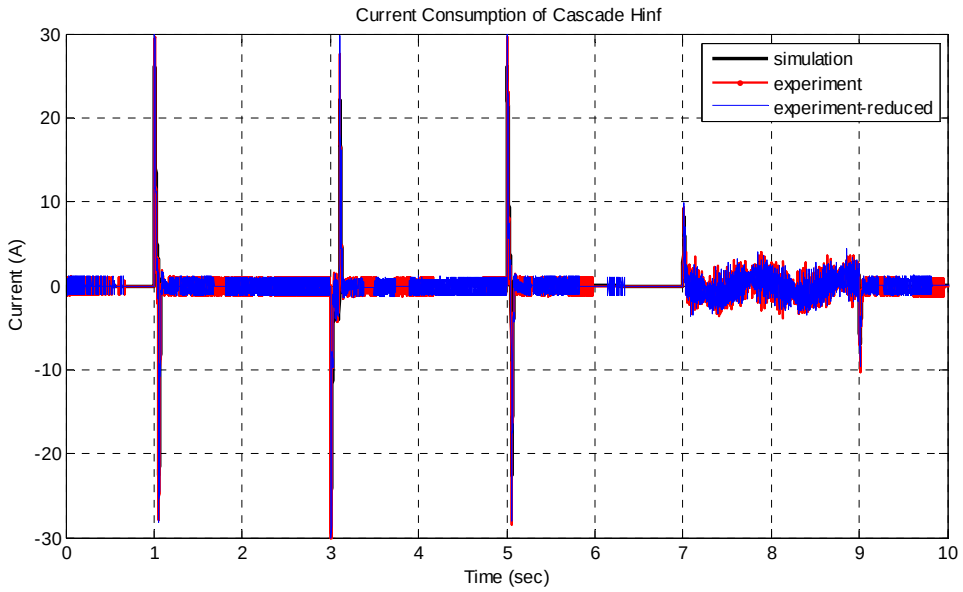

Figure 92. *Current consumption of H_∞ speed controller*

3.3.4.2 H_∞ Position Controller

The position controller determines the total bandwidth of the system in cascade methodology which is about 20 Hz as shown in Figure 93. This means that the outer loop of the system is 2.5 times slower than the inner loop having 50 Hz bandwidth. Although general trend says that this value should be 4-5 times, the simulation and experimental results reveal that the obtained closed loop bandwidth does not cause any contradiction and it is satisfactory for the plant considered in this thesis.

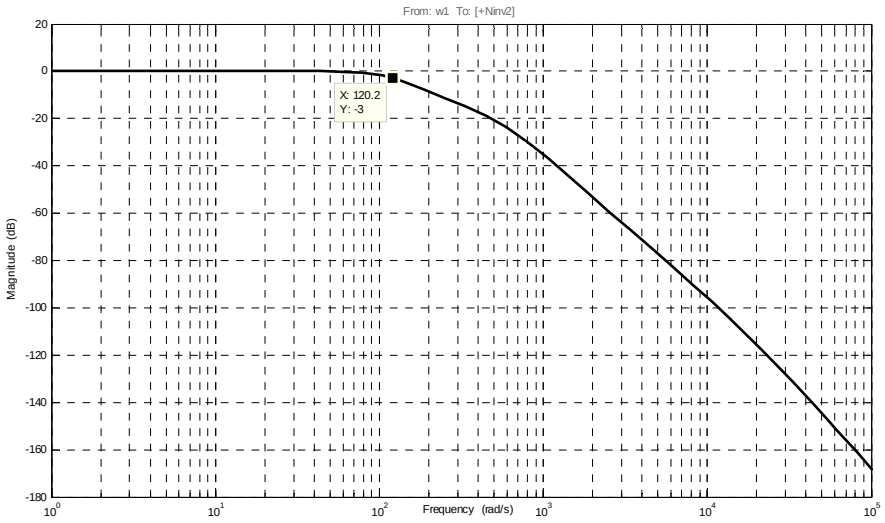

Figure 93. *Closed loop Bode diagram of cascaded H_∞ controlled system*

The responses of the closed loop position control system to the reference input are given in Figure 94 and Figure 95. On the other hand, the output signal of the controller; that is the current signal, is shown in Figure 96.

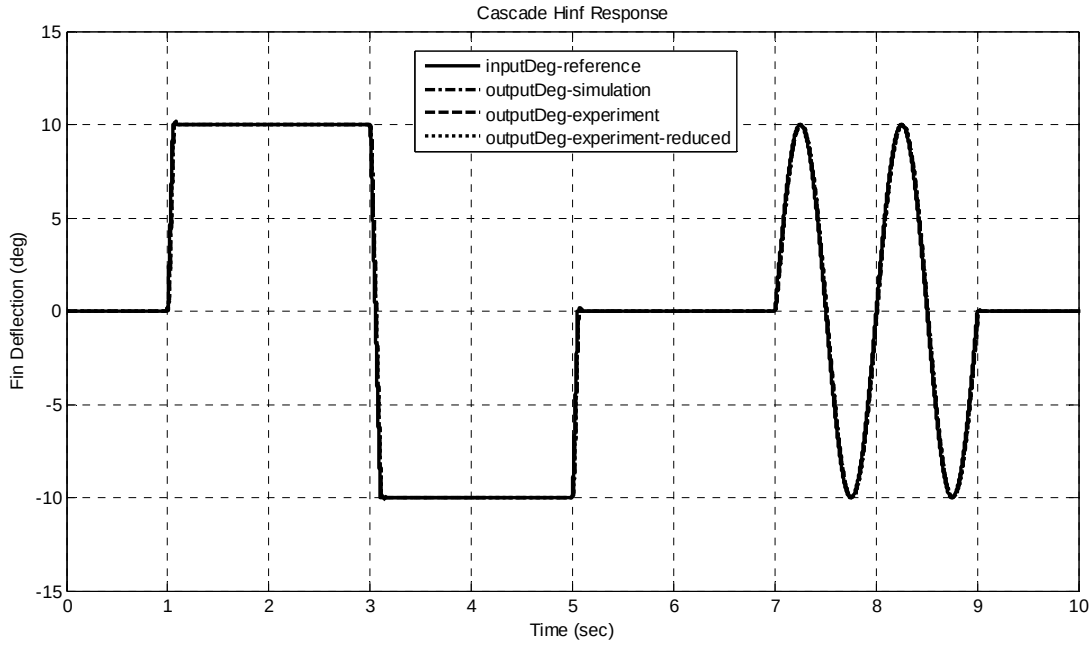

Figure 94. *Simulation and experimental results of cascaded H_∞ controller*

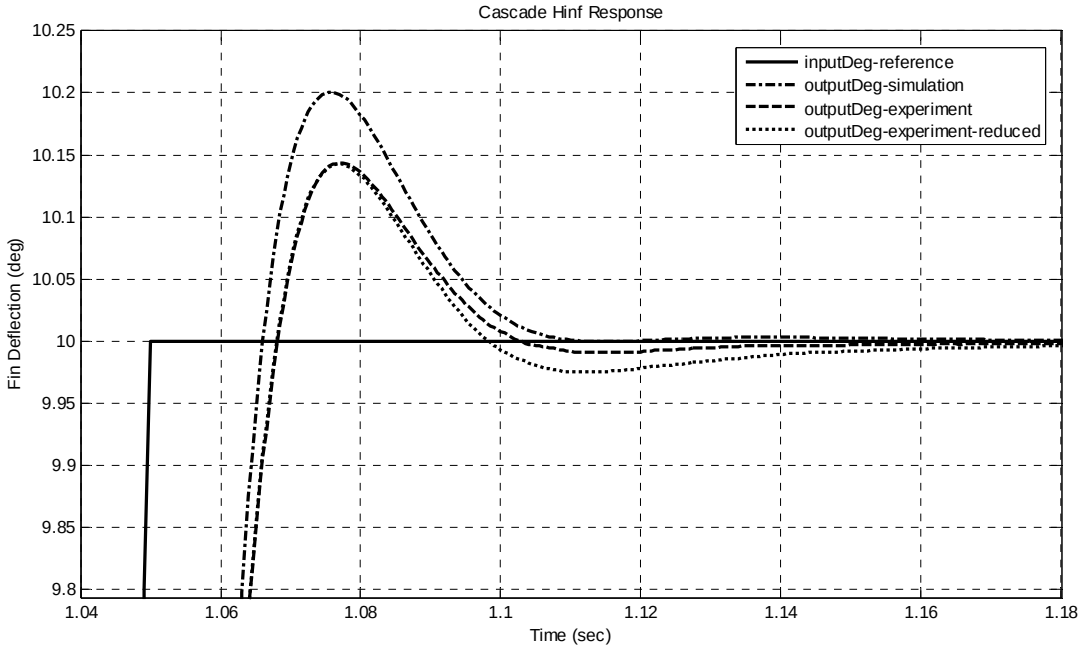

Figure 95. *Magnification of step response at t=1 s in Figure 94*

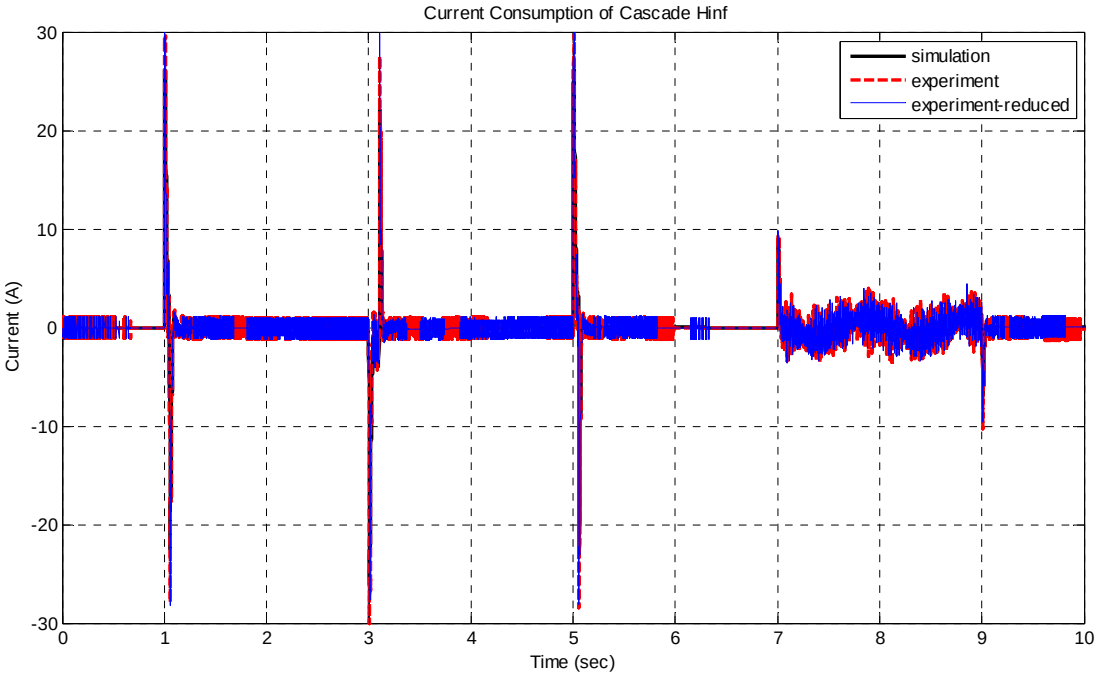

Figure 96. *Current consumption of cascaded H_∞ controller*

CHAPTER 4

COMPUTER SIMULATIONS AND EXPERIMENTS

At this point, three different H_∞ controllers and PID controller were synthesized. In this thesis, the aim is to compare the cascaded H_∞ controller with pure 1-DOF H_∞ and 2-DOF H_∞ controllers. Although,, the obtained controllers do not meet the desired requirements exactly, the best performance is obtained in cascaded H_∞ controller. During the design processes, nearly the same weighting functions are chosen such that it is possible to make reasonable comparison of the performance of the controllers and closed loop position systems.

4.1 Simulation Results

The sensitivity functions of controllers for nominal plant is given in Figure 97. All of the controllers satisfy the robustness criteria. As expected, the sensitivity functions of the closed loop systems are well below the 0 dB.

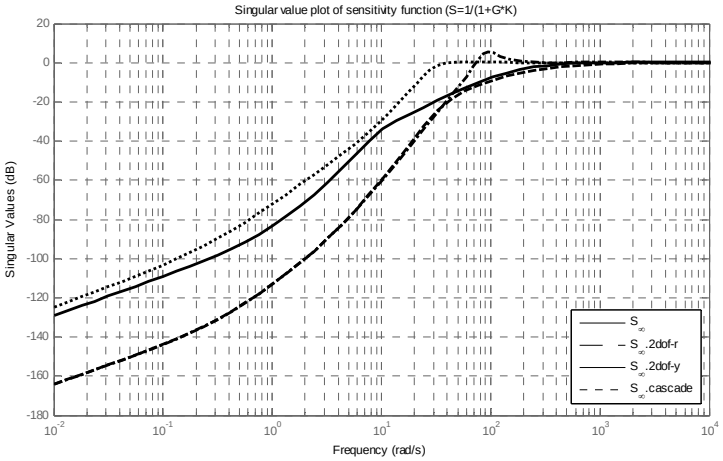

Figure 97. *Sensitivity functions of the closed loop systems with different controller*

The loop transfer function with different controllers is also given in Figure 98. The behaviors of the systems seem similar which means that disturbance attenuations of the closed loop systems are similar.

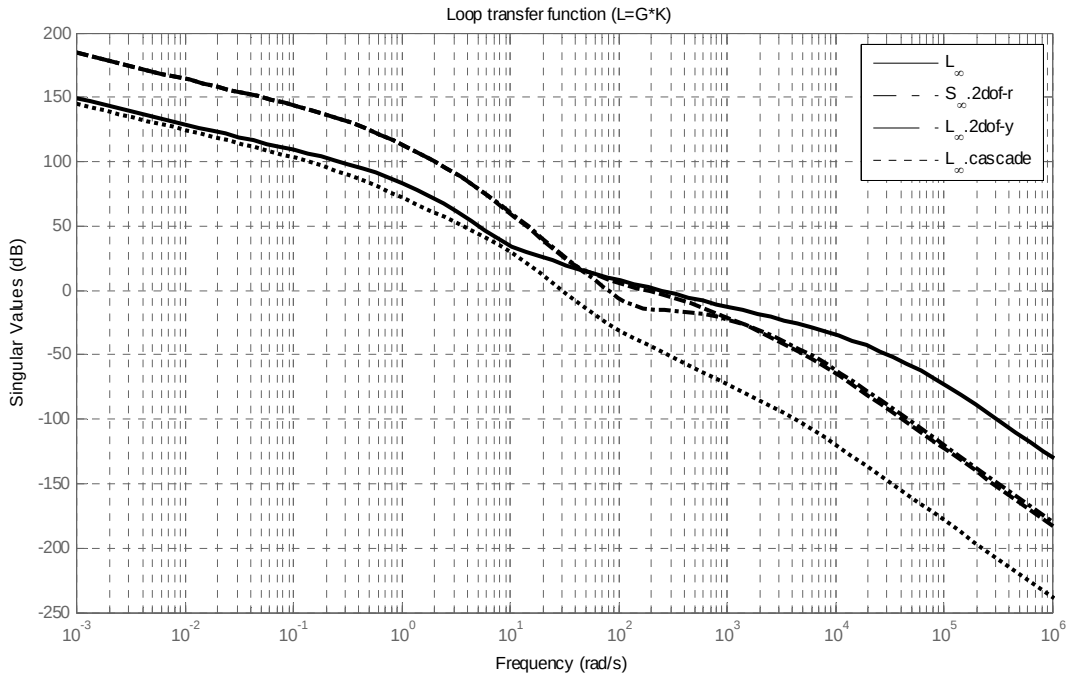

Figure 98. *Singular value plot of the loop transfer functions with different controllers*

The simulation results shows that although bandwidth of the cascade H_∞ is lower than pure 1-DOF H_∞ controller, the settling time of the cascade H_∞ controller is shorter than the others as given in Figure 99. Moreover, the peak response of the cascade controller is also lower than the others. When the bandwidths of the systems are compared as in Figure 100, the lowest one is 2-DOF H_∞ controller which is 10 Hz. The second one is cascaded H_∞ controller and its bandwidth is around 20 Hz. Although the fastest system seems pure H_∞ controller, performance of the cascaded H_∞ in tracking the step position input signal is better than the others.

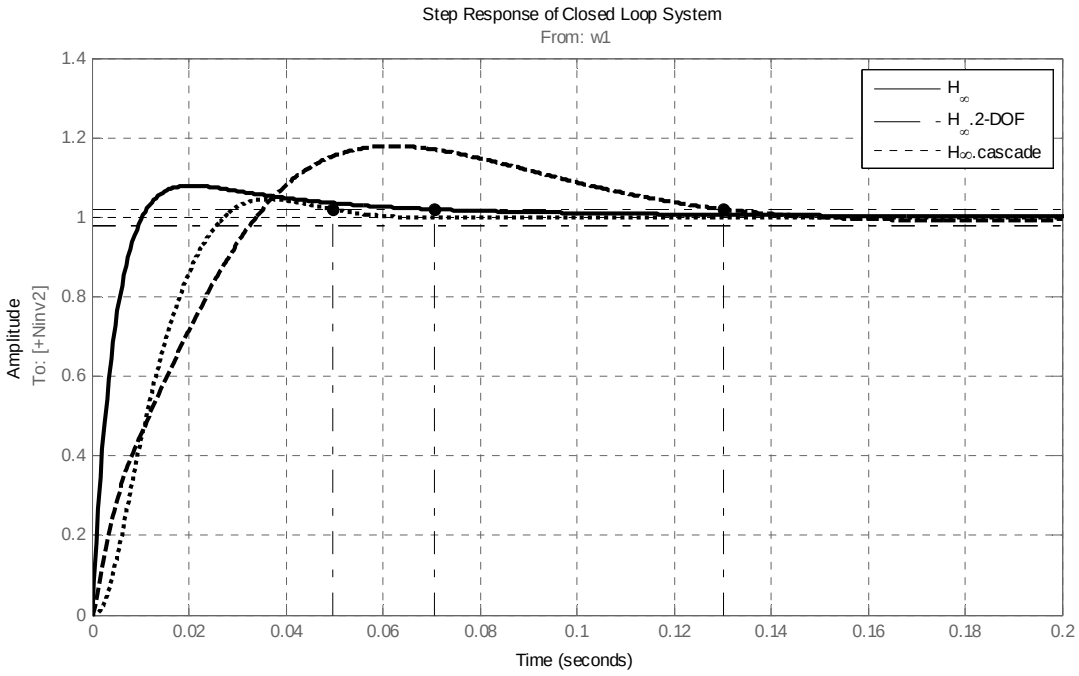

***Figure 99**. Step response of controllers*

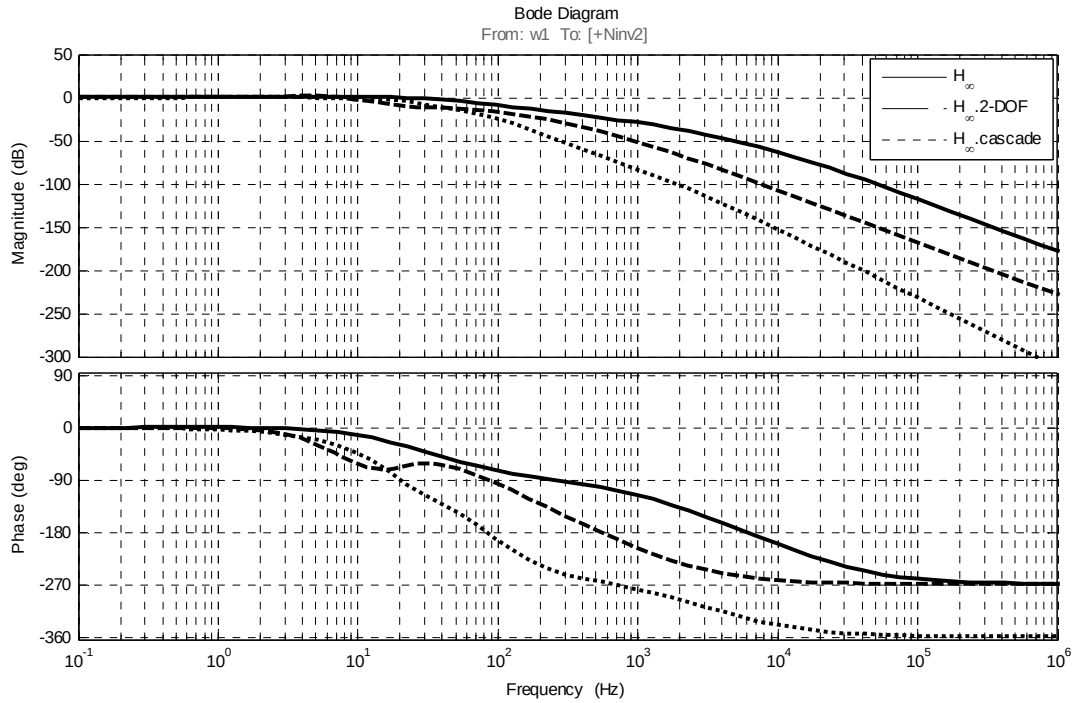

***Figure 100.** Bode diagrams of the closed loop system*

4.2 Experimental Results

As expected, experimental results are similar to simulation results. Especially, 1-DOF H_∞ and 2-DOF H_∞ performances are close to each other. In this section, the reference signal is considered as the only input to the closed loop systems and secondly, the comparisons of the closed loop systems are done by taking into account both the reference signal and external disturbance input.

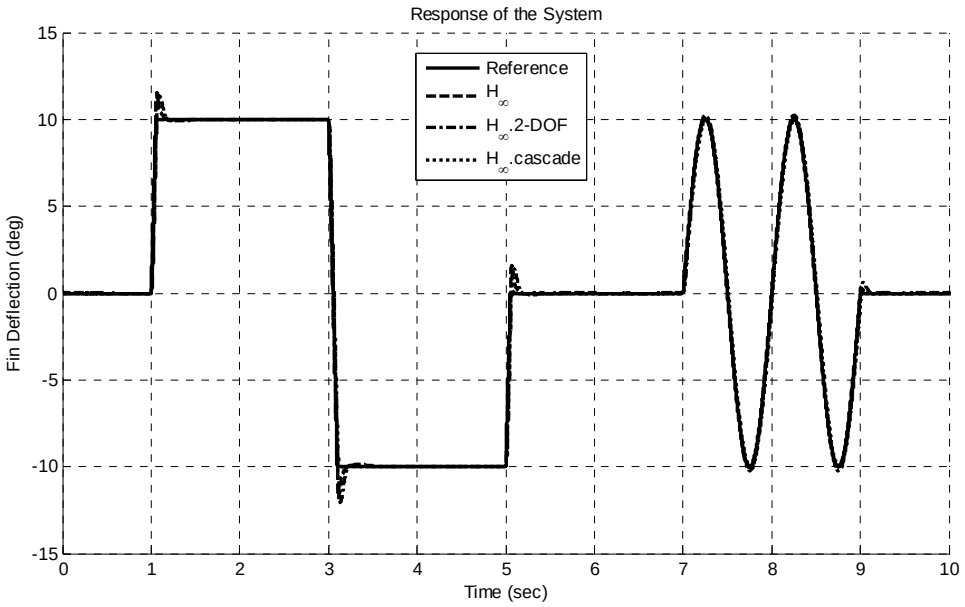

Figure 101. *Responses of the closed loop systems*

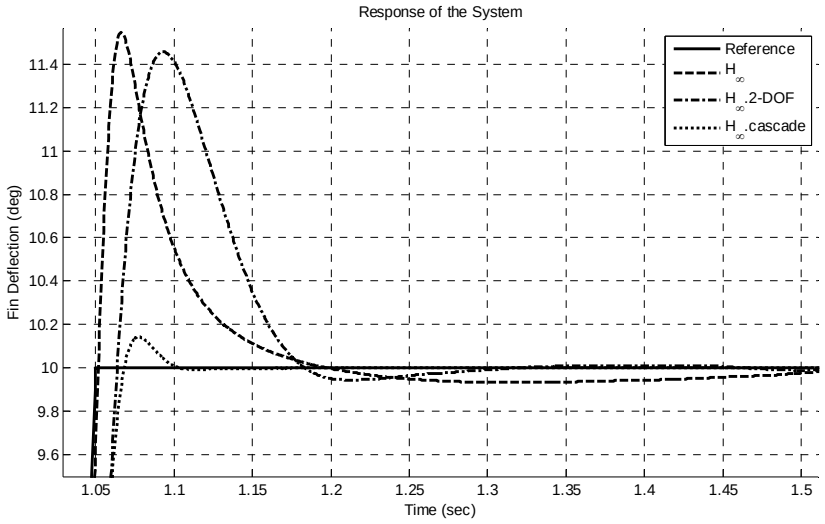

Figure 102. *Detailed view of the step responses at t=1 s in Figure 101*

When the current consumption of the controllers are considered, it can be seen from Figure 103 that 1-DOF H_∞ controller current consumption is higher than the others. Current commands for 2-DOF H_∞ and cascaded H_∞ controllers are very similar to each other.

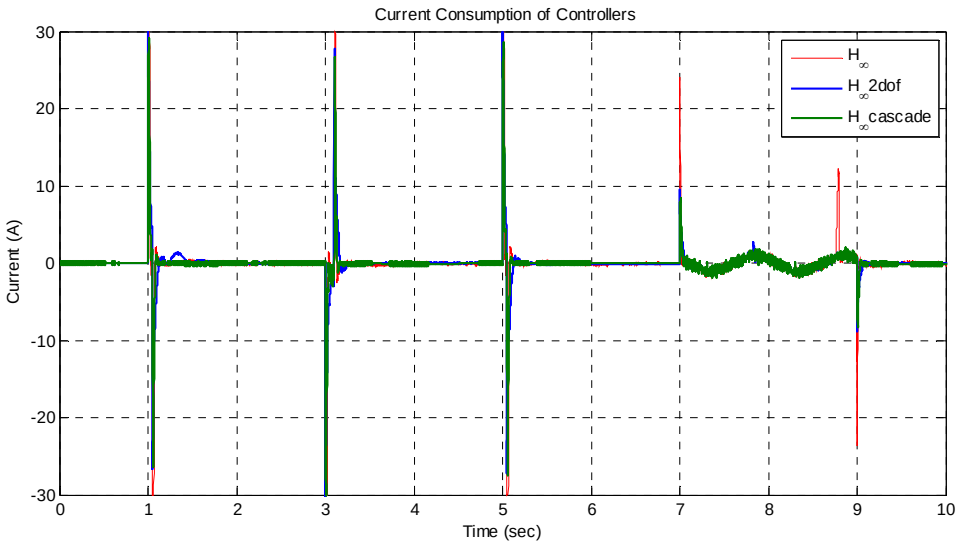

Figure 103. *Controller output of the system*

The closed loop systems are also tested with sinusoidal signal whose amplitude is 10 deg and frequency 1 Hz. The reference tracking of the controllers are given in Figure 104.

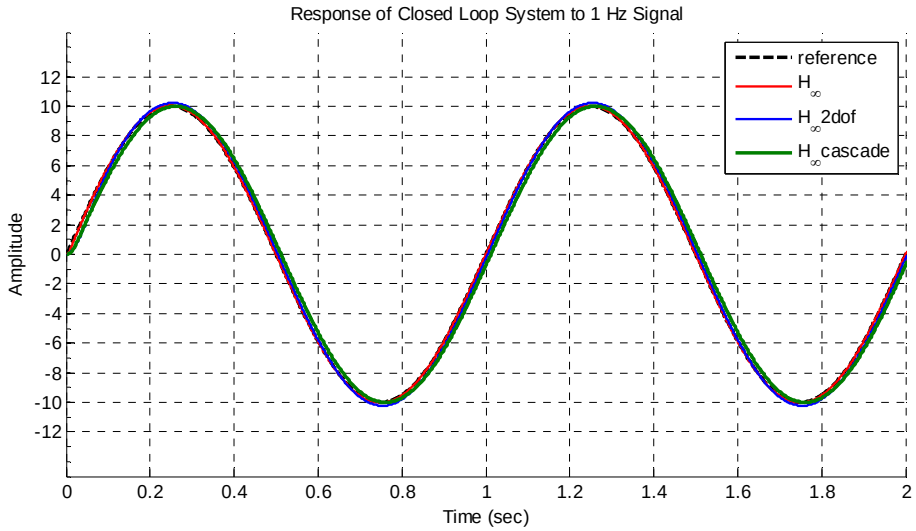

Figure 104. *Response of the system to 1 Hz signal*

The 1-DOF H_∞ controller makes more overshoot than 2-DOF H_∞ controller while cascaded H_∞ controller tracks the reference signal with a little time delay. The controller output of the system is given in Figure 105. For 1 Hz sinusoidal input, the characteristics of the controller outputs are nearly same.

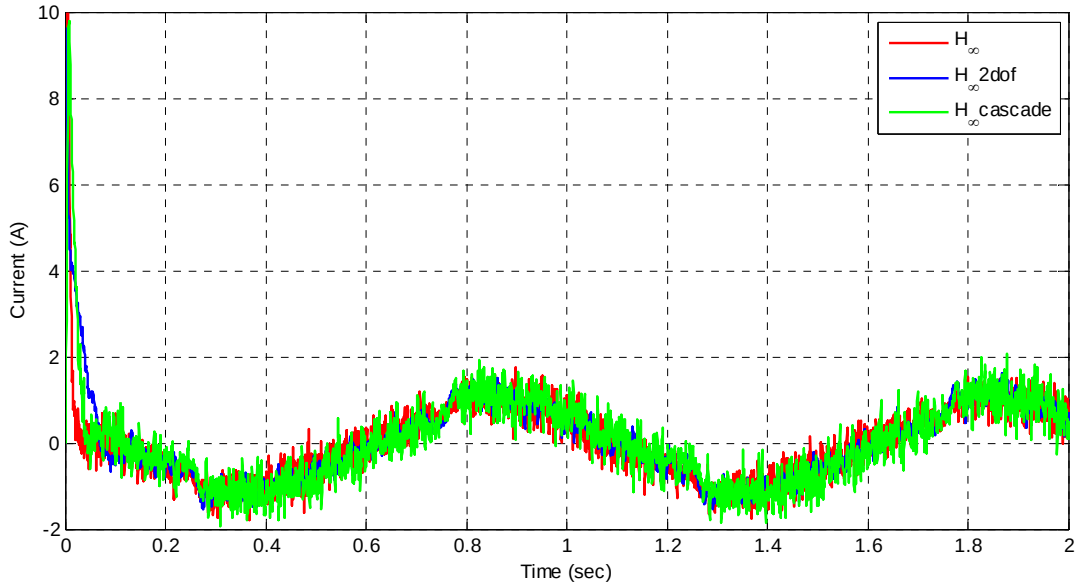

Figure 105. *Controller output of the system to 1 Hz signal*

On the other hand, all the robust controllers are also tested under variable external load. The load that is applied to the closed loop systems is varying from -20 Nm to 15 Nm. Before the application of the load, the system is tried to be held at 0° position by the controllers and then the load is applied to the system. The closed loop system responses to variable load are depicted in Figure 106 and loads are shown in Figure 107 in terms of current since the disturbance can be applied manually. As can be seen from Figure 106, when the load is removed, the 1-DOF H_∞ controller makes more oscillations in position response than the other controllers. For instance, at time 14 s, when the load removed from the system, the oscillation of the 1-DOF H_∞ reach 0.3 degrees. 2-DOF H_∞ controller also behaves like 1-DOF H_∞ controller but the peaks of the oscillations in position response are less than 1-DOF H_∞ controller and the amplitudes of the peaks do not exceed 0.13 degrees. Here, cascaded H_∞ controller has the best response in the existence of the disturbances even if higher disturbance

forces as compared to the other controller cases than others. The oscillations of the cascade controller are very low when compared to others controllers and its deflection from the 0° does not exceed 0.03° at the fin side.

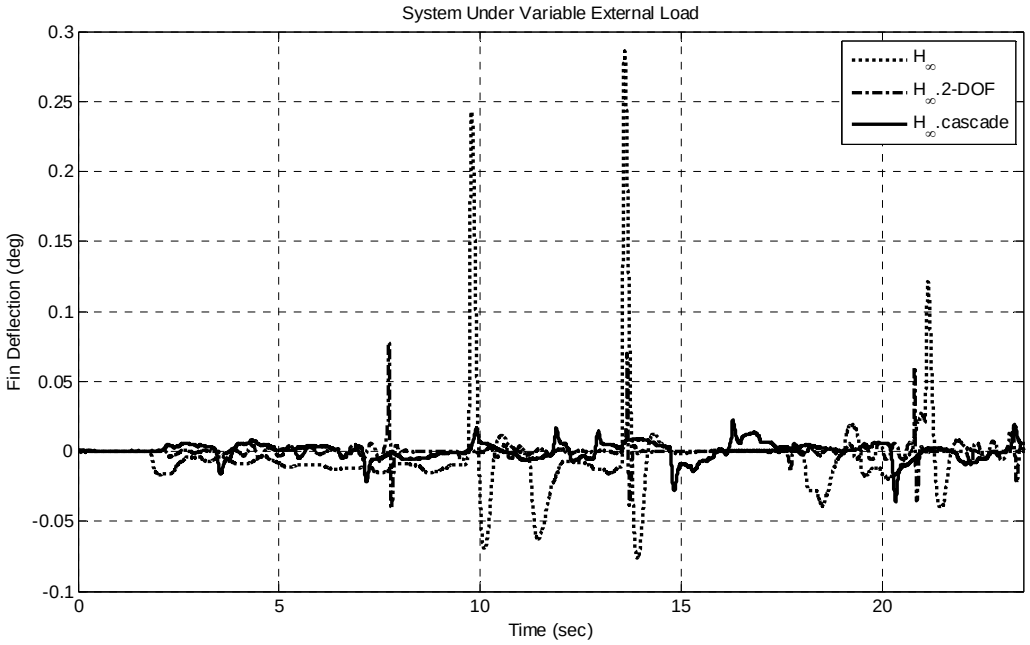

***Figure 106**. Reference tracking of the system under variable disturbance*

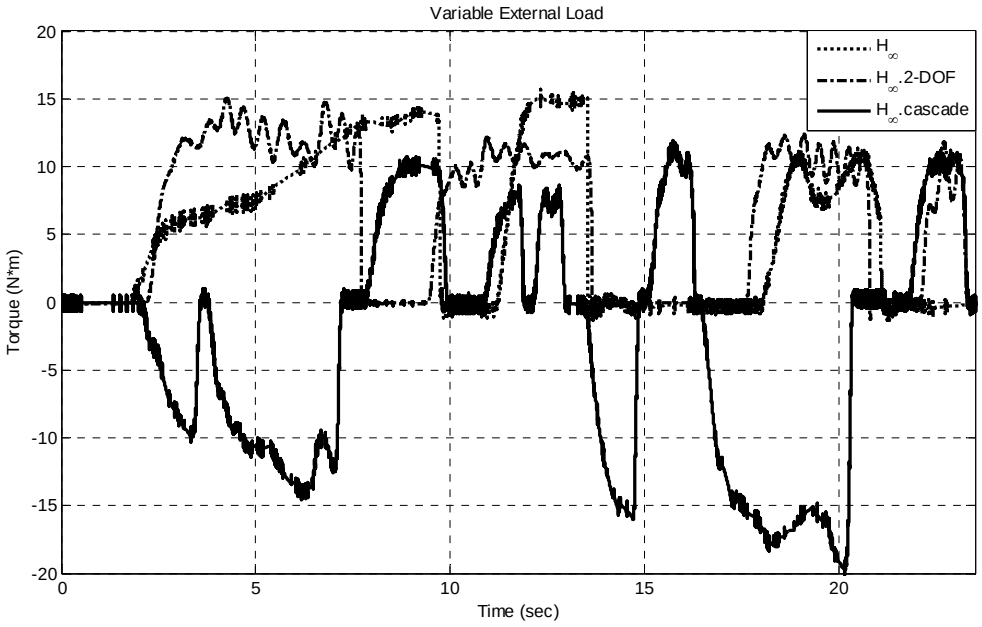

***Figure 107.** Controller output of the system under variable disturbance*

4.2.1 Experimental Bandwidth of the System

As mentioned before, the bandwidth of the cascade controller is given 20 Hz in previous part. One of the experimental methods to determine the closed loop system bandwidth is exciting the system using chirp signal. In Figure 108, the response of closed loop system with cascaded H_∞ controller to chirp signal is given. If the closed loop system is assumed to be an ideal standard second order system; the frequency where magnitude ratio as compared to the beginning of the signal is 0.707 can be accepted to give the bandwidth of the system. Then, the bandwidth of the system is found as 19.5 Hz which is very close to simulation results; therefore, bandwidth of the other controllers could also be found in the same manner.

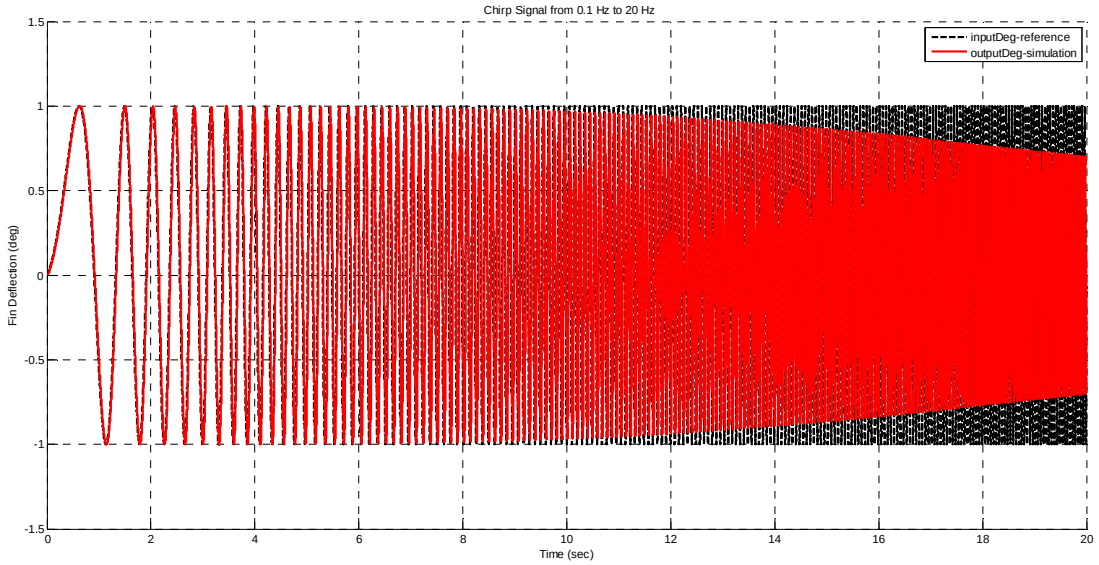

Figure 108. *Response of H_∞ cascaded controlled system to chirp signal*

The comparison of the controllers is also given in Table 6. It can be seen that the percent overshoot and the settling time of the cascade controller is better than others. As mentioned before, the aim of the robust controller is to be stable for variable plant uncertainties. Using *'robuststab'* command of Matlab®, it is possible to make a robustness analysis to the uncertain plant. This command tells the upper and lower bound of stability margin. If lower bound of the stability margin is higher than 1, than it is concluded that the system is robustly stable to plant uncertainties. For 1-

DOF H_∞ and 2-DOF H_∞, the controllers can tolerate up to 150% to model uncertainty while cascade H_∞ can tolerate up to 300% to model uncertainty.

Table 6. *Comparison of the robust controllers*

		Ideal System	**H_∞**	**2-DOF H_∞**	**Cascaded H_∞**	
					Position (outer loop)	**Speed (inner loop)**
Gamma Value 'γ'		-	5.6906	2.8850	1.4453	1.7007
Bandwidth (Hz)		20	43.29	11.6	20.9	51.6
Settling Time (s)		0.048	0.07	0.13	0.045	0.036
Overshoot (%)		4.32	7.93	17.9	4.59	18.6
W_{ideal} (Hz)		20	20	20	20	100
Controller Order		-	9	9	8	8
Reduced Order		-	4	5	4	5
robuststab	**Lower Bound**	-	1.5000	1.5000	-	2.9998
	Upper Bound	-	1.5000	1.5000	-	3.0000
	Destabilizing Frequency	-	0.3204	0.6891	-	0.0059

CHAPTER 5

DISCUSSION AND CONCLUSION

5.1 Summary and Comments on the Results

In this study, modeling, identification, simulations, and experiments of the control system for a fin actuation system is studied. In this respect, firstly PID controllers are designed and their performance are compared. Then, 1-DOF, 2-DOF, and cascaded H_∞ controllers are synthesized. All the controllers are simulated in computer environment and then these controllers are applied to physical system.

In order to make experiments, initially, the mathematical model of the system is obtained. In this section, the electrical part of the system is neglected because of the very high band width frequency of the driver card. This simplified model is used both on identification and simulation parts. The obtained mathematical model is tired to be verified using a standard system identification procedure. In this respect, PRBS and BLWN signals are applied to system as the input. The obtained input/output data set is firstly converted to frequency domain and then all the identification procedure is carried out in frequency domain. The identified model appeared to be a second order system with a free integrator. This model is obtained in two ways. In first way, all the parameters are assumed unknown and found in certain intervals. In second way, the motor torque constant and equivalent inertia of the system are computed and using these values equivalent viscous friction of the system is estimated. In controller synthesis, the first way is chosen.

As mentioned before, three different PID and H_∞ controllers are synthesized. In first PID, Butterworth polynomials are used in order to place the poles of the closed loop

control system as per the desired bandwidth and nondimensional damping quantities. This way, it becomes possible to find the gains of the controller. The second one is designed using *'pidtool'* command of Matlab®. The final PID controller is obtained using experimental approach. In this PID, Ziegler-Nichols tuning method is utilized to determine the controller gains. The simulation and experimental results show that the current consumption of PID controllers is higher than their robust counterparts. The performance of the PID controllers is a bit lower than expected. Thus, in Chapter 4, the PID controllers are not compared with the robust controllers. After that, H_∞ controllers are designed, simulated and tested. The weighting functions of H_∞ controllers are decided according to physical performance requirements and physical limits of the system. For 1-DOF and 2-DOF controllers same weighting functions are used but for the cascaded controller, weighting functions are redefined according to speed requirements of system for inner loop and position requirements of the speed for the outer loop. The order of H_∞ controllers is generally higher than the classical controllers so that one may think that, the cascade controller is unnecessary since its degree is much higher than the other H_∞ controllers and the speed feedback can lead to some problems during operation. The important point is that the aim of this thesis is not mainly to find the best controller but to find a new representation for naturally nonlinear systems. Furthermore, the uncertainties are defined on the whole plant instead of defining on each parameter which causes problems during the synthesis of the controllers in this thesis. The gamma values of the robust controllers are a bit higher than unity which may cause robustness problem on real applications but this situation can be guaranteed using a robust stability analysis. On the other hand, inner loop of the cascade controller; that is speed loop, could also be reduced to a second order system after its closed loop speed control is achieved so that the order of the position controller can be reduced significantly.

To sum up, the cascaded controller that handled in this thesis can be an alternative controller for the electromechanical actuator systems.

5.2 Future Works

In this study, jet vane parts are not physically constructed. Indeed, the jet vane part is taken as a disturbing torque on the system. As a first future work, the jet vane part

can be integrated to the real system and the controller performance can also be tested. In addition to this, as an alternative to the performance and ideal closed loop weightings, an additional performance weighting representing the error between reference input and measured output could also be assigned for robust controller synthesis. Thus, an unnecessary increase in controller order could be reduced and more optimized and easy to implement controllers could be designed. As an another future work, other ways of representing uncertainty in parametric level could also be improved for the future works. Eventually, load test can also be made in controlled speed and load conditions. To summarize, the future works to be done can be written as:

- integration of jet vanes to the physical system
- decision of alternative weighting functions between error and reference input
- reduction of controller orders
- optimization of controllers to decrease current consumption
- changing of uncertainty definition
- load test under controllable speed and torque

REFERENCES

[1] Fleeman, E. L., "Air-to-Air Missile Design and System Engineering Short Course," Ankara, 2013.

[2] Siouris, G. M., Missile Guidance and Control Systems, New York: Springer, 2004.

[3] Sutton, G. P., Biblarz, O., Rocket Propulsion Elements, John Wliey & Sons, Inc., 2001.

[4] "Air-Launched Weapons," IHS Jane's 360, [Online]. Available: http://www.janes.com/. [Accessed 20 May 2013].

[5] Control Actuation Workshop/System Engineering, Martin Marietta Training Notes, 1993.

[6] Chin, S. S., Missile Configuration Design, McGraw-Hill Book Company, Inc., 1961.

[7] Fleeman, E. L., Tactical Missile Design, Virginia: American Institute of Aeronautics and Astronautics, Inc., 2001.

[8] Mark, H., Encyclopedia of Space Science and Technology, vol. I, New Jersey: John Wiley & Sons, Inc., 2003.

[9] "Solid Rocket Thrust Vector Control," NASA, 1974.

[10] Yangel, M., Thrust Vector and Aerodynamic Control of Missiles, Msc Thesis: METU, Ankara, Turkey, 1995.

[11] Llyod, R., "A Review of Thrust Vector Control Systems for Tactical Missiles," in *AAIA/SAE Joint Propulsion Conferans*, Las Vegas, 1978.

[12] TVC Jet Vane Thermal Modelling Using Parametric System Identification, NPS69-88-001: Naval Post Graduate School, 1988.

[13] Schaefermeyer, M. R., Aerodynamic Thrust Vectoring for Attitude Control of a Vertically Thrusting Jet Engines, Utah, 2011.

[14] Balu, R., Marathe, A. G., Paul, P. J., Mukundas, H. S., "Analysis of Performance of a Hot Gas Injection Thrust Vector Control System," *J. Propulsion,* vol. 7, no. 4, pp. 580-585, 1991.

[15] "A4/V2 Makeup," Brothers Design, 1999. [Online]. Available: http://www.v2rocket.com. [Accessed 10 June 2014].

[16] Design and Analysis of Solid Rocket Motor Nozzle, AGARD-LS-150, 1988.

[17] Yu, M. S., Cho, H. H., Hwang, K. Y., Bae, J. C., "A Study on a Surface Ablation of the Jet Vane System in a Rocket Nozzle, AIAA-2004-2276," in *AIAA Thermophysics Conference*, Portland, Oregon, 2004.

[18] El-Sharkawy, A. I., "Experimental Studies on Thrust Vector in Solid Propellant Rockets," in *AIAA/SAE Propulsion Conference*, Orlando / Florida, 1977.

[19] Sung, H., Hwang, Y., "Thrust-Vector Characteristics of Jet Vanes Arranged in X-Formation Within a Shroud," *Journal of Propulsion and Power,* vol. 20, no. 3, pp. 501-508, 2004.

[20] Facciano, A. B., Seybold, K. G., Westberry-Kutz, T. L., Widmer, D. O., "Evolved SeaSparrow Missile Jet Vane Control System Prototype Hardware Development," *Journal of Spacecraft and Rockets,* vol. 39, no. 4, pp. 522-531, 2002.

[21] Kalnins, I., Gorlov, V., Gerhard, I., "The COSMOS Launch Services and Launch System Modernization Program, AIAA-2001-4699," in *AIAA Space Conferance and Exposition*, Albuquerque, 2001.

[22] Rainville, P., deChamplain, A., Kretschmer, D., Farinaccio, R., Stowe, R., "Unsteady CFD Calculation for Validation of a Multi-Vane Thrust Vector Control System," in *AIAA/ASME/SAE/ASEE Joint Propulsion Conference and Exhibit*, Florida, 2004.

[23] T. W. Bastian, "Jet Tab Control Mechanism for Thrust Vector Control". USA Patent 4,274,610, 23 June 1981.

[24] Edwards, S.S., Parker, G.H., "An Investigation of the Jetevator as a Means of Thrust Vector Control," Lockheed Missiles & Space Company Inc., California, 1958.

[25] Dumoulin, J., "Reaction Control System," 31 August 2000. [Online]. Available: http://science.ksc.nasa.gov. [Accessed 2014 10 16].

[26] Innocenti, M., Thukral, A., "Simultaneous Reaction Jet and Aerodynamic Control of Missile Systems," in *Aerospace Design Conference*, Irvine, CA, 1993.

[27] Machell A., Foulsham, P. G., "Reaction Control System". England Patent 4,955,558, 11 September 1990.

[28] Ellison, J. R., "Jet Tab Steerable Missile". USA Patent 3,986,683, 19 October 1976.

[29] Jacobson, M. D., "Droppable Jet Vane TVC". USA Patent 5,082,202, 21 January 1992.

[30] Kim, W. H., Bae, J. C., Lim, S. T., Park, S. H. "Jet Vane Thrust Vector Control System". USA Patent US 7,313,910 B2, 1 January 2008.

[31] Hatalsky, W., Facciano, A., Haight, S. D., Jordan, A., "Jet Vane Control System and Method". USA Patent 5,806,791, 15 September 1998.

[32] Doyle J., Francis B., Tannenbaum A., Feedback Control Theory, California,

Macmillan Publishing Co., 1990.

[33] Xue, D., Chen, Y., Atherton, D. P., Linear Feedback Control - Analysis and Desing with Matlab, Philadelphia: SIAM, 2007.

[34] Zames, G., "Feedback and Optimal Sensitivity: Model Reference Transformations, Multiplicative Seminorms, and Approximate Inverses," *IEEE Transactions on Automatic Control,* vol. 26, no. 2, pp. 301-320, 1981.

[35] Doyle J., Glover K., Khargonekar P.P., Francis B.A., "State Space Solutions to Standard H2 and H∞ Control Problems," *IEEE Trans. on Automatic Control,* vol. 34, no. 8, pp. 831-847, 1989.

[36] Rollins, L., "Robust Control Theory," [Online]. Available: http://users.ece.cmu.edu/. [Accessed 6 July 2014].

[37] Toscano, R., Structured Controllers for Uncertain Systems - A Stochastic Optimizaion Approach, London: Springer-Verlag, 2013.

[38] Bibel, J. E., Malyevac, D. S., "Guidelines for the Selection of Weighting Functions for H-Infinity Control NSWCDD/MP-92/43," Naval Surface Warfare Center, Dahlgren, Virginia, 1992.

[39] Skogestad, S., Postlethwaite, I., "Multivariable Feedback Control - Analysis and Design," John Wiley & Sons, 1996.

[40] Gu, D., Petkov, P. H., Konstantinov, M. M., Robust Control Design with Matlab, London: Springer, 2013.

[41] Zhou, K., Doyle, J. C., Glover, K., Robust and Optimal Control, New Jersey: Prentice Hall, 1996.

[42] Hartley, G. A., "H_∞ Controller Design for an SISO Electromechanical Actuator," in *AIAA Guidance, Navigation and Control Conference*, HiltonHilton Head Island, SC, U.S.A., 1992.

[43] Hartley, G. A., "Comparison of Classical and H-infinity Controller Design for a Single-axis Prototype Electromechanical Actuator," in *AIAA Guidance, Navigation and Control Conference*, Monterey, CA, U.S.A., 1993.

[44] Malasse, O., Zasadzinski, M., Iung, C., Hayar, H., Darouach, M., "H∞ Design Using Normalized Coprime Factors: An Application to an Electromechanical Actuator," in *IEEE Conference on Control Applications*, Glasgow, UK, 1994.

[45] Adam, E. J., Guesrtrin, E. D., "Identification and Robust Control of an Experimental Servo Motor," *ISA Transactions,* vol. 41, no. 2, pp. 225-234, 2002.

[46] Luo G., Fan, P., "Mixed H2/H∞ Control of Direct-Drive Electromechanical Actuator," in *International Conference on Electrical Machines and Systems*, Beijing, China, 2003.

[47] Ölçer, T. U., H2/H∞ Mixed Robust Controller Synthesis for a Fin Actuation System, Msc Thesis: METU, Ankara, Turkey, 2013.

[48] Daş, E., Güdümlü Bir Mühimmat Kanatçık Tahrik Sistemi İçin İki Döngülü Kontrol Sistemi Tasarımı, Msc Thesis: İTÜ, İstanbul, Turkey, 2014.

[49] Yoo, C. H., Lee, Y. C., Lee, S. Y., "A Robust Controller for an Electro-Mechanical Fin Actuator," in *Asian Control Conferance*, Grand Hyatt-Melbourne, Australia, 2004.

[50] Eker, İ., "Sliding Mode Control with PID Sliding Surface and Experimental Application to an Electromechanical Plant," *ISA Transactions,* vol. 45, no. 1, pp. 109-118, 2006.

[51] Schinstock, D. E., Haskew, T. A., "Identifcation of Continuous-Time, Linear, and Nonlinear Models of an Electromechanical Actuator," *Journal of Propulsion and Power,* vol. 13, no. 5, pp. 683-690, 1997.

[52] Schinstock, D. E., Scott, D. A., Haskew, T. A., "Modeling and Estimation for

Electromechanical Thrust Vector Control of Rocket Engines," *Journal of Propulsion and Power,* vol. 14, no. 4, pp. 440-446, 1998.

[53] Schinstock, D. E., Scott, D. A., Haskew, T. A., "Transient Force Reduction in Electromechanical Actuators for Thrust Vector Control," *Journal of Propulsion and Power,* vol. 17, no. 1, pp. 65-72, 2001.

[54] Ristanović, M., Lazić, D., Indin, I., "Experimental Validation of Improved Performances of an Electromechanical Aerofin Control System with a PWM Controlled DC Motor," *FME Transactions,* vol. 34, no. 1, pp. 15-20, 2006.

[55] Ristanović, M., Lazić, D., Indin, I., "Nonlinear PID Controller Modification of Electromechanical Actuator System for Aerofin Control with PWM Controlled DC Motor," *Automatic Control and Robotics,* vol. 7, no. 1, pp. 131-139, 2008.

[56] Lazić, D., Cojbasic, Z., Ristanović, M., "Fuzzy-Neuro-Genetic Aerofin Control," *Automatic Control and Robotics,* vol. 10, no. 1, pp. 71-82, 2011.

[57] Ristanović, M., Lazić, D., Indin, I., "Intelligent Control of DC motor Driven Electromechanical Fin Actuator," *Control Engineering Practice,* vol. 20, no. 6, pp. 610-617, 2012.

[58] Jeong, D. S., Choi, K. J., Woo, H. W., Kim, J. G., "Controller Design of Missile Actuator Using DSP," in *International Conference on Control, Automation and Systems*, Seoul, Korea, 2007.

[59] Khan, M. A., Todić, I., Miloš, M., Stefanović, Z., Blagojević, Dj., "Control of Electro-Mechanical Actuator for Aerospace Applications," *Strojarstvo,* vol. 52, no. 3, pp. 303-313, 2010.

[60] Gao, Y., Gu, L., Pan, L., "Application of Variable Structure Control in Missile Electromechanical Actuator System," in *International Conference on Intelligent Computation Technology and Automation*, Changsha, Hunan, China, 2008.

[61] Yan L., Dongyang, S., "Research on Electro-Mechanical Actuator System

Based on Discrete-time Variable Structure Control," in *WRI Global Congress on Intelligent Systems*, Wuhan, Hubei, China, 2010.

[62] Liu, X., Wu, Y., Deng, Y., Xiao, S., "A Global Sliding Mode Controller for Missile Electromechanical Actuator Servo System," *Journal of Aerospace Engineering,* vol. 228, no. 9, pp. 1-10, 2013.

[63] Dwivedula, R. V., Pagilla, P. R., "Effect of Compliance and Backlash on the Output Speed of a Mechanical Transmission System," *Journal of Dynamic Systems, Measurement, and Control,* vol. 134, no. 3, 2012.

[64] Nordin, M., Gutman, P. O., "Controlling Mechanical Systems with Backlash - A Survey," *Automatica,* no. 38, pp. 1633-1649, 2002.

[65] Axsys Technologies, *Brushless DC Motors Handbook,* Axsys Technologies.

[66] ADVANCED Motion Controls, "Downloadable Resources," 1997. [Online]. Available: http://www.a-m-c.com. [Accessed 20 August 2014].

[67] Landau, I. D., Zito, G., Digital Control Systems - Design, Identification and Implementation, Germany: Springer-Verlag London Limited, 2006.

[68] Söderström, T., Stoica, P., System Identification, Cambridge: Prentice Hall Internatioal (UK) Ltd., 1989.

[69] "Selecting a Sampling Rate," National Instruments, June 2010. [Online]. Available: ni.com. [Accessed 12 June 2014].

[70] National Instruments, "Stimulus and Acquisition Considerations in the System Identification Process," 17 June 2010. [Online]. Available: http://www.ni.com. [Accessed 2014 August 26].

[71] Ljung, L., "System Identification Toolbox™ R2014b," Mathworks, 2014.

[72] Babuska, R., Fuzzy Modelling for Control, Boston: Kluwer academic Publishers, 1988.

[73] Rogers, R., "Building a Benchtop PID Controller," 2013. [Online]. Available: http://www.keithley.com/. [Accessed 29 July 2014].

[74] O'Dwyer, A., Handbook of PI and PID Controller Tuning Rules, London: Imperial College Press, 2006.

[75] Özkan B., Dynamic Modeling, Guidance and Control of Missiles, Ph.D. Thesis: METU, Ankara, Turkey, 2005.

[76] Fortuna L., Frasca M., Optimal and Robust Control Advanced Topics with MATLAB, Florida, CRC Press, 2012.

[77] Beaven, R. W., Wright, M. T., Seaward, D. R., "Weighting Function Selection in the H-infinity Design Process," *Control Engineering Practice,* vol. 4, no. 5, pp. 625-633, 1996.

[78] Hu, J., Bohn, C., Wu, H. R., "Systematic H∞ Weighting Function Selection and Its Application to the Real-time Control of a Vertical Take-of Aircraft," *Control Engineering Practice,* vol. 8, pp. 241-252, 200.

[79] Grimble, M. J., Biss, D., "Selection of Optimal Control Weighting Functions to Achieve Good H-infinity Designs," in *International Conference on Control*, Oxford, 1988.

APPENDICES

A.1. Air-to-Air Missiles

Table 7. *Air-to-Air missiles [4]*

System	Country	Project Type	Length [m]	Dia. [mm]	Wing Span [m]	Weight [kg]	Warhead Weight [kg]	Warhead	Fuze	Guidance	Range [km]	CAS	TVC	Speed [Mach]	Service
AIM-54A PHOENIX	USA	LRAA	3.96	380	0.92	443	60	HE Continuous Rod	IR	Semi Active, Update, Inertial & Active Radar	135	Canard	n/k	5	1974
AIM-54C PHOENIX	USA	LRAA	3.96	380	0.92	463	60	HE Continuous Rod	Active Radar	Semi Active, Update, Inertial & Active Radar	150	Tail	n/k	5	1985
AIM-120 AMRAAM	USA	MRAA	3.65	178	0.63	157	22	HE Fragmentation	Active Radar	Command, Inertial & Active Radar	50	Tail	No	n/k	1991
FIM-92 STINGER	USA	SRAA	1.57	69	0.09	10.1	3	HE Blast/ Fragmentation	Impact	Passive IR/UV	4.5	Canard	n/k	2.2	1988
AIM-9B SIDEWINDER	USA	SRAA	2.83	127	0.53	76	4.5	HE Blast/ Fragmentation	IR	IR	2	Canard	No	n/k	1956
AIM-9D SIDEWINDER	USA	SRAA	2.87	127	0.64	90	9	HE Continuous Rod	RF	IR	3	Canard	No	n/k	1965
AIM-9L SIDEWINDER	USA	SRAA	2.87	127	0.64	87	9.5	HE Fragmentation	Active Laser	IR	8	Canard	No	n/k	1976
AIM-9P SIDEWINDER	USA	SRAA	3.07	127	0.64	82	12	HE Blast/ Fragmentation	RF/Active Laser	IR	8	Canard	No	n/k	1982
AIM-9M SIDEWINDER	USA	SRAA	2.90	127	0.64	86	10.15	HE Fragmentation	Active Laser	IR	8	Canard	No	n/k	1978
AIM-9S SIDEWINDER	USA	SRAA	2.87	127	0.64	86	10.15	HE Fragmentation	Active Laser	IR	8	Canard	No	n/k	1993
AIM-9X SIDEWINDER	USA	SRAA	2.90	127	0.44	85	9.1	HE Fragmentation	Active Laser	IIR	10	Tail	Jet Vane	n/k	2002
AIM-7F SPARROW	USA	MRAA	3.66	203	1.02	227	39	HE Continuous Rod	RF	Semi-Active Radar	40	Wing	No	n/k	1975
AIM-7M SPARROW	USA	MRAA	3.66	203	1.02	231	40	HE Blast/ Fragmentation	Active Radar	Semi-Active Radar	45	Wing	No	n/k	1982
AIM-7P SPARROW	USA	MRAA	3.66	203	1.02	231	40	HE Blast/ Fragmentation	Active Radar	Command, Semi-Active Radar	45	Wing	No	n/k	1992
AIM-7R SPARROW	USA	MRAA	3.66	203	1.02	231	40	HE Blast/ Fragmentation	Active Radar	Command, Semi-Active Radar, IR	45	Wing	No	n/k	1992
AIM-4F	USA	SRAA	2.18	167	0.61	68	18	HE	RF	Semi-Active Radar	8	Tail	No	n/k	1960
AIM-4G	USA	SRAA	2.02	167	0.61	66	12	HE	RF	IR	3	Tail	No	n/k	1960
AIM-4D	USA	SRAA	2.02	167	0.51	61	12	HE	Active Radar	IR	3	Tail	No	n/k	1963

System	Country	Project Type	Length [m]	Dia. [mm]	Wing Span [m]	Weight [kg]	Warhead Weight [kg]	Warhead	Fuze	Guidance	Range [km]	CAS	TVC	Speed [Mach]	Service
AIM-26B (Rb27)	USA	SRAA	2.13	165	0.63	115	18	HE	Active Radar	Semi-Active Radar	10	Tail	No	n/k	1963
PL-11 (LY-60)	China	MRAA	3.69	200	1	220	33	HE Fragmentation	n/k	Semi Active Radar	15	Tail	n/k	n/k	2001
PL-10	China	MRAA	3.99	286	1.17	300	n/k	HE Fragmentation	RF	Semi Active CW Radar	15	Tail	n/k	n/k	1996
PL-9C	China	SRAA	2.99	160	0.856	121	10	HE	Active Laser	Multi Element IR	22	Canard	n/k	3.5	1990
PL-9	China	SRAA	2.90	157	0.816	115	10	HE	Active Laser	Single Element IR	15	Canard	n/k	3.5	1991
PL-8	China	SRAA	2.99	160	0.81	115	10	HE Fragmentation	Active Laser	IR	15	Canard	No	n/k	1990
PL-7	China	SRAA	2.75	157	0.66	93	12	HE Fragmentation	IR	IR	5	Canard	No	n/k	1987
PL-5B	China	SRAA	2.896	127	0.67	87	9	HE	IR	IR	5	Canard	No	2.5	1982
PL-5E	China	SRAA	2.89	127	0.617	83	9	HE	Active Laser	IR	3	Canard	No	2.5	1995
PL-3	China	SRAA	2.99	127	0.53	82	13.5	HE Blast/ Fragmentation	IR	IR	3	Canard	No	n/k	1980
PL-2B	China	SRAA	2.99	127	0.53	82	11.3	HE Blast/ Fragmentation	IR	IR	3	Canard	No	n/k	1970
PL-1	China	SRAA	2.5	200	0.654	83	15	HE	RF	Radar Beam-Rider	5	n/k	n/k	n/k	1964
QW-2 VANGUARD	China	SRAA	1.59	72	n/k	10.7	1.42	HE	Active Laser	IR	6	n/k	n/k	n/k	2000
QW-1 VANGUARD	China	SRAA	1.53	72	0.14	11.32	1.5	HE	Impact	IR	5	n/k	n/k	n/k	1992
AIM-132 ASRAAM	UK	SRAA	2.9	166	0.45	88	n/k	HE Blast/ Fragmentation	Active Laser	IRR	20	Tail	Jet Vane	n/k	2001
SKY FLASH	UK	MRAA	3.66	203	1.02	195	30	HE Continuous Rod	Active Radar	Semi-Active Radar	40	Wing	No	n/k	1978
STARTREAK	UK	SRAA	1.4	130	0.25	16	3	Steerable Darts with HE	Impact	Radio Command with Laser Grid	6	n/k	n/k	n/k	2003
MICA	France	MRAA	3.1	165	0.56	112	12	HE Blast/ Fragmentation	Active Radar	Command, Semi-Active Radar or IRR	60	Tail	Jet Vane	n/k	1997

System	Country	Project Type	Length [m]	Dia. [mm]	Wing Span [m]	Weight [kg]	Warhead Weight [kg]	Warhead	Fuze	Guidance	Range [km]	CAS	TVC	Speed [Mach]	Service
MISTRAL 1/2 (ATAM)	France	SRAA	1.86	90	0.18	19.5	3	HE Tungsten Ball	Laser and Impact	IR	6	n/k	n/k	n/k	1996
R550 MAGIC 1	France	SRAA	2.72	157	0.66	89	13	HE Fragmentation	IR	IR	3	Canard	No	n/k	1975
R550 MAGIC 1	France	SRAA	2.72	157	0.66	89	12	HE Fragmentation	RF	IR	20	Canard	No	n/k	1992
R530	France	SRAA	3.28	263	1.10	195	27	HE Fragmentation	RF	Semi Active Radar or IR	15	Tail	No	n/k	1963
SUPER 530F	France	MRAA	3.54	263	0.88	245	30	HE Fragmentation	RF	Semi Active Radar	25	Tail	No	n/k	1980
SUPER 530D	France	MRAA	3.80	263	0.62	270	30	HE Fragmentation	Active Radar	Semi Active Radar	40	Tail	n/k	n/k	1987
IRIS-T	Germany	SRAA	3.00	127	0.35	87	11.4	HE Fragmentation	Active Laser	IIR	12	Tail	Jet Vane	n/k	2003
ASPIDE Mk1	Italy	MRAA	3.70	203	1.00	220	30	HE Fragmentation	Active Radar	Semi-Active Radar	35	n/k	n/k	n/k	1988
ASPIDE 2000	Italy	MRAA	3.70	234	0.64	225	30	HE Fragmentation	Active Radar	Semi-Active Radar	40	n/k	n/k	n/k	2002
MAA-1A PIRANHA 1	Brazil	SRAA	2.67	152	0.65	86	12	HE Fragmentation	Active Laser	Passive IR	6	Canard	No	n/k	1990
MAA-1B PIRANHA 2	Brazil	SRAA	2.75	152	0.66	89	12	HE Fragmentation	Active Laser	Dual Band IR	10	Canard	No	n/k	2012
AMM-3	Japan	SRAA	3.00	127	0.64	91	15	HE Fragmentation	Active Laser	IR	8	Canard	No	n/k	1991
AMM-4	Japan	SRAA	3.70	220	n/k	n/k	n/k	HE Fragmentation	Active Radar	Inertial, Semi-Active Radar	80	Tail	n/k	n/k	1999
AMM-5 (XAAM-D)	Japan	SRAA	n/k	n/k	n/k	n/k	n/k	HE	Active Radar	IIR	20	Tail	Jet Vane	n/k	2006
TIEN CHIEN II	Taiwan	MRAA	3.60	190	0.62	183	22	HE Blast/ Fragmentation	Active Radar	Active Radar and inertial Midcourse Guidance	60	Tail	n/k	n/k	1999
TIEN CHIEN I	Taiwan	SRAA	2.87	127	0.54	90	n/k	HE Blast/ Fragmentation	Active Laser Proximity and Impact	IR	8	n/k	n/k	n/k	1993
ASTRA	India	MRAA	3.57	178	n/k	154	15	HE Blast/ Fragmentation	RF Proximity	Inertial in mid-course, with data link updates, active radar terminal homing	80	Tail	n/k	4+	n/k
PYTHON 5	Israel	MRAA	3.09	160	0.64	103.6	11	HE Fragmentation	n/k	IIR	20	Canard	No	4	2006
PYTHON 4	Israel	SRAA	3.00	160	0.35	103.6	11	HE Fragmentation	Active Laser	IR	15	Canard	No	3.5	1992

System	Country	Project Type	Length [m]	Dia. [mm]	Wing Span [m]	Weight [kg]	Warhead Weight [kg]	Warhead	Fuze	Guidance	Range [km]	CAS	TVC	Speed [Mach]	Service
PYTHON 3	Israel	SRAA	3.00	160	0.86	120	11	HE Fragmentation	Active Radar	IR	15	Canard	n/k	n/k	1982
SHAFRIR 2	Israel	SRAA	2.60	160	0.64	95	11	HE Fragmentation	n/k	IR	3	n/k	n/k	n/k	1978
DERBY	Israel	MRAA	3.62	160	0.64	118	n/k	n/k	Proximity	Inertial mid-course, with data link updates, active radar terminal phase	63+	n/k	n/k	4	n/k
Project 5	Israel	MRAA	3.50	160	n/k	n/k	n/k	HE Fragmentation	RF	IIR / Active Radar	n/k	Tail	No	n/k	1999
V3E A-DARTER	South Africa	MRAA	2.98	166	0.48	89	n/k	HE Fragmentation	Active Laser	Inertial and IIR	20	Tail	Jet Vane	n/k	n/k
V3C DARTER	South Africa	SRAA	2.75	160	0.66	90	17	HE Fragmentation	Active Laser	IR	5	Canard	n/k	n/k	1994
U DARTER	South Africa	MRAA	2.75	160	0.66	96	17	HE Fragmentation	Laser Proximity and	IR	8	n/k	N7k	n/k	1990
R DARTER	South Africa	MRAA	3.62	160	n/k	120	n/k	n/a	Proximity		63	n/k	n/k	n/k	2000
A DARTER	South Africa	MRAA	2.98	166	n/k	93	n/k	HE	n/k	Inertial mid-course, data link updates, active radar	n/k	n/k	n/k	n/k	2006
S DARTER	South Africa	MRAA	n/k	n/k	n/k	n/k	n/k	n/k	n/k	Inertial and Active Radar	n/k	n/k	n/k	n/k	2007
KUKRI V3A/B	South Africa	SRAA	2.94	127	0.53	74	n/k	HE Fragmentation	n/k	IR	4	n/k	n/k	n/k	1981
METEOR BVRAAM	International	LRAA	3.65	178	n/k	185	n/k	Pre-formed HE Blast/ Fragmentation	Proximity and	Data-linked mid-course, active radar terminal seeker	100+	Tail	n/k	4+	n/k
SA-14 'GREMLIN'	Russia	SRAA	1.47	72	0.30	10.5	2	HE Fragmentation	Impact	IR	5	n/k	n/k	n/k	1974
SA-7B 'GRAIL'	Russia	SRAA	1.44	72	0.30	10	1.8	HE Fragmentation	Impact	IR	5	n/k	n/k	n/k	1971
R-37 (AA-X-13)	Russia	LRAA	4.2	380	0.70	600	60	HE Fragmentation	n/k	Inertial with command updates, semi-active radar and active radar	150	n/k	n/k	n/k	2003
R-77 (AA-12 'ADDER')	Russia	MRAA	3.6	200	0.4	175	22	HE Fragmentation	Active Laser	Inertial, Command and Active Radar	75	n/k	n/k	n/k	2003
R-77M-PD	Russia	MRAA	3.7	200	n/k	225	n/k	HE	n/k	Inertial and Active Radar	n/k	n/k	n/k	n/k	2005
R-73 M1 (AA-11 'ARCHER')	Russia	MRAA	2.9	170	0.51	105	7.4	HE Fragmentation Rod	Active Radar	Inertial and IR	20	n/k	Jet Tab	n/k	1987
R-73 M2 (AA-11 'ARCHER')	Russia	MRAA	2.9	170	0.51	110	7.4	HE Fragmentation Rod	Active Radar	Inertial and IR	30	n/k	Jet Tab	n/k	1996

System	Country	Project Type	Length [m]	Dia. [mm]	Wing Span [m]	Weight [kg]	Warhead Weight [kg]	Warhead	Fuze	Guidance	Range [km]	CAS	TVC	Speed [Mach]	Service
R-27T (AA-10 'ALAMO')	Russia	LRAA	3.80	230	0.97	245	39	Expanding Rod	Active Radar	IR	65	Wing	n/k	n/k	1985
R-27R (AA-10 'ALAMO')	Russia	LRAA	4.08	230	0.97	253	33	Expanding Rod	Active Radar	Active Radar, Inertial, Command and SAR	60	Wing	n/k	n/k	1985
R-27ET (AA-10 'ALAMO')	Russia	LRAA	4.50	260	0.97	343	39	Expanding Rod	Active Radar	IR	80	Canard	n/k	n/k	1985
R-27ER (AA-10 'ALAMO')	Russia	LRAA	4.70	260	0.70	350	39	Expanding Rod	Active Radar	Active Radar, Inertial, Command and SAR	62.5	Canard	n/k	n/k	1995
R-27AE (AA-10 'ALAMO')	Russia	LRAA	4.78	260	0.80	350	39	Expanding Rod	Active Radar	Active Radar, Inertial, Command and SAR	110	Canard	n/k	n/k	1995
R-33 (AA-9 'AMOS')	Russia	LRAA	4-15	380	1.18	490	47	HE Blast/ Fragmentation	Active Radar	Inertial with command updates and semi-active radar	120	Tail	n/k	n/k	1989
R-60M (AA-8 'APHID')	Russia	SRAA	2.08	130	0.43	63	3	HE Fragmentation	Active Radar	IR	3	n/k	n/k	n/k	n/k
R-24T ('APEX' IR)	Russia	SRAA	2.09	120	0.43	43	3.5	HE Rod	Active Laser	IR	10	n/k	n/k	n/k	1982
R-24T ('APEX' IR)	Russia	MRAA	4.60	200	1.04	250	35	HE Fragmentation	Active Radar	Command and IR	50	n/k	n/k	n/k	n/k
R-24R ('APEX' IR)	Russia	MRAA	4.80	200	1.04	270	35	HE Fragmentation	Active Radar	Command and IR	50	n/k	n/k	n/k	n/k
R-40T/R-46TD (ACRIS IR)	Russia	MRAA	6.20	355	1.8	467	35	HE Fragmentation	Radar and Active Laser	Command, Inertial and Semi-active Radar	35/60	n/k	n/k	n/k	n/k
FATTER	Iran	SRAA	77.8	n/k	n/k	n/k	n/k	n/k	n/k	n/k	n/k	n/k	n/k	n/k	n/k

A.2. System Identification Input-Outputs in Time Domain

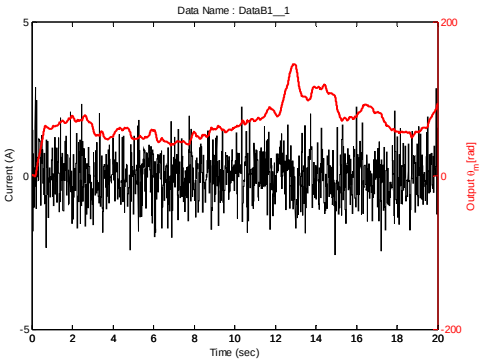

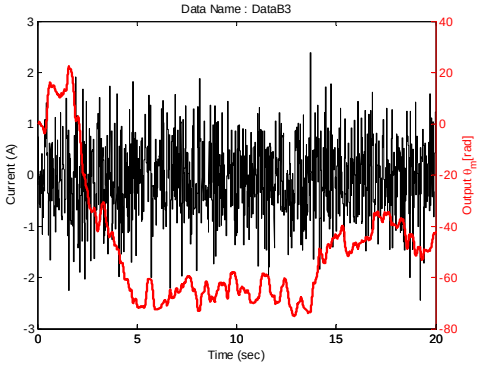

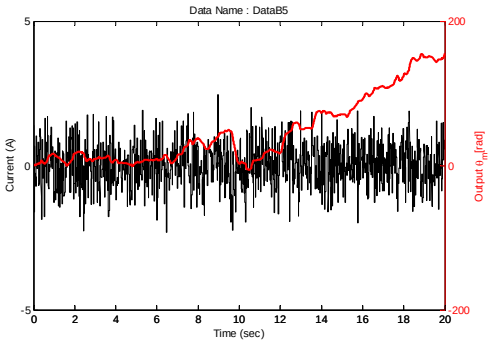

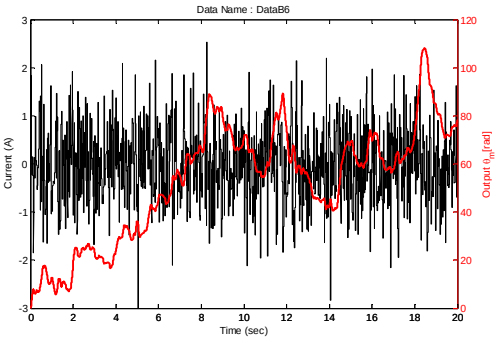

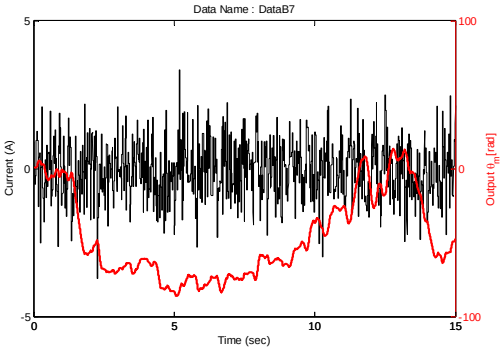

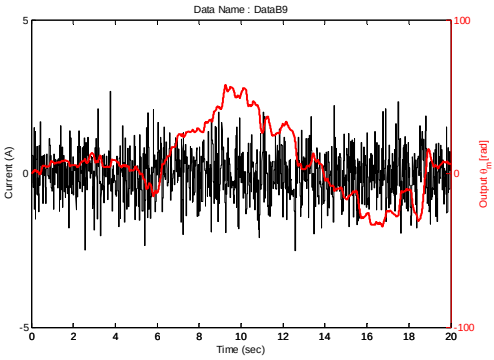

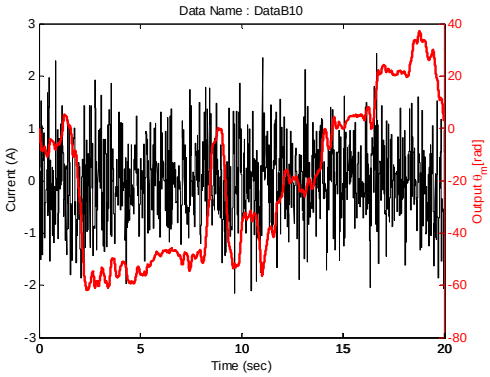

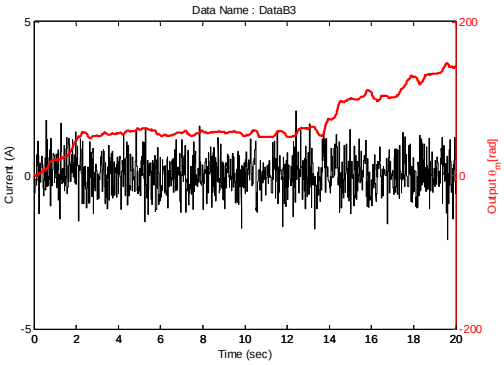

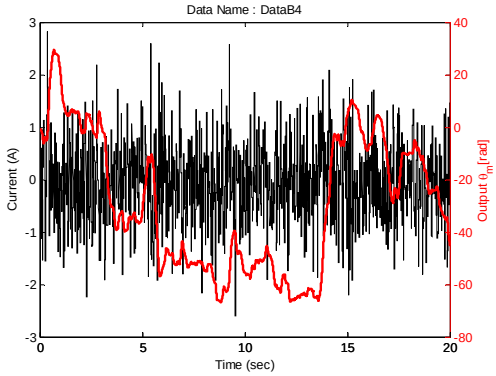
Data Name : DataB4
Current (A)
Output θm [rad]
Time (sec)

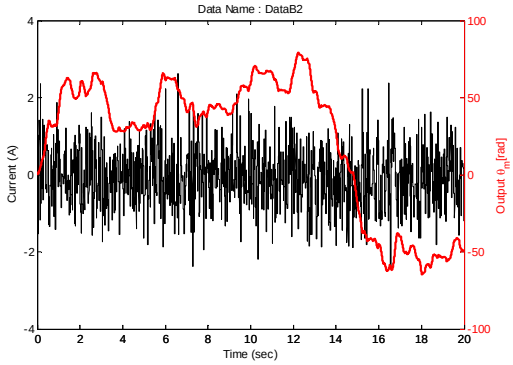
Data Name : DataB2
Current (A)
Output θm [rad]
Time (sec)

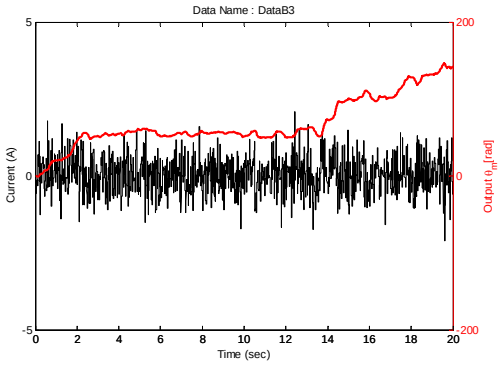
Data Name : DataB3
Current (A)
Output θm [rad]
Time (sec)

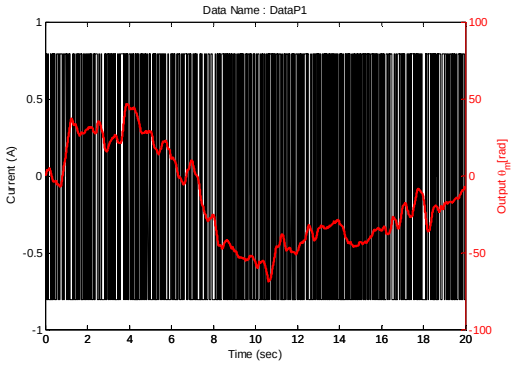
Data Name : DataP1
Current (A)
Output θm [rad]
Time (sec)

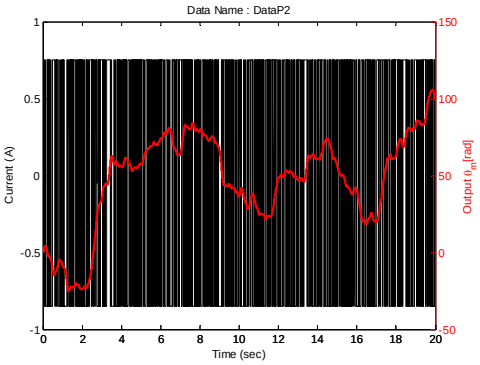
Data Name : DataP2
Current (A)
Output θm [rad]
Time (sec)

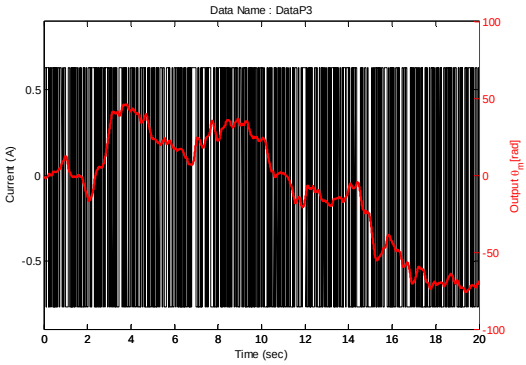
Data Name : DataP3
Current (A)
Output θm [rad]
Time (sec)

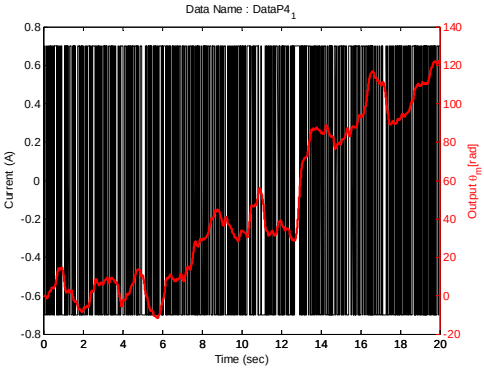
Data Name : DataP4 1
Current (A)
Output θm [rad]
Time (sec)

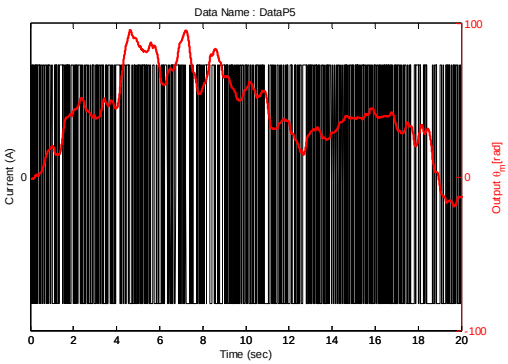
Data Name : DataP5
Current (A)
Output θm [rad]
Time (sec)

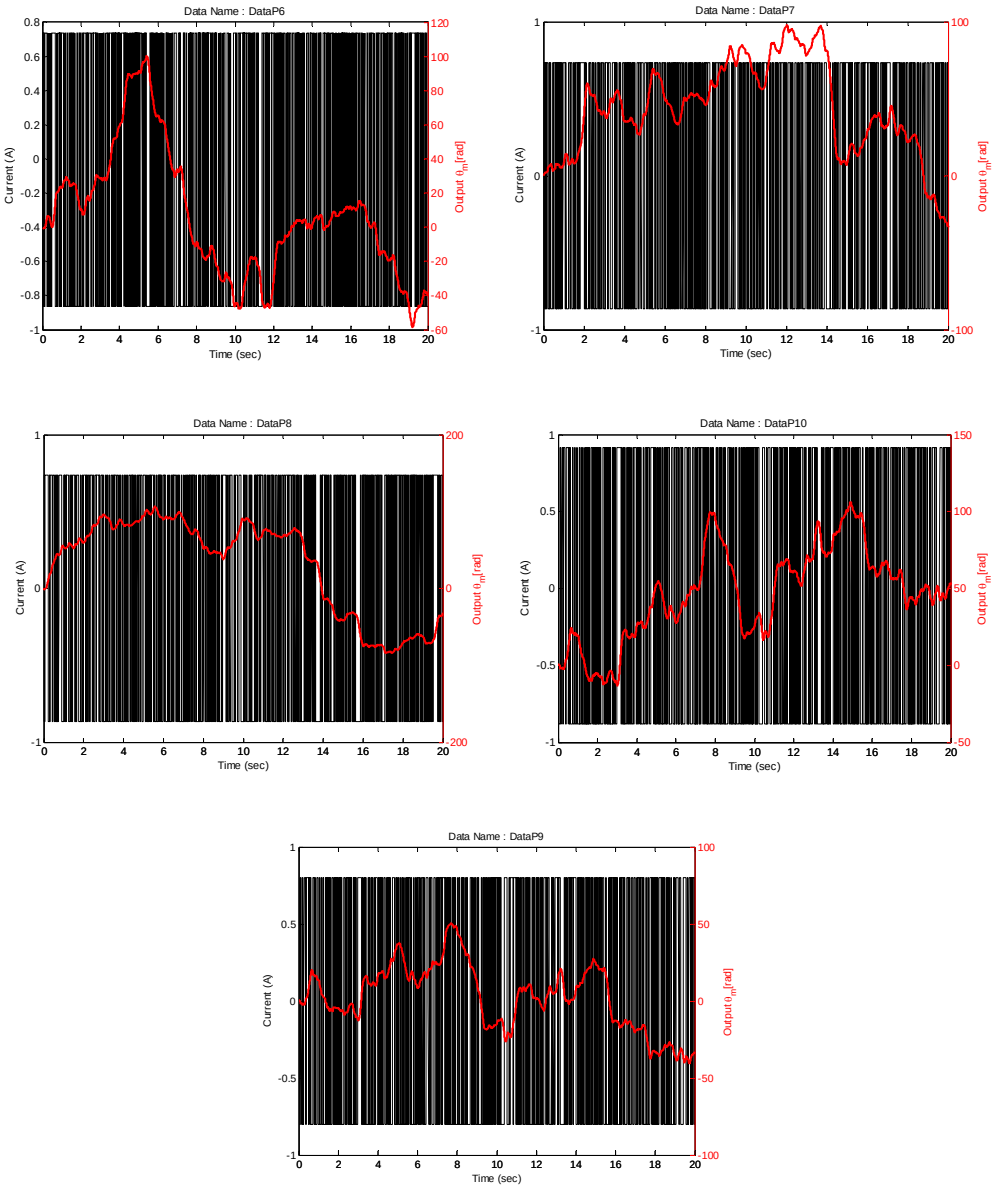

Figure 109. *Input and output signal set used in identification*

A.3. Frequency Spectrum of Input Signals

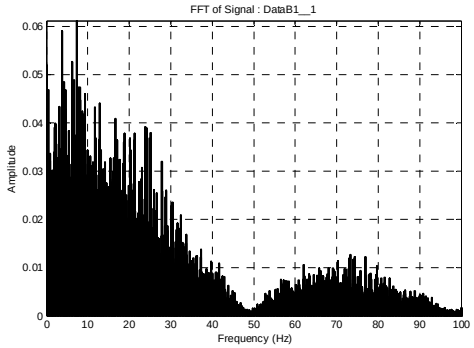

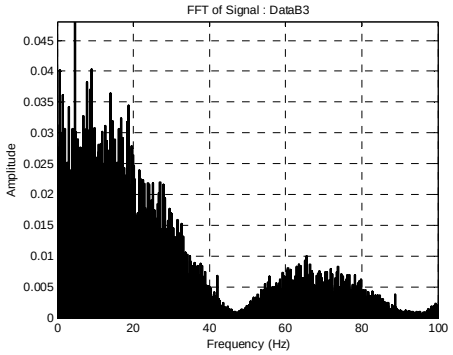

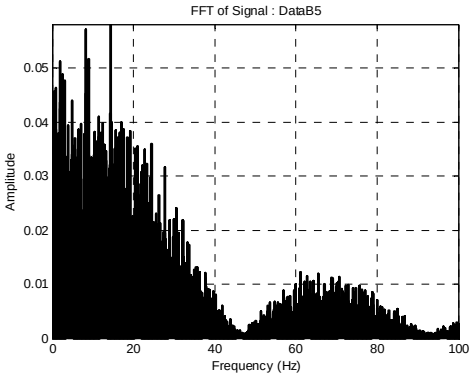

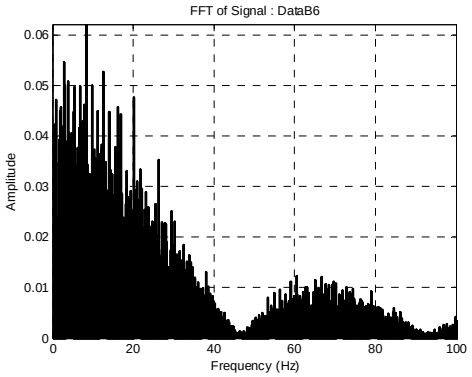

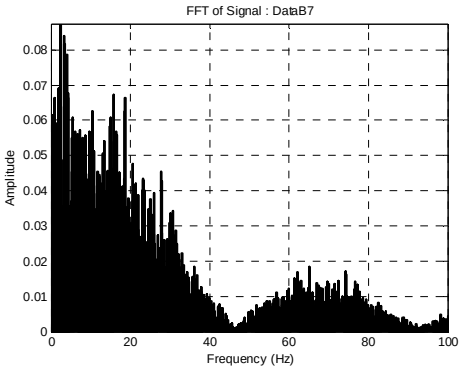

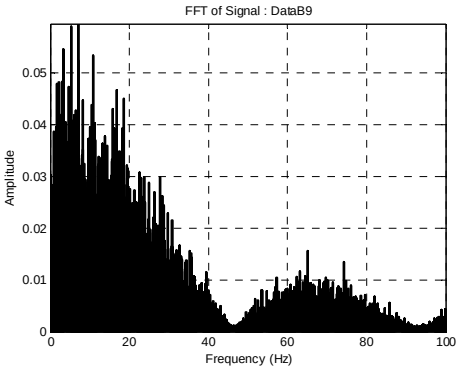

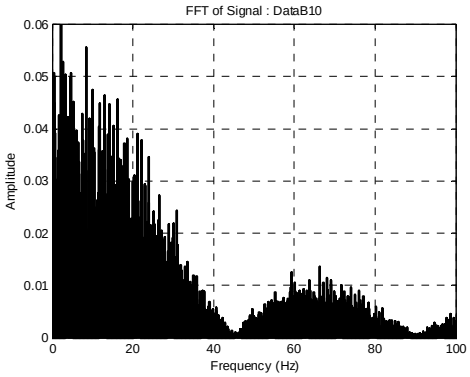

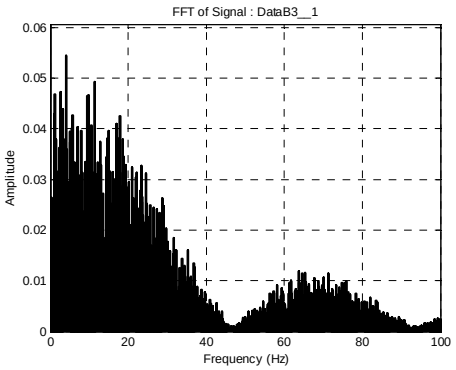

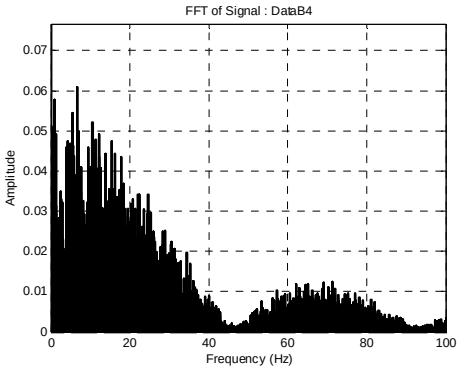
FFT of Signal : DataB4
Amplitude
Frequency (Hz)

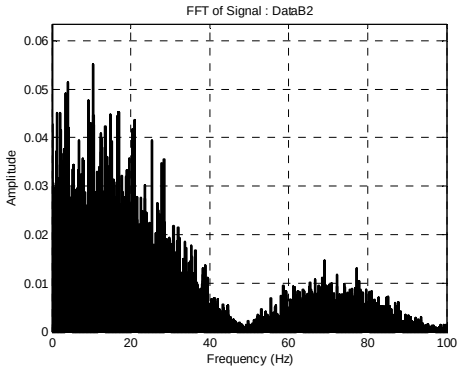
FFT of Signal : DataB2
Amplitude
Frequency (Hz)

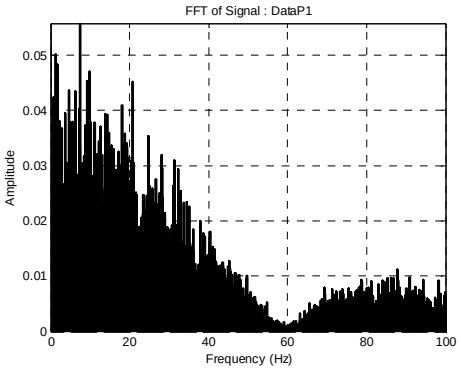
FFT of Signal : DataP1
Amplitude
Frequency (Hz)

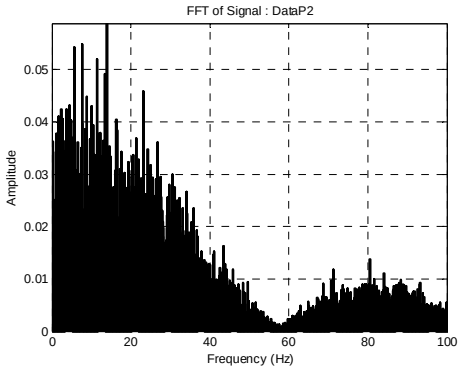
FFT of Signal : DataP2
Amplitude
Frequency (Hz)

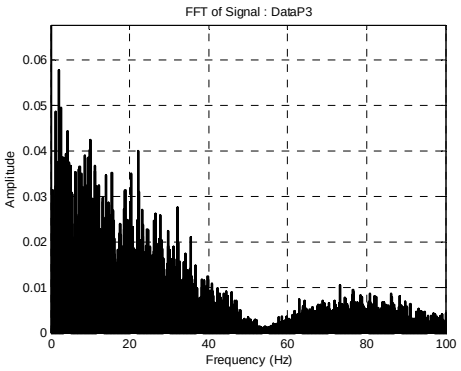
FFT of Signal : DataP3
Amplitude
Frequency (Hz)

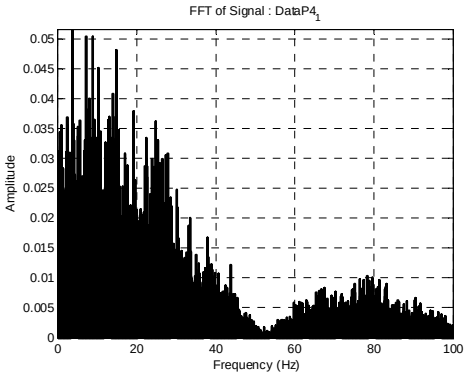
FFT of Signal : DataP4_1
Amplitude
Frequency (Hz)

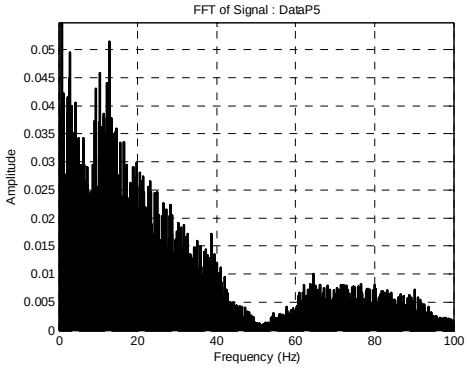
FFT of Signal : DataP5
Amplitude
Frequency (Hz)

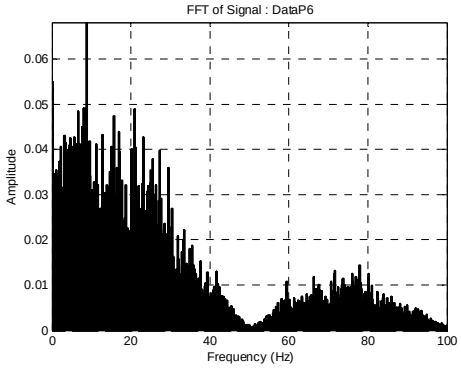
FFT of Signal : DataP6
Amplitude
Frequency (Hz)

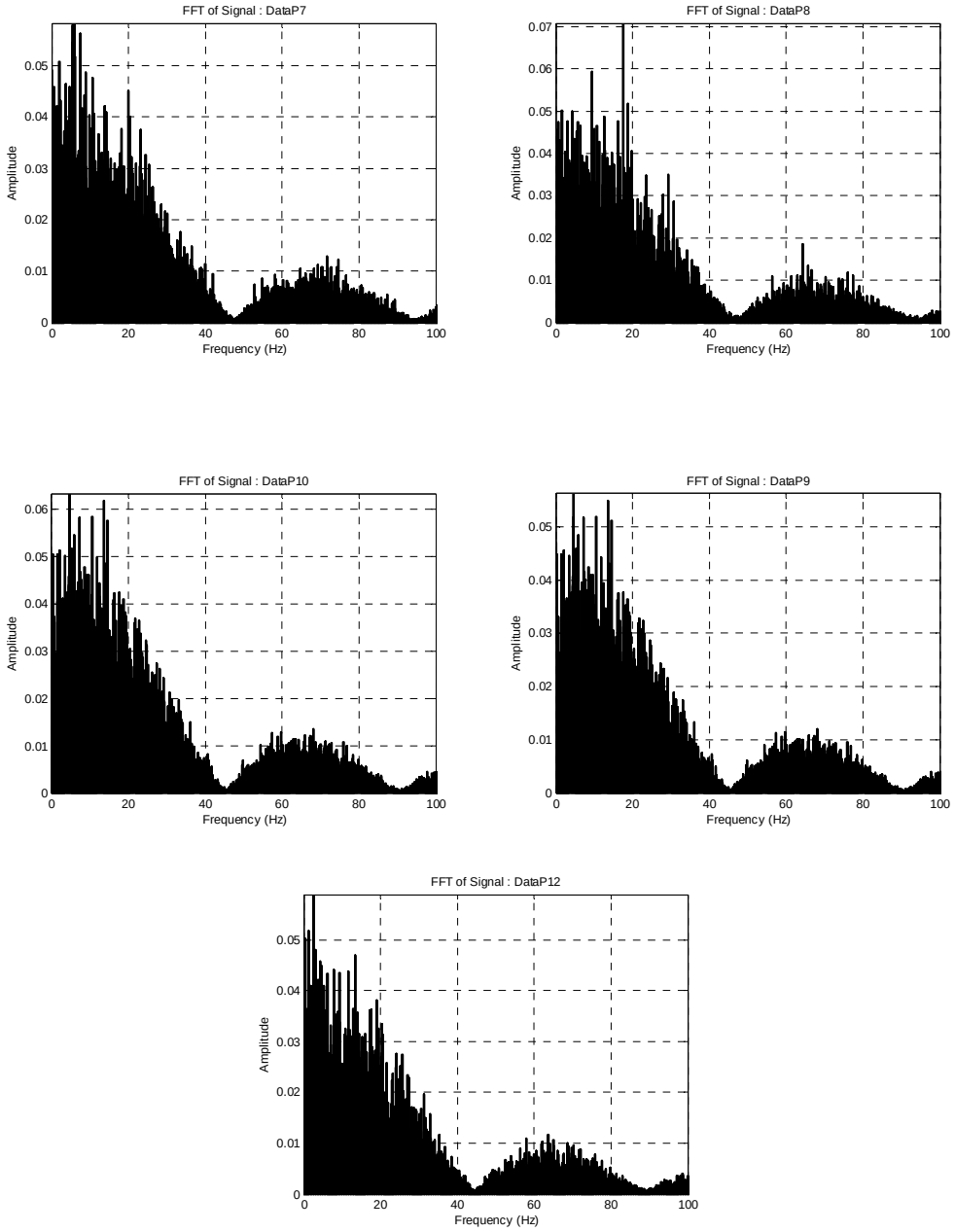

Figure 110. *Frequency content of input signals*

A.4. Generalized Plant Matrices

Plant_Hinf =

A =

	x1	x2	x3	x4	x5	x6	x7	x8	x9
x1	-3.142	0	0	0	0	0	0	0	0
x2	421.1	-177.7	-123.4	0	0	0	0	0	0
x3	0	128	0	0	0	0	0	0	0
x4	0	0	96.4	-0.7854	0	0	0	0	-6.251
x5	0	0	0	0	-69.81	0	0	0	0
x6	0	0	0	0	0	-3.142	0	0	0
x7	0	0	0	0	0	-261.8	-10	0	0
x8	0	0	0	0	0	0	65.63	-6.339	0
x9	0	0	0	0	0	0	32.81	0	0

B =

	uWm	w(1)	w(2)	w(3)	u
x1	0	0.25	0	0	0
x2	0	0	0	0	0
x3	0	0	0	0	0
x4	0	0	0	0	0
x5	0	0	0	0	0.6606
x6	0	0	8	0	0
x7	0	0	0	0	64
x8	0	0	0	0	0
x9	1	0	0	0	0

C =

	x1	x2	x3	x4	x5	x6	x7	x8	x9
uwm	0	0	0	0	0	0	12.15	-1.024	0
z1	0	0	0	0	-0.5872	0	0	0	0
z2	0	0	4.418	7.163	0	0	0	0	-0.2865
y	52.64	0	0	0	0	0	0	0	-1

D =

	uwm	w(1)	w(2)	w(3)	u
ywm	0	0	0	0	0
z1	0	0	0	0	0.05556
z2	0	0	0	0	0
y	0	0	0	-0.06283	0

Plant_2_DOF_Hinf =

A =

	x1	x2	x3	x4	x5	x6	x7	x8	x9
x1	-0.3142	0	0	0	0	0	0	0	0
x2	336.9	-710.9	-493.5	0	0	0	0	0	0
x3	0	512	0	0	0	0	0	0	0
x4	0	0	944.5	-4.712	0	0	0	0	-30.62
x5	0	0	0	0	-69.81	0	0	0	0
x6	0	0	0	0	0	-3.142	0	0	0
x7	0	0	0	0	0	-261.8	-10	0	0
x8	0	0	0	0	0	0	65.63	-6.339	0
x9	0	0	0	0	0	0	32.81	0	0

B =

	uWm	w(1)	w(2)	w(3)	u
x1	0	0.0625	0	0	0
x2	0	0	0	0	0
x3	0	0	0	0	0
x4	0	0	0	0	0
x5	0	0	0	0	0.6606
x6	0	0	8	0	0
x7	0	0	0	0	64
x8	0	0	0	0	0
x9	1	0	0	0	0

C =

	x1	x2	x3	x4	x5	x6	x7	x8	x9
yWm	0	0	0	0	0	0	12.15	-1.024	0
z1	0	0	0	0	-1.174	0	0	0	0
z2	0	0	17.67	17.55	0	0	0	0	-0.573
y1	21.06	0	0	0	0	0	0	0	0
y2	0	0	0	0	0	0	0	0	1

D =

	uWm	w(1)	w(2)	w(3)	u
yWm	0	0	0	0	0
z1	0	0	0	0	0.1111
z2	0	0	0	0	0
y1	0	0	0	0	0
y2	0	0	0	0.02513	0

Plant_speed_Hinf =

A =

	x1	x2	x3	x4	x5	x6	x7	x8	x9
x1	-0.3142	0	0	0	0	0	0	0	0
x2	336.9	-710.9	-493.5	0	0	0	0	0	0
x3	0	512	0	0	0	0	0	0	0
x4	0	0	944.5	-4.712	0	0	0	0	-30.62
x5	0	0	0	0	-69.81	0	0	0	0
x6	0	0	0	0	0	-3.142	0	0	0
x7	0	0	0	0	0	-261.8	-10	0	0
x8	0	0	0	0	0	0	65.63	-6.339	0
x9	0	0	0	0	0	0	32.81	0	0

B =

	uWm	w(1)	w(2)	w(3)	u
x1	0	0.0625	0	0	0
x2	0	0	0	0	0
x3	0	0	0	0	0
x4	0	0	0	0	0
x5	0	0	0	0	0.6606
x6	0	0	8	0	0
x7	0	0	0	0	64
x8	0	0	0	0	0
x9	1	0	0	0	0

C =

	x1	x2	x3	x4	x5	x6	x7	x8
yWm	0	0	0	0	0	0	12.15	-1.024
z1	0	0	0	0	-1.174	0	0	0
z2	0	0	17.67	17.55	0	0	0	0
y1	21.06	0	0	0	0	0	0	0

y2	0	0	0	0	0	0	0	0

	x9
ywm	0
z1	0
z2	-0.573
y1	0
y2	1

D =

	uwm	w(1)	w(2)	w(3)	u
ywm	0	0	0	0	0
z1	0	0	0	0	0.1111
z2	0	0	0	0	0
y1	0	0	0	0	0
y2	0	0	0	0.02513	0

```
Plant_cascade=
```

A =

	x1	x2	x3	x4	x5	x6
x1	-177.7	-123.4	2.269e-08	0.0002097	-0.0246	-1.443
x2	128	-6.423e-19	4.58e-20	-6.827e-11	1.952e-09	7.156e-09
x3	1.688e-18	96.4	-0.7854	2.646e-11	-7.563e-10	0.02556
x4	1.51e-14	2.04e-15	-6.321e-17	-2.486e+04	-7393	2165
x5	-1.772e-12	-2.393e-13	7.417e-15	8192	0.00082	0.003007
x6	-1.04e-10	-1.404e-11	4.352e-13	-0.001683	-4096	0.2154
x7	1.525e-09	2.059e-10	-6.383e-12	0.02468	-0.7056	1021
x8	-1.118e-08	-1.51e-09	4.68e-11	-0.181	5.174	18.97
x9	2.049e-08	2.768e-09	-8.578e-11	0.3317	-9.483	-34.78
x10	-1.881e-08	-2.54e-09	7.873e-11	-0.3045	8.704	31.92
x11	4.314e-09	5.827e-10	-1.806e-11	0.06983	-1.996	-7.321
x12	-4.938e-10	-6.67e-11	2.067e-12	-0.007994	0.2285	0.8381
x13	-9.203e-13	-1.243e-13	3.853e-15	-1.49e-05	0.0004259	0.001562

	x7	x8	x9	x10	x11	x12
x1	21.17	-155.2	284.5	-261.1	59.9	-6.857
x2	-2.62e-08	1.168e-08	-4.864e-09	-2.69e-10	1.292e-10	-9.662e-12
x3	0.05821	0.1345	0.2823	0.3092	0.3564	0.1948
x4	1054	411.5	206.3	57.31	13.91	7.098
x5	-0.01102	0.004988	-0.002192	2.306e-05	2.306e-05	-4.865e-07
x6	-0.6014	0.3163	-0.1157	0.005021	0.002274	0.000446
x7	9.546	-4.329	1.726	-0.2186	-0.2565	-0.129
x8	442.6	31.5	-13.98	-0.07094	-0.1214	-0.1491
x9	127.4	70.41	25.37	-0.3621	-0.4132	-0.0747
x10	-117	52.95	40.75	0.1468	0.09181	-0.08913
x11	26.83	-12.15	5.336	15.95	-0.08721	-0.01619

x12	-3.071	1.39	-0.6108	0.006428	7.997	-0.01038
x13	-0.005724	0.002591	-0.001138	1.198e-05	1.198e-05	-0.1301

	x13
x1	-0.01278
x2	-1.902e-10
x3	-6.222
x4	40.88
x5	-7.991e-05
x6	-0.002759
x7	4.24
x8	4.25
x9	3.679
x10	2.04
x11	0.9877
x12	0.4352
x13	-0.004115

B =

	w(1)	w(2)	u
x1	1.794e-11	0	-2.287e-15
x2	-3.477e-11	0	4.431e-15
x3	1.347e-11	0	-1.717e-15
x4	1.245e-07	0	64
x5	-1.461e-05	0	1.862e-09
x6	-0.0008569	0	1.092e-07
x7	0.01257	0	-1.602e-06
x8	-0.09216	0	1.175e-05
x9	0.1689	0	-2.153e-05
x10	-0.155	0	1.976e-05
x11	0.03556	0	-4.532e-06

```
x12   -0.004071          0   5.188e-07
x13  -7.586e-06          0   9.669e-10
```

C =

	x1	x2	x3	x4	x5	x6
z1	0	0	0	0	0	0
z2	-1.302e-20	4.418	7.163	-9.035e-17	1.06e-14	0.001171
y	3.778e-09	-7.32e-09	2.836e-09	2.621e-05	-0.003075	-0.1763

	x7	x8	x9	x10	x11	x12
z1	10	0	0	0	0	0
z2	20.002668	0.006164	0.01294	0.01417	0.01634	0.008927
y	2.656	-19.38	35.61	-32.59	7.544	-0.8259

	x13
z1	0
z2	-0.2851
y	-0.9969

D =

	w(1)	w(2)	u
z1	0	0	0.001194
z2	0	0	0
y	0	-0.02513	0

A.5. Weightings Functions of Cascade H_∞ Controller

H_∞ Speed Controller

$$W_{ref} = \frac{0.4363}{0.2122s + 1}$$

$$W_{hinge} = \frac{30}{0.3183s + 1}$$

$$W_u = \frac{0.055556s + 17.4557}{s + 349.1}$$

$$W_{ideal} = \frac{\omega_n^2}{s^2 + 2\xi\omega_n s + \omega_n^2},\ \omega_n = 100\ Hz,\ \xi = \sqrt{2}/2$$

$$W_{perf} = \frac{0.057296s + 18.0024}{s + 15.71}$$

$$W_{noise} = 2 \cdot 2 \cdot pi / 500$$

H_∞ Position Controller

$$W_{ref} = \frac{0.01745}{0.3138s + 1}$$

$$W_{hinge} = \frac{30}{0.3183s + 1}$$

$$W_u = \frac{1}{200 * 240 * pi / 180}$$

$$W_{ideal} = \frac{\omega_n^2}{s^2 + 2\xi\omega_n s + \omega_n^2},\ \omega_n = 20\ Hz,\ \xi = \sqrt{2}/2$$

$$W_{perf} = \frac{0.28648s + 90.0120}{s + 15.71}$$

$$W_{noise} = 2 \cdot 2 \cdot pi / 500$$